UNIVERSITY OF CALIFORNIA
RIVERSIDE

Synthesis, Characterization, and Device Applications of Viral-Templated Copper Sulfide and Copper Oxide Semiconductor Nanomaterials

A Dissertation submitted in partial satisfaction
of the requirements for the degree of

Doctor of Philosophy

in

Electrical Engineering

by

Mohammed Shahriar Zaman

December 2014

Dissertation Committee:
Dr. Elaine D. Haberer, Chairperson
Dr. Jianlin Liu
Dr. Ming Liu

The Dissertation of Mohammed Shahriar Zaman is approved:

_____

_____

_____

Committee Chairperson

University of California, Riverside

Acknowledgments

I would like to express my gratitude towards my advisor Prof. Elaine D. Haberer. Without her help and inspiration my research work could not have progressed. She helped me understand the basics of bio-templates and guided me towards building knowledge about M13 phage templates and how these could be utilized for mineralizing materials. I learned a lot about analyzing data and presenting them to a general audience to keep their interest on the topic from her. Her encouragement inspired me to tackle hard to solve problems at times. I gained a lot of experience by setting up equipment, writing various protocols for the lab which helped me stay organized.

I would like to thank my lab mate Chung Hee Moon for her contribution. She encouraged me through tough times. She had developed the pVIII library successfully in the lab which I used for biopanning. She also helped me analyze the mass spectroscopy data of the virus. She took the ammonia gas sensing measurement data and helped me further analyze them. We would often share our problems and she would suggest possible solutions which came in really useful.

Next I would like to acknowledge my lab mates Xiaoyin Ma, Joon Bok Lee, Steven Garcia, Hector Lopez Hernandez, and Gabriel Bernard Grajeda for their contributions in publishing my papers. I would also like to thank all my lab mates for their support and encouragement.

I would like to thank Dr. Krassimir Bozhilov for helping me to take high resolution transmission electron microscope images of the mineralized copper sulfide materials.

I would like to thank Prof. Nosang Myung and his students for kindly letting me use their lab for taking IV measurments and using their gas sensing systems.

I would like to thank Dr. Ilkeun Lee for taking and analyzing the x-ray photoelectron spectroscopy spectrums of the fresh and aged copper sulfide samples.

I would also like to thank Dong Yan and Dexter Humphrey at the Center for Nanoscale Science and Engineering for teaching me how to work on cleanroom equipment and helping me out whenever I ran into a problem.

Last but not least I would like to thank my parents who encouraged me all the way through my PhD life. I had really hard times but they supported and inspired me at all moments. I would like to specially thank my dear wife for being so supportive and patient. She had to endure all my frustrations and still she managed to put a smile on my face and encouraged me. My family and friends motivated me to get this done and I am really thankful to them.

Dedicated to my parents, wife, family,

friends, and well-wishers, without your support

I would not have been able to complete this.

ABSTRACT OF THE DISSERTATION

Synthesis, Characterization, and Device Applications of Viral-Templated Copper Sulfide and Copper Oxide Semiconductor Nanomaterials

by

Mohammed Shahriar Zaman

Doctor of Philosophy, Graduate Program in Electrical Engineering
University of California, Riverside, December 2014
Dr. Elaine D. Haberer, Chairperson

Nature has the ability to mineralize and build intricate nanostructures of inorganic materials with a very high precision. Various bio-molecules can mineralize and control the morphology and composition of inorganic materials at ambient conditions. Inspired by nature, this work focuses on utilizing the M13 virus, a filamentous phage, 880 nm in length and 6 nm in diameter, for mineralizing copper sulfide and copper oxide semiconductor nanomaterials. The various coat proteins of the virus can easily be modified to express different peptides with specific affinity to various inorganic materials. A phage-display technique was utilized to identify a copper sulfide binding peptide expressed on the entire pVIII coat protein of the virus. This modified phage was used for synthesizing copper sulfide nanoparticles along the length of the template. To increase the yield and coverage of the mineralized material on the phage-templates, non-specific electrostatic interactions between a negatively charged phage (E3) and positively charged copper ions were utilized to synthesize copper sulfide at ambient conditions. The

mineralized material coated the phage template and was identified to be cubic $Cu_{1.8}S$, a non-stoichiometric phase of the copper sulfide material system. The material showed strong optical absorption below 800 nm due to band-to-band transitions and localized surface plasmon resonance (LSPR) peaks in the infrared region. The LSPR peaks increased in absorption and the electrical resistance of the materials decreased with time indicating an increase in the number of free carriers in the material due to exposure at ambient conditions. The free carrier increase was attributed to a compositional change on the surface of the material. The synthesized $Cu_{1.8}S$ was utilized to fabricate NH_3 gas sensors. These gas sensors showed a high response to NH_3 gas which may be attributed to the large surface-to-volume ratio of the viral-templated nanomaterials. Finally, utilizing the non-specific electrostatic interactions between the E3 phage and positively charged cations, copper oxide nanoparticles were also synthesized along the viral-template. These semiconductor materials were identified to be a mixture of CuO and Cu_2O with a direct optical band gap of 2.87 eV. These viral-templated semiconductor nanomaterials have potential applications for incorporation into future devices.

Table of Contents

List of Figures

List of Tables

1. Introduction

In recent years the growth of nanostructures and applications of these nanomaterials has fueled researchers to develop novel synthesis methods. Nanostructured materials offer unique electrical and optical properties which makes them promising objects to study. Often the existing traditional methods of producing materials are not capable of achieving intricate and complex structures required for various applications. The bottom up assembly process on the other hand involves the construction of atoms or molecules one unit at a time by chemical synthesis through self-assembly. Self-assembly enables the fabrication of intricate nano-structures. Bio-templated assembly is an alternative to conventional synthesis method that has drawn much attention from researchers. In this dissertation we show that using a bio-template we were able to biomineralize copper sulfide and copper oxide p-type semiconductor nanoparticles and utilized the bio-templated material to fabricate a device thus showing its device applicability.

1.1 Biomineralization

Biomineralization is a process where biological molecules synthesize various materials with intricate structures. Nature has been producing complicated nanostructures for millions of years. These structures are produced under mild conditions. A common example of biomineralization is biosilicification. The diatom is one of the most important sources for the application of biological approaches and molecules to the mineralization

of inorganic materials. The cell walls of diatoms consist of hydrated, amorphous silica [1, 2]. These diatoms possess the ability to produce silica under relatively mild conditions [3, 4]. The silica created by these diatoms offer intricate and organized control over the formation of these structures. Sponges also biomineralize amorphous silica termed as spicules [5, 6]. The spicule morphology though appears rather simple when compared to the intricate structures synthesized by diatoms but these structures can grow up to 3 m in length [7]. Another interesting example of biomineralization is the deposition of magnetic materials in bacteria, algae, termites, bees, mollusks, fish, and pigeons [8, 9]. The most common are magnetotactic bacteria which produces magnetic particles (Fe_3O_4) [9]. The exact mechanism of the synthesis process is still under investigation but an extensive analysis by Arakaki et al. showed that the synthesizing peptide contains hydroxyl containing amino acids which are known to bind to metals and hydrophilic amino acids which could capture metal ions [10].

Biomineralization can also occur as a result of detoxification of various organisms. Metals such as gold, silver, and cadmium are toxic to certain organisms. As a pathway of detoxification there are many bacteria, fungi, algae and plants that can synthesize metal nanoparticles [11, 12]. Sweeny et al. synthesized CdS nanoparticles of 2-5 nm in size utilizing E. coli [13]. The lactic-acid producing bacterial and the active bacterial component of buttermilk can biomineralize gold, silver and alloys of gold and silver [14].

1.2 Peptide Biotemplates

The self-assembling technique of living organisms has inspired researchers to explore rational methods for the synthesis of a rich family of functional inorganic crystals or hybrid organic/inorganic materials with specific size, shape, orientation, complex form and hierarchy owing to their importance and potential applications in industry [15]. Natural systems have led to the study of many different biological molecules (for example, nucleic acids, carbohydrates, proteins and peptides) [16]. The distinctive sequence specific self-assembly [16] and recognition properties [16] of peptides make them useful as building blocks for directing the growth and assembly of inorganic nanostructures. Naik et al. utilized a synthetic peptide to synthesize arched and elongated silica structures [17]. Peptide based templates have been used to grow gold and silver nanoparticles, nanotubes and nanowires [18]. Brown et al. utilized 3 repeating polypetides which were identified through the screening of a cell-surface displayed peptide library, to modify and accelerate the morphology and growth of gold nanoparticles [19]. These polypetides were proposed to bind to gold nanoparticles and influence their growth. Djalali et al. used a gold binding peptide AHHAHHAAD to mineralize gold nanoparticles [20]. The binding peptides were first immobilized on a heptane nanowire and were subsequently used to nucleate gold nanoparticles. The gold nanocrystals were polydisperse in nature and ranged from 4 – 30 nm in diameter [20]. Bovine serum albumin (BSA), a common protein was investigated for the mineralization of gold nanoparticles. Burt et al. utilized BSA to yield well-dispersed gold nanoparticles less than 2 nm in size [21]. A technologically important material titanium dioxide could

also be mineralized using peptides. The protein coats isolated from spicules of sponge were utilized to synthesize titanium dioxide under a mild reaction condition from an aqueous titanium complex solution [22]. Apoferritin is another protein which is also a very good candidate for templating semiconductor nanoparticles. Wong and Mann used apoferritin to synthesize CdS nanoparticles. They demonstrated that the protein was capable of binding to Cd^{2+} and could synthesize CdS within the inner cavity of the protein. These nanoparticles were stable under aqueous conditions for extended periods of time [23]. Au nanoparticles less than 10 nm in size were mineralized on the tobacco mosaic virus (TMV) template at acidic pH conditions [24]. The same TMV virus was utilized to synthesize silver nanoparticles aligned within the inner 4 nm channel of the virus [24]. Banerjee et al. have utilized the HG12 peptide to produce copper nanostructures on the surface of bionanotubes [25]. The organized protein structure on the capsid of the Tobacco Mosaic Virus (TMV) was utilized to synthesize Pt nanoparticles [24]. The tubular structure of TMV capsid has also been utilized as a template for the synthesis of Co and Ni nanowires [26]. The M13 bacteriophage has been used as a template to produce different nanostructures such as quantum dots [27, 28] virus based films [29], micro and nanofibers [30], magnetic and semiconducting nanowires [31], nanorings [32], lithium nanowires for battery electrode application [33]. M13 has also been used to align inorganic, organic and biological nanosized materials [34]. Water soluble polyaniline (PANi) / M13 [35], M13 – PEDOT [36] composite nanowires were constructed using M13 as a template which have potential electronics, optics, sensing and biomedical engineering applications. The use of ambient conditions,

near neutral pH solutions, environment friendliness, reduced cost and precise control over the size, shape, chemistry and crystal structure of the inorganic products [18] can make biomolecule based approaches as an attractive alternative to traditional production techniques.

1.3 M13 virus

M13 is a *Escherichia coli* specific filamentous bacteriophage which was first discovered in Munich, Germany [37]. The phage belongs to a family of filamentous bacteriophages with single-stranded DNA genomes. The virus is approximately 880 nm in length and 6.5 nm in diameter consisting of 6400 bp [38-40]. The single – stranded DNA is covered by a proteinaceous coat. The coat contains five different proteins as shown in figure 1. Two minor coat proteins pIII and pVI cap one end and two other minor coat proteins pVII and pIX cap the other end. Each minor coat protein is present at about 5 copies per particle. The major coat protein consists of approximately 2700 copies of the pVIII protein, which covers the length of the particle [39, 41]. All of the five coat proteins are essential for structural stability.

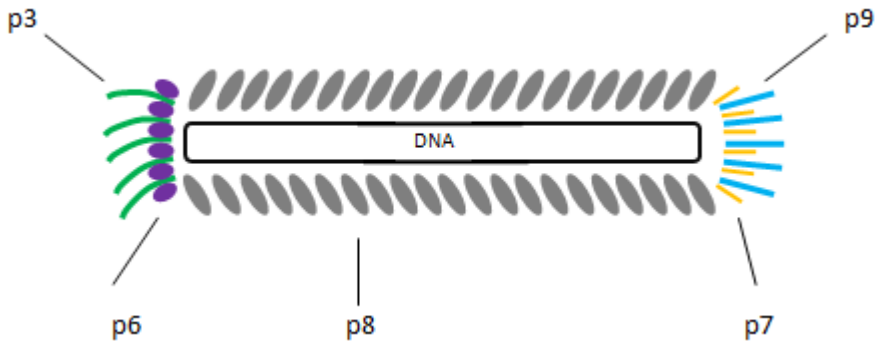

Figure 1. Various coat proteins of the M13 filamentous bacteriophage.

The pIII is the largest and the most complex of the coat proteins. It contains 406 amino acids and around 42 kDa in molecular weight [41]. The pVIII major coat protein has 112 amino acids and around 12 kDa in molecular weight [41]. The major coat proteins are arranged with a five-fold rotational axis in a α-helical strtucture [41]. The pVIII protein has an n-terminus or an amino-terminus on the surface and a c-terminus or carboxyl-terminus on the inside of the structure. The n-terminal end is negatively charged due to acidic amino acids which give the phage an overall negative charge. This is shown in figure 2.

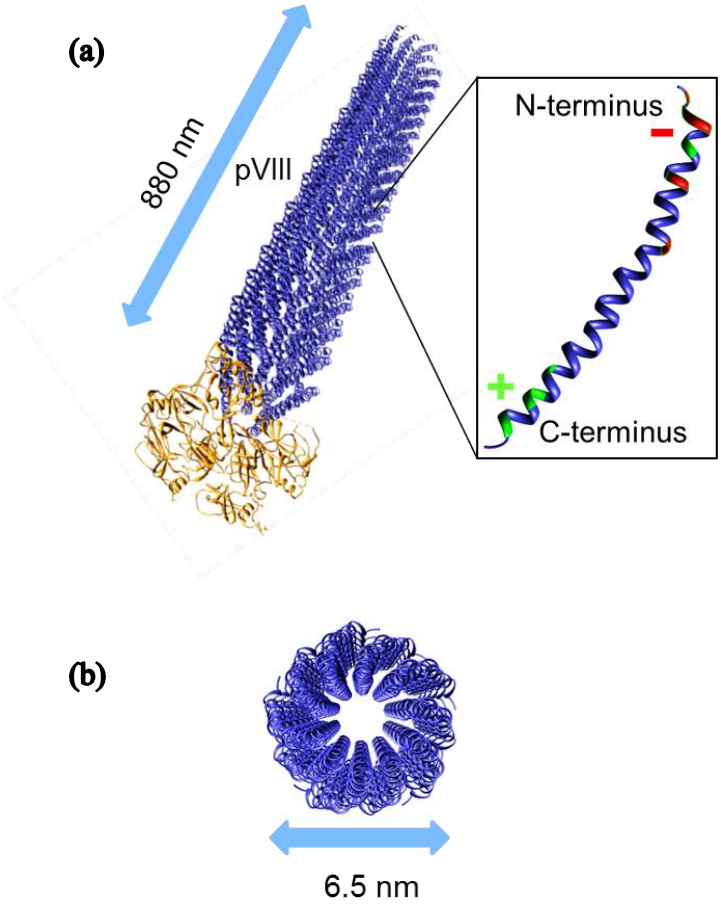

Figure 2. (a) pVIII coat protein structure on the M13 bacteriophage (b) cross-section of the pVIII coat protein.

Random peptides can be inserted at the n-terminus of the structure. Due to phage structural stability the length of peptides that can be genetically modified into the pVIII coat protein is restricted to five to six amino acids [39].

M13 replicates by infecting the *E. coli* bacteria. The replication process starts by the pIII end of the phage binding to the F pilus of the *E. coli* cell and inserting the DNA inside the bacterial cell. Inside the host cell the single stranded DNA is converted to a double–stranded form and is used as a template to further duplications. The various coat proteins are assembled inside the host cell. Eventually the single-stranded DNA is extruded through pores in the host cell and is surrounded by various coat proteins. The assembly is initiated by the incorporation of pVII and pIX at one end of the virus. Thousands of pVIII coat proteins are then assembled along the length of the phage particle. Finally the process is terminated by the addition of pIII and pVI at the other end of the bacteriophage. The assembled phage particle is then released into the environment. The whole M13 replication process is non-lytic. The newly assembled phages extrude continuously from the infected cells. The infected cell continues to grow and replicate though at a reduced rate.

1.4 Materials of interest

The materials that are going to be explored in this dissertation are copper sulfide and copper oxide. Both of these materials are p-type semiconductors, the charge carrier being holes. Both materials are non-toxic in nature and abundant. The materials can have various compositions and have various applications.

1.4.1 Copper sulfide

Copper sulfide (Cu_xS) is a semiconductor which exists in several polymorphic forms ranging in composition from Cu_2S to CuS. Among the most well-characterized phases are high chalcocite (Cu_2S, hexagonal), low chalcocite (Cu_2S, orthorhombic), djurleite ($Cu_{1.95}S$), digenite ($Cu_{1.8}S$), and covellite (CuS) [42]. The Cu-deficient phases of this p-type material exhibit sizable hole concentrations which increase with decreasing copper content and cause the band gap to increase due to the Moss–Burstein effect [43, 44]. Although the band gaps of many non-stoichiometric phases are not well-defined, a range of 1.2–2.58 eV (Cu_2S–CuS) is generally accepted for bulk materials [45-47]. The large hole concentrations in these materials also cause significant free carrier absorption within the infrared spectral region. The spectral range of the observed interband transitions and the tunability of the free carrier absorption of copper sulfide are highly desirable for photovoltaic and plasmonic applications, respectively. The optical and electrical properties are dependent on phase and composition, which have proven challenging to control.

1.4.2 Copper oxide

Copper oxide is an abundant, non-toxic p-type semiconductor which exists primarily in two compositions. The lower oxidation state, copper (I) oxide (Cu_2O), appears red in color and has a bulk band gap near 2.1 eV [48], whereas the higher oxidation state, copper (II) oxide (CuO), is black with a bulk band gap at approximately 1.85 eV [48]. Optically absorbing in the ultraviolet (UV) and visible spectral range, these materials are useful for a number applications including photovoltaic devices [49-51],

photodetectors [52], and photocatalysis [53]. Furthermore, copper oxides can be used for gas sensors [54, 55], enzyme-free glucose sensors [56], lithium ion batteries [57], and supercapacitors [58].

1.5 Research scope

In this dissertation we utilize the M13 filamentous bacteriophage to synthesize copper sulfide and copper oxide nanoparticles on the phage template. We developed the process of synthesizing copper sulfide nanoparticles on the phage template and used the phage templated materials as ammonia gas sensors. To show the versatility of the synthesis process we utilized the phage to synthesize copper oxide nanoparticles.

In chapter 2 we show that the phage display technique can be used to isolate peptides that bind to copper sulfide. The binding peptides were utilized to mineralize copper sulfide under ambient conditions. The synthesized material was analyzed using transmission electron microscope, electron diffraction pattern and energy dispersive x-ray spectroscopy. It was found that the material was Cu_2S but may have some oxidation. The synthesis process had a low yield and required a more robust and repeatable process.

In chapter 3, we develop a more robust process of copper sulfide synthesis utilizing the non-specific electrostatic interactions between the phage-template and the precursor ions. Although the coverage of material varied along the length of the virus, the process had a higher yield and was repeatable.

Next the optical and electrical characteristics of the material will be determined in chapter 4. Here, using UV/Vis/NIR spectrophotometry the optical absorption spectrum of the material was determined. The optical and electrical stability is an important aspect of

any material that will be discussed in this chapter. The material was found to be changing both optically and electrically with time.

In chapter 5, we utilize the phage-templated material as an ammonia gas sensor. We show that the material can be used to detect ammonia gas under ambient temperature and pressure. The gas sensors had better or comparable gas response compared to other copper sulfide based ammonia gas sensors.

Chapter 6 discusses the synthesis process of copper oxide using the same phage template that was used to mineralize copper sulfide. This shows the versatility of the synthesis process. In addition to the synthesis process the optical absorption of the material was determined from which the optical band gap was calculated. The optical band gap indicated the presence of quantum confinement in the nanoparticles.

In this dissertation we show that the virus template can be successfully utilized to synthesize copper sulfide and copper oxide nanoparticles on the viral template. The synthesized material can also be used for device applications. These studies would help in further utilizing viral-templated materials for incorporation in future device assimilations.

2 Copper Sulfide Mineralization with Material Specific Binding Peptides

2.1 Introduction

Nature has the ability to mineralize and control the shape, morphology and composition of various metals and semiconductors. Inspired by nature, researchers have been focusing on identifying peptides and proteins capable of nucleating various technologically important materials. A widely used method for screening peptides capable of either binding or mineralizing a particular material is called phage display technique or biopanning technique. The phage display technique is based on evolutionary principle where the peptide which has the strongest affinity for the target material will dominate eventually. The process is shown in figure 3.

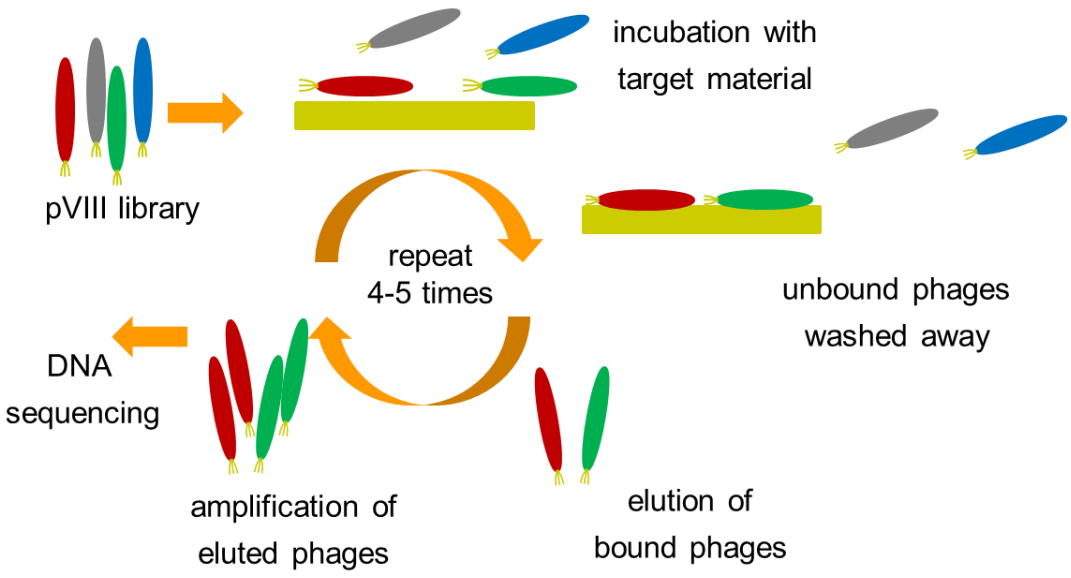

Figure 3. Phage display technique

The process starts with a library of phage which has random peptides fused into either the pIII or pVIII coat protein of the virus. A fixed amount of the phage library is incubated with the target material in a buffer solution. The buffer solution helps the phage stay dispersed and prevents agglomeration of powder materials. The incubation allows for some of the phages to bind to the target material. The exact binding mechanism of the peptides on the phage and the target material is complex and often not clear. After the incubation period the unbound phages are washed away. The bound phages on the target material are then eluted either by chemical or by physical elution. In chemical elution the pH of the solution is lowered such that the binding between the phages and the target material is disrupted and bound phages are released. On the other hand, in physical elution, the phages are sonicated at high frequency to release them from the target material. Either elution method can be adopted but physical elution can yield stronger binders [59]. Donatan et al. utilized the physical elution technique to identify and screen 9 strong mica binders that chemical elution was unable to detect [59]. An amplification of the bound phages follows afterwards and the whole screening process is repeated 4-5 times to increase the stringency of the binding phages. The DNA of the bound phages are sequenced usually from the 2^{nd} round to determine strong binders for the target material.

Phage display has been utilized by researchers to identify various peptides that bind to different types of materials. Belcher's group has successfully identified peptides capable of binding to GaAs [60], ZnS [27, 28, 31, 61], CdS [28, 31, 61], CoPt [31, 62], FePt [31], polypyrrole [63], carbon nanotubes [64]. Naik et al. identified peptides capable

of binding to Ag [65], CoPt [66] through biopanning. Phage display technique has been utilized to identify peptides capable to binding to Ti [67], germania [68], ZnO [69].

In this chapter we utilize first utilize the pIII library to identify copper sulfide binding sequences. The sequences were tested for their binding affinity though the results were not conclusive. A copper sulfide binding sequence was also genetically inserted in the pIII region of the template for binding study. Finally a pVIII library was used to perform biopanning against copper sulfide powder and screen binding sequences. The strongest binder was used for mineralizing copper sulfide. The mineralized material was characterized structurally and was identified to be a mixture of two phases of Cu_2S.

2.2 Experimental Details

2.2.1 Biopanning using pIII and pVIII library

For selecting a binding peptide in the pIII region, a 7 mer library (New England Biolabs, NEB) was utilized. For biopanning, 1.5 mg of Cu_2S powder was used and the pH level of all the TBST solutions used was fixed at 10.0 everywhere unless otherwise stated. The powder was washed 10 times in 0.5% Tween-20 in tris-buffered saline (0.5% TBST). After washing, a total of 10^{11} phages from 7 mer constrained library (NEB) was added to the powder with 1 mL of 0.1% TBST and kept on rocker. The phages were allowed to be adsorbed on to the Cu_2S for 30 minutes. After 30 minutes of incubation the suspended Cu_2S particles were centrifuged using a microcentrifuge and the supernatant containing unbound phages was discarded. The powder was washed 5 times with 0.1% TBST afterwards to remove any non-specific binding phages. After the five washes, 0.6

mL of 0.1% TBST was added to the powder to elute the bound phages. The solution was then briefly vortexed using a vortexer and then sonicated for 30 seconds using the sonicator. The powder was then centrifuged down and the supernatant removed in a separate sterile microcentrifuge tube. The phages were amplified for the next round immediately using standard amplification and polyethylene glycol (PEG) purification techniques for the M13 phage [70, 71]. To amplify the phages and infect the E. Coli cells with the phages, 35 ml of luria broth (LB) medium was combined with 350 µl of ER2738 (New England Biolabs) overnight culture and was inoculated with a single plaque. The solution was incubated at 37 C for 4.5 h with shaking. The E. coli cells were then pelleted at 4^0C and 10,000 rpm for 20 min, and the supernatant was transferred to a clean tube after centrifugation. Subsequently, 1/6 volume of 20% PEG/2.5 M NaCl (PEG/NaCl) was added to the supernatant and the phage was precipitated overnight at 4^0 C. The phages were then pelleted at 4^0 C and 10,000 rpm for 30 min and the supernatant discarded. To dissolve the phage pellet 1 ml of TBS was added and vortexed until the pellets were dissolved. The solution was spun for 5 min at 14,000 rpm to remove residual E. Coli cells and then the solution was transferred to a micro-centrifuge tube, and precipitated again with 1/6 volume PEG/NaCl on ice for 30 min. Finally, the phages were pelleted at 14,000 rpm for 10 min, the supernatant was discarded, and the phage pellet was dissolved in 200 µL of TBS. The concentration of the phage stock was measured using a spectrophotometer (Evolution 60, UV/vis). After amplification the amplified phage was used for the next round of biopan. Biopanning was carried out for five rounds. For the 4th and 5th round after incubation 0.5% TBST was used for washing to increase the

stringency. DNA sequencing of the phages was completed from 2nd round onwards to find any binding peptide. The peptide sequences from 4th and 5th round were analyzed individually to determine any consensus sequence.

An 8-mer M13 pVIII random peptide library was used for selection of Cu_2S binding peptides and was constructed using the method described in Lee et. al [62, 72]. The library had a random peptide insert 8 amino acids in length fused to each pVIII protein of the M13 virus and a complexity of 10^7 to 10^8. Each biopanning round was initiated with 10^{11} total phage. To minimize dissolution of the Cu_2S (Sigma-Aldrich) target material, all biopanning solutions were adjusted to pH 10. Before biopanning, the target material was washed 10 times in 0.5% Tween-20 in tris-buffered saline (0.5% TBST). Approximately 1.5 mg of Cu_2S powder was incubated with pVIII-modified phage for 30 minutes in 0.1% TBST. After incubation, the unbound phages were discarded and the Cu_2S powder was washed five times with TBST. The bound phages were eluted by sonication in 0.7% TBST for 30 s. The eluate was immediately titered and amplified for the next biopanning round. Clones from round five were sequenced to identify binding peptides.

2.2.2 Genetically engineered phage with pIII insert

The Cu_2S binding sequence His-Gly-Gly-Gly-His-Gly-His-Gly-Gly-Gly-His-Gly (HG12) was inserted into the pIII region of the M13 phage. The oligonucleotide CATGTTTCGGCCGAACCTCCACCACCATGACCACCACCATGACCATGACCAC CACCATGAGAGTGAGAATAGAAAGGTACCCGGG (IDT) was annealed with extension primer for 1 min at 95^0 C and then the temperature was lowered to below 37^0 C

in a thermal cycler. The annealed duplex was extended by mixing it with Klenow fragments at 37^0 C for 10 min then at 65^0 C for 15 min to deactivate the enzymes and afterwards keeping at room temperature. The extended duplex and the M13KE vector were digested with *Acc*65 I and *Eag* I. The extended duplex was digested for 4 h at 37^0 C and then at 65^0 C for 15 min and kept at 20^0 C afterwards. The M13SK vector was digested for 6 h at 37^0 C and then at 65^0 C for 20 min and finally kept at 20^0 C. After digestion, the digested duplex and the vector were purified using polyacrylamide gel and agarose gel respectively. The purified duplex and vector were ligated overnight for 16 hours at 16^0 C and heat treated to kill the enzymes. The ligated DNA was transfected into XL1-Blue electroporation competent cells and tittered.

2.2.3 Binding test

A binding test was performed with the sequences chosen from the biopanning rounds, and wild-type M13 phage. A total of 10^{11} phage was incubated with approximately 1.5 mg of Cu_2S powder for 30 min with shaking on rocker in 0.1% TBST. After incubation the unbound phage were discarded and the target material was washed three times with 0.5% TBST. The bound phages were eluted by sonication in 0.7% TBST for 30 s. The phages were titered immediately and the number of plaques were compared with each other.

2.2.4 Mineralization of copper sulfide

The pIII-modified and the pVIII-modified M13 clones observed with the highest frequency in biopanning as well as the HG12 clone was used for copper sulfide biomineralization. For HG12 phage mineralization, the phages (10^6 pfu/μL) were incubated for 12 hours in 1 mM $CuCl_2$ (Acros Organics) and 1 mM Na_2S (Acros Organics) was added to it and incubated. Two different incubation times for Na_2S were tested, 1 h and 12 h. The pIII modified phages were used for mineralization following the same method. For mineralization with the pVIII modified phage, an aqueous phage solution was placed on a gold transmission electron microscopy (TEM) grid and dried in a vacuum desiccator to fix the templates to the grid. The grid was incubated in 2 mM $CuCl_2$ (Acros Organics) for 12 hours, 2 mM Na_2S (Acros Organics) was added, and the incubation was continued for another 12 hours. Samples without phage templates were prepared in the same manner to serve as controls.

2.2.5 Structural and compositional analysis

Transmission Electron Microscope (TEM) was used to characterize the size, shape, morphology, and hierarchical structure of the biomineralized materials. To prepare samples for TEM, the sample grids were washed twice with deionized water after biomineralization. TEM images were acquired using either a Tecnai T-12 TEM at 120 kV or a Phillips CM300 TEM at either 200 or 300 kV. Energy dispersive x-ray spectroscopy (EDX) and electron diffraction on a Phillips CM300 TEM were used to find elemental composition and crystal structure, respectively.

2.3 Results and Discussion

2.3.1 Biopanning challenges

Using the standard procedure of biopanning which involves incubating Cu_2S with the phage in TBS at pH 7.4 for 1 h and then lowering the pH level to elute the bound phages from the target material did not yield any plaque. There could be various possibilities for no plaques. Cu_2S was found to be insoluble in water but soluble in acid [73]. The biopanning procedure involves the use of TBST as the incubation and washing solution, which is Tris Buffered Saline with Tween. Tween is a biological detergent and TBS contains Tris HCl. As a result Cu(I)S reacted with HCl and produced copper ions. The possible reaction taking place was: $Cu_2S + 2HCl = 2CuCl_2 + H_2S$, where $CuCl_2$ is soluble in water and produces copper ions. Tween has not been found to interact with Cu_2S to produce copper ions. The incubation in TBS may dissolve the Cu_2S which can remove the bound phages from the surface of the target material. Also, lowering the pH to elute bound phages would have the same issue of dissolving the Cu_2S. Cu_2S is less soluble at high pH. Therefore to test out the recovery of phages the pH of the incubation solution was varied from 9 to 12 and percentage of recovered phages calculated. Also two different incubation times were tested 30 min and 45 min. The results are shown in figure 4. An incubation time of 30 min and pH of 10 was chosen for the biopanning.

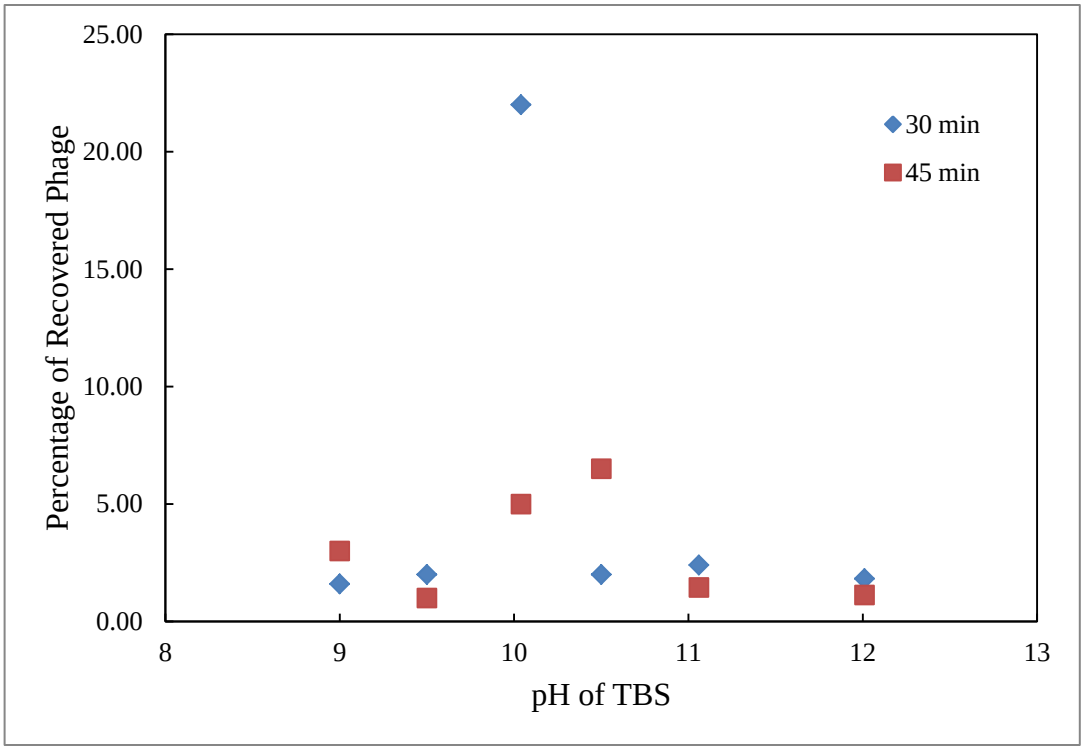

Figure 4. Percentage of phage recovered vs. varying pH level of TBS. Data is shown for phages recovered after 30 and 45 minutes of incubation with the TBS adjusted at the particular pH level.

We also needed to address the use of a low pH solution during chemical elution. The elution step in the biopanning technique required changing the pH of the solution to a much lower level. But changing the pH to a lower level would increase the solubility of Cu_2S. So, another elution technique was needed. An alternative to the chemical elution technique is physical elution, which was used to select binding peptides of mica ($KAl_2(AlSi_3O_{10})(OH)_2$) [59]. Using ultrasonication to disrupt the peptide-inorganic material binding interaction, this technique was successfully applied as an alternative to the chemical elution step [59]. So, we chose to use an ultrasonicator for eluting the bound phages from Cu_2S.We chose a 30 seconds ultrasonication time for our elution step at a

power level of 80 Watts and at a frequency of 40 kHz. After solving the biocidal effect of copper, the phage display technique was ready to be applied for Cu_2S.

2.3.2 Material specific pIII sequences

Biopanning was carried out for five rounds. DNA sequencing of the phages were done from 2^{nd} round onwards to find any binding peptide. The sequence Z58 (YRAPWPP) was present four times in the 5^{th} round of biopanning. The peptide sequences from 4^{th} and 5^{th} round were analyzed individually to determine any consensus sequence which is shown in table 1.

Table 1. Statistical analysis and resultant consensus sequence found from individual amino acids.

Amino Acids	Percentages by Position (%)							Observed frequency (%)	Library Frequency (%)
	pos1	pos2	pos3	pos4	pos5	pos6	pos7		
Phe	0.00	0.00	9.09	0.00	4.55	0.00	0.00	1.95	1.70
Trp	4.55	0.00	4.55	0.00	18.18	9.09	0.00	5.19	2.40
Met	0.00	0.00	4.55	0.00	4.55	0.00	4.55	1.95	3.40
Pro	0.00	18.18	4.55	40.91	18.18	31.82	40.91	22.08	14.00
His	9.09	0.00	9.09	4.55	0.00	4.55	9.09	5.19	4.60
Lys	0.00	4.55	0.00	0.00	0.00	0.00	0.00	0.65	3.00
Arg	0.00	18.18	0.00	0.00	9.09	18.18	4.55	7.14	4.40
Asn	4.55	0.00	0.00	4.55	0.00	9.09	0.00	2.60	3.30
Gln	9.09	4.55	4.55	4.55	4.55	0.00	0.00	3.90	3.60
Glu	0.00	0.00	0.00	0.00	4.55	0.00	0.00	0.65	1.70
Asp	0.00	0.00	0.00	9.09	0.00	0.00	0.00	1.30	1.90
Val	4.55	0.00	0.00	0.00	0.00	4.55	4.55	1.95	4.30
Gly	9.09	0.00	0.00	0.00	0.00	0.00	0.00	1.30	3.90
Ala	18.18	13.64	18.18	4.55	9.09	0.00	4.55	9.74	6.90
Ile	0.00	9.09	13.64	4.55	0.00	4.55	9.09	5.84	3.60
Leu	4.55	4.55	9.09	9.09	4.55	9.09	9.09	7.14	10.00
Thr	4.55	0.00	18.18	4.55	9.09	4.55	9.09	7.14	8.40
Ser	9.09	22.73	4.55	4.55	9.09	4.55	0.00	7.79	11.60
Tyr	22.73	4.55	0.00	9.09	4.55	0.00	4.55	6.49	4.10
Cys	0.00	0.00	0.00	0.00	0.00	0.00	0.00	0.00	0.57
Individual Consensus	Y	S	A	P	W	P	P		
			T		P				

From table 1 it can be seen that the consensus sequence is predominantly proline rich. The amino acids were grouped as shown in figure 5 for further analysis.

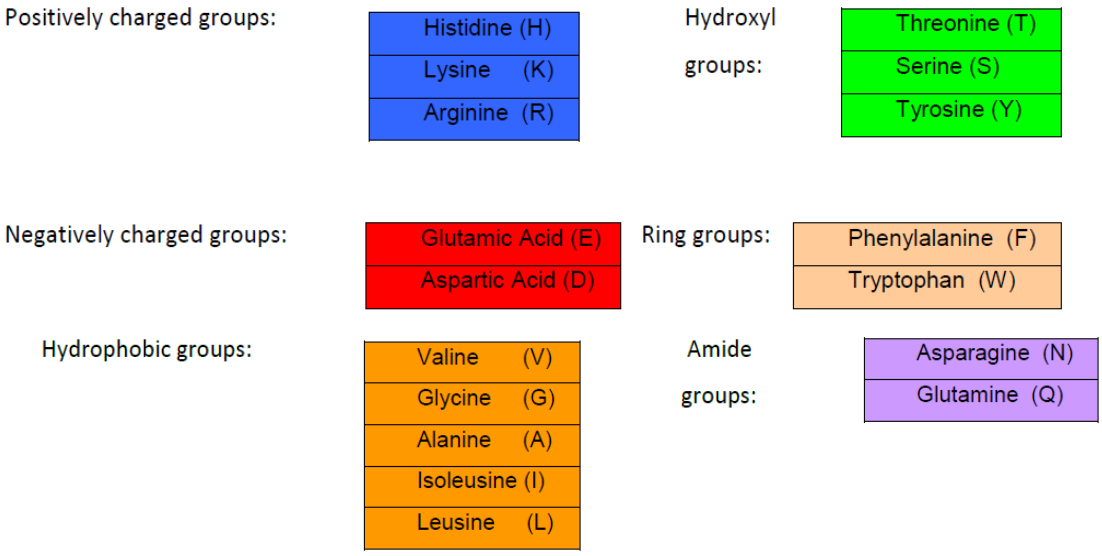

Figure 5. Amino acid groups

Proline (P) and Methionine (M) were not grouped with any other amino acids.

The sequences were analyzed to see if there was any trend so as to confirm that the biopanning process was working. The result of the analysis is shown in figure 6.

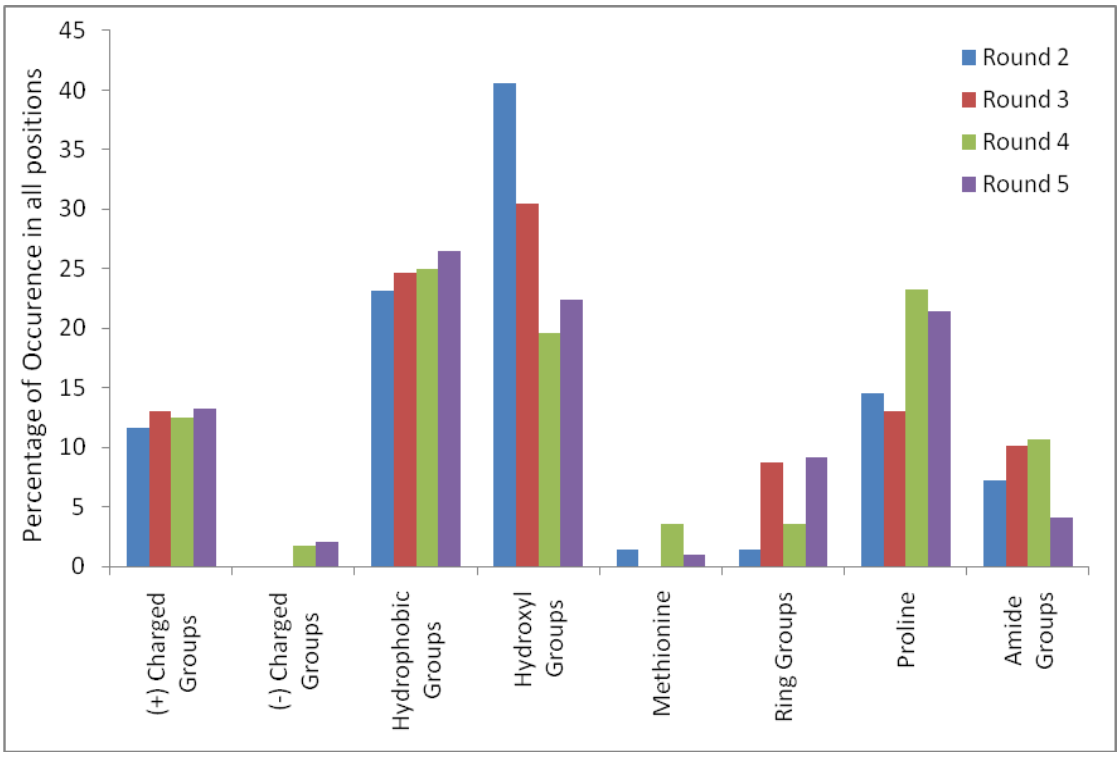

Figure 6. Percentage of occurrence of amino acids combined in all positions vs. different groups of amino acids.

As seen from figure 6, the hydrophobic groups were increasing in percentage from 2nd to 5th round. On the other hand there was a decrease in the hydroxyl groups from round 2 to round 5. Also there was an increase in the percentage of Proline as well. The positively charged groups seem to remain more or less constant in different rounds. So there are trends in the proline, hydrophobic and hydroxyl groups indicating that the biopanning may be working.

From the biopanning rounds, it can be seen that it was not until the 5th round that a particular sequence Z58 (YRAPWPP) came multiple times. This sequence also had the last four positions same as the consensus sequence. This sequence was chosen for the

binding study. But it was not sure whether or not this sequence had the strongest binding affinity or it just had a higher replication rate. So, two other sequences were also chosen in addition to this one for the binding study. The first one was Z515 (HAIYPRH). This sequence was chosen as it also came in the 4^{th} round. The second one was Z41 (GSMPRTP). This sequence was chosen using the sequence pattern discovery tool from IBM Computational Biology Center by grouping the amino acids in hydrophobic, hydroxyl, positive, negative, ring and amide groups. The sequence pattern chosen was [AGIL][STY] . . [RHK] as this pattern occurred the most number of times.

2.3.3 Material specific pVIII sequences

After five rounds of biopanning six unique amino acid sequences were identified. Each of these six peptides is shown in table 2 with the frequency at which it was found among the selected clones and its calculated isoelectric point. Compared to the library, the identified peptides were rich in basic, hydrophobic, and polar residues; however the peptides were still net negatively charged under incubation conditions as indicated by their calculated isoelectric points (pH 4-4.37). Over half of the clones sequenced (16 of 24) displayed the same peptide: DTRAPEIV. Notably, this peptide is lacking histidine, an amino acid known to be integral in binding copper or copper sulfide compounds [25, 74-76]. Binding may be caused by electrostatic interactions between the net negatively charged pVIII proteins and positively charged copper ions [77, 78]. Alternatively, $-NH_2$ terminated side groups, such as those found at the peptide N-terminus and in arginine, have also demonstrated Cu_2S binding capabilities [79]. Further investigation is required to determine the dominant binding mechanism for this peptide. Because of the frequency with which it appeared in the final biopanning round, the clone with the DTRAPEIV pVIII peptide fusion was selected for biomineralization experiments.

Table 2. Statistical analysis and resultant consensus sequence found from individual amino acids.

Amino Acids	Percentages by Position (%)								Obs. Freq. (%)	Library Freq. (%)
	pos1	pos2	pos3	pos4	pos5	pos6	pos7	pos8		
Phe	0.00	0.00	0.00	0.00	0.00	0.00	0.00	0.00	0	0.89
Trp	0.00	0.00	0.00	0.00	0.00	0.00	0.00	0.00	0	0.89
Met	0.00	0.00	0.00	0.00	0.00	0.00	4.35	0.00	0.62	1.79
Pro	0.00	0.00	4.35	0.00	73.91	0.00	8.69	0.00	12.42	14.29
His	0.00	0.00	0.00	0.00	0.00	0.00	0.00	0.00	0	0
Lys	0.00	4.35	13.0	0.00	0.00	0.00	0.00	0.00	2.48	0.89
Arg	0.00	0.00	78.3	0.00	0.00	0.00	0.00	0.00	11.18	5.36
Asn	0.00	0.00	0.00	0.00	4.35	0.00	0.00	0.00	0.62	1.79
Gln	0.00	0.00	0.00	0.00	0.00	0.00	0.00	0.00	0	6.25
Glu	0.00	0.00	0.00	0.00	4.35	73.91	8.69	13.04	12.42	16.07
Asp	95.7	0.00	0.00	0.00	0.00	0.00	0.00	0.00	13.66	8.04
Val	4.35	13.04	0.00	0.00	0.00	8.69	0.00	69.57	3.73	5.36
Gly	0.00	0.00	0.00	0.00	8.69	0.00	0.00	0.00	1.24	8.93
Ala	0.00	0.00	0.00	73.9	8.69	8.69	8.69	0.00	14.29	6.25
Ile	0.00	0.00	0.00	0.00	0.00	0.00	69.57	0.00	9.94	0.89
Leu	0.00	8.69	0.00	0.00	0.00	0.00	0.00	0.00	1.24	1.79
Thr	0.00	73.91	0.00	8.69	0.00	4.35	0.00	8.69	12.42	8.93
Ser	0.00	0.00	4.35	17.4	0.00	4.35	0.00	8.69	3.73	11.61
Tyr	0.00	0.00	0.00	0.00	0.00	0.00	0.00	0.00	0	0
Cys	0.00	0.00	0.00	0.00	0.00	0.00	0.00	0.00	0	0
Individual Consensus	D	T	R	A	P	E	I	V		

2.3.4 Binding test results

The sequences selected from the pIII and pVIII insert phage were compared with M13 phage as a control in the binding test. The binding tests of the pIII inserted phages are shown in figure 7. From the figure it can be seen that all of the phages have a greater binding affinity compared to M13. The phages seem to have some affinity towards Cu_2S.

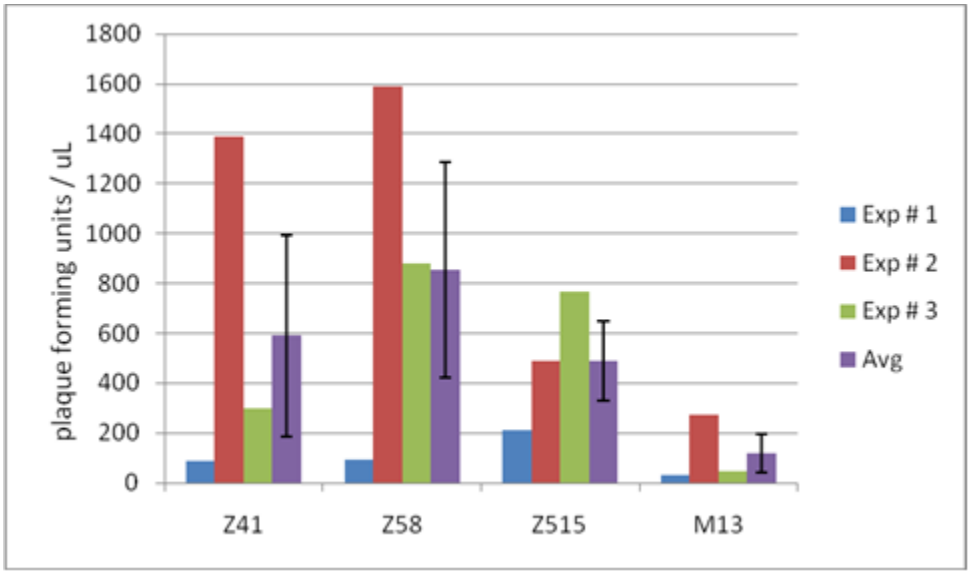

Figure 7. Plaque forming units per micro liter vs. different peptide sequences used in binding study. The binding test was done three times and averaged.

But when the binding test was repeated again it was found that the results were not repeatable and in some cases the M13 phage had a higher affinity than the binding phages.

Similarly the pVIII inserted sequence DTRAPEIV (Np8-44) was also compared to the M13 phage. The result of the binding study is shown in figure 8. From figure 8 it is also clear that the binding of the phage to Cu_2S was not conclusive.

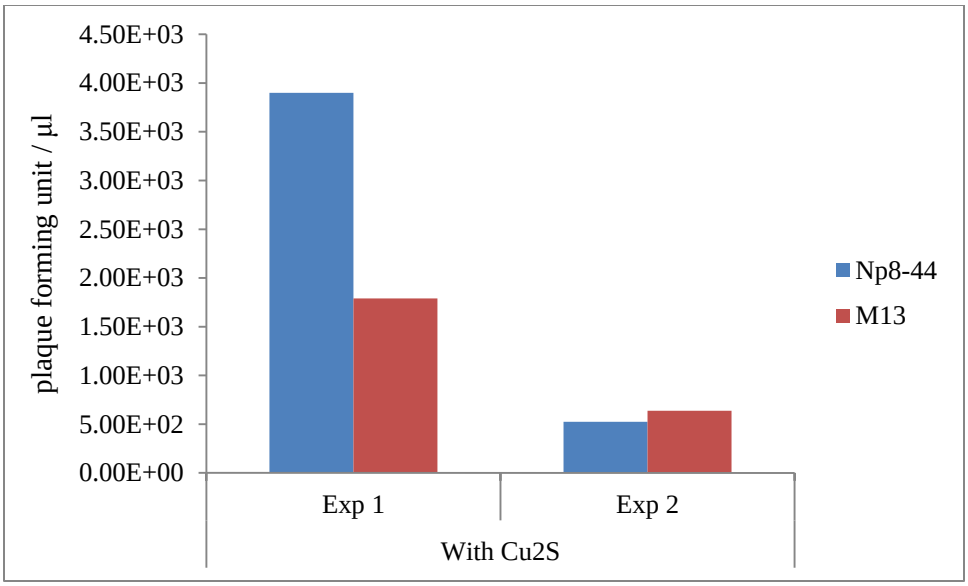

Figure 8. Binding test of Np8-44 phage and M13 phage. The test was repeated twice to show the variability in the binding study results.

2.3.5 Mineralizing copper sulfide with specific pIII and pVIII sequences

The HG12 phage and the phages identified from both the pIII and pVIII biopanning rounds were used for mineralizing copper sulfide. As can be seen from figure 9, the HG12 phage was most probably bound to some self-nucleated material. To determine the effect of increasing the incubation time on the nucleated particles the incubation time with Na_2S was increased to 12 h and TEM images were taken afterwards. The TEM image of the phage is shown in figure 10. As can be seen there were nanoparticles found all over the phage template rather than just at the pIII end. This indicated that there could be nucleation all over the phage template which could be due to some other mechanism than a specific binding affinity for Cu_2S.

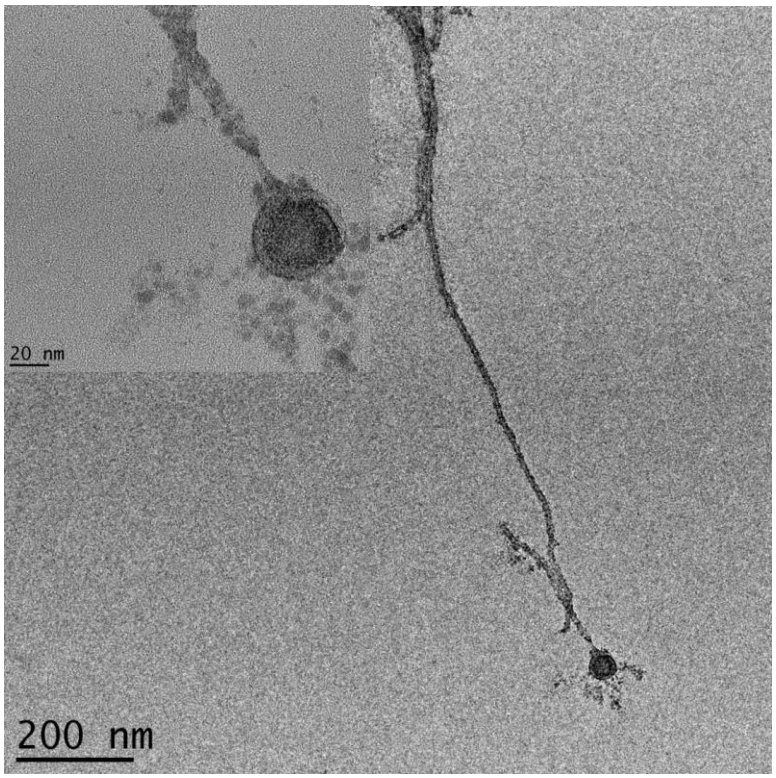

Figure 9. TEM image of mineralization with HG12 phage. Inset: Higher magnification image of the particle bound to the phage.

The inset of figure 10 shows that these nanoparticles were smaller than 20 nm in size and were aligned randomly on the phage templates.

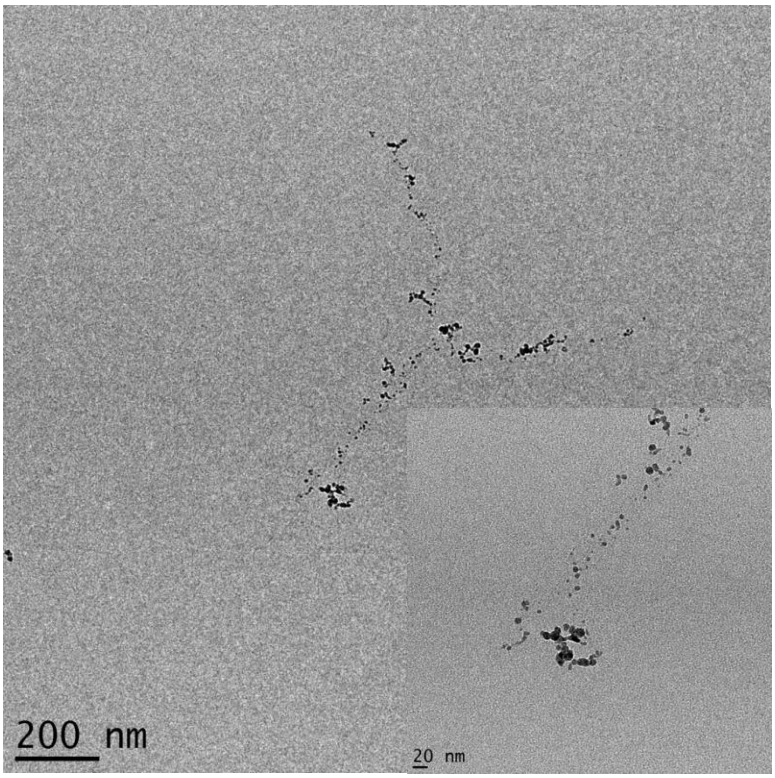

Figure 10. TEM image of HG12 phages mineralizing nanoparticles. The phages were incubated for 12 h in $CuCl_2$ and 1 h in Na_2S. Inset: Higher magnification image of the nanoparticles on the phage template.

The Z58 phage (YRAPWPP) was next selected for nucleation. The TEM image of the nucleated phages is shown in figure 11. As can be seen from the image these phages also had nucleated particles on the entire template.

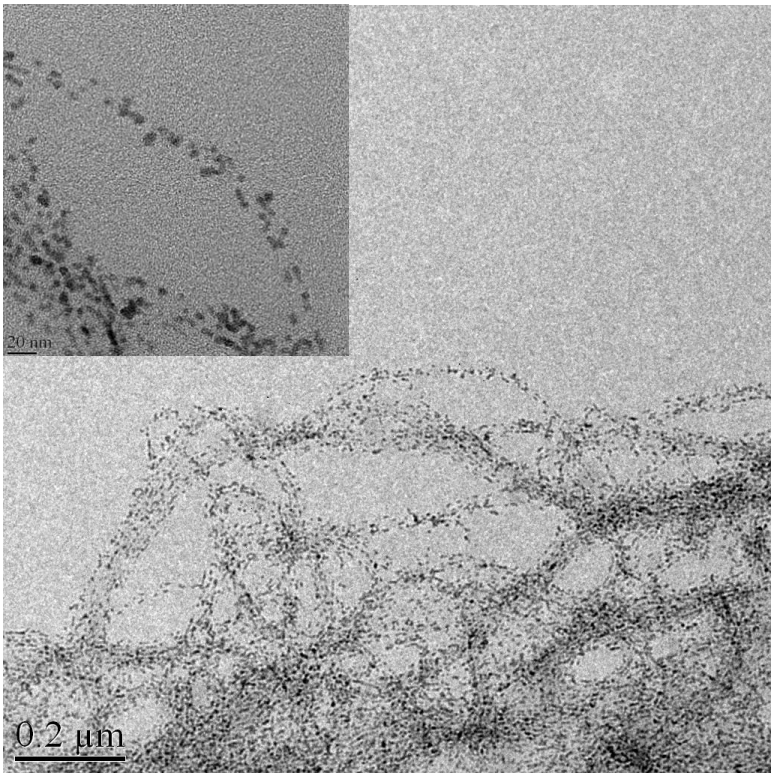

Figure 11. TEM image of nucleated material on Z58 phage. The phages were incubated 12 h with $CuCl_2$ and 12 h with Na_2S.

TEM images of unstained, viral-templated copper sulfide using the pVIII inserted phages are shown in figure 12 with a representative EDX spectrum in figure 13 and an electron diffraction pattern in figure 14. The biomineralized nanoparticles were irregularly shaped. The particle size distribution determined from TEM images is shown in figure 15. The median particle diameter is 6.5 nm. The nanoparticles were arranged in chain-like structures. The nanoparticle coverage of the template was incomplete and non-uniform with large gaps frequently observed between nanoparticles. Banerjee et al.

previously reported biomineralized Cu_2S nanoparticles 12 to 22 nm in diameter using bionanotube templates. In comparison, the viral-templated nanoparticles were smaller in diameter, but less densely packed along the template and less monodisperse [74]. The EDX spectrum confirmed the presence of Cu and S within the biomineralized material, as well as O. The Au and C peaks were attributed to the grid, whereas the silicon internal fluorescence peak from the detector was the source of the Si peak. The d-spacings determined by the electron diffraction pattern were attributed to the (100), (102), (104), and (110) planes of high chalcocite and the (240) plane of low chalcocite, indicating a mixture of copper sulfide compositions was present. Furthermore, d-spacings characteristic of the (110), (-112), and (-113) planes of CuO were also observed.

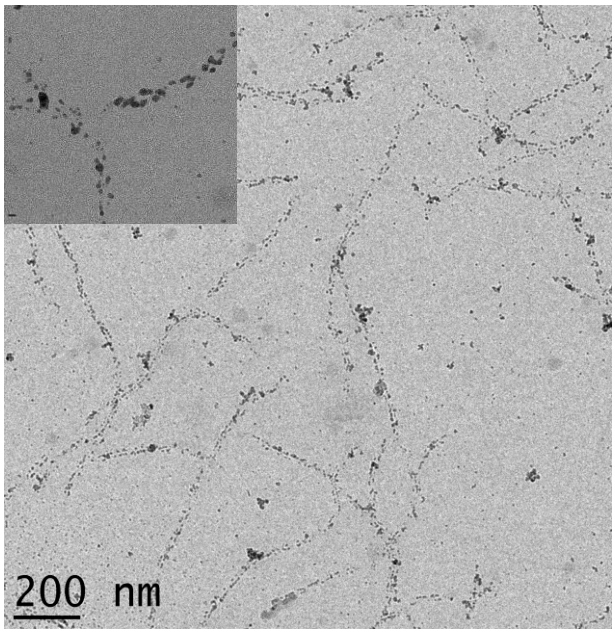

Figure 12. Linear chains of copper sulfide nanoparticles templated on the pVIII protein of Cu_2S-binding phage. Inset: A high magnification TEM image of viral-templated nanoparticles (scale bar is 10 nm).

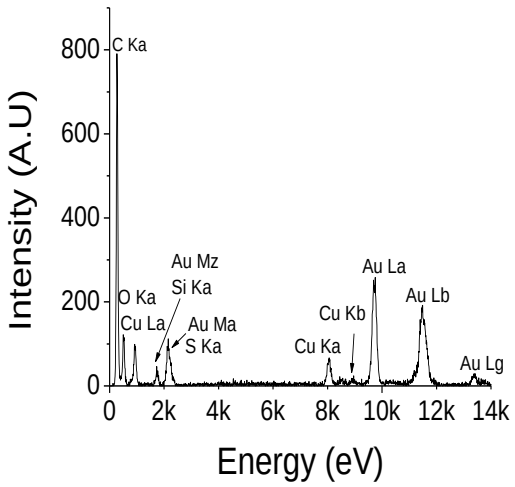

Figure 13. EDX spectrum showing the presence of elemental Cu and S.

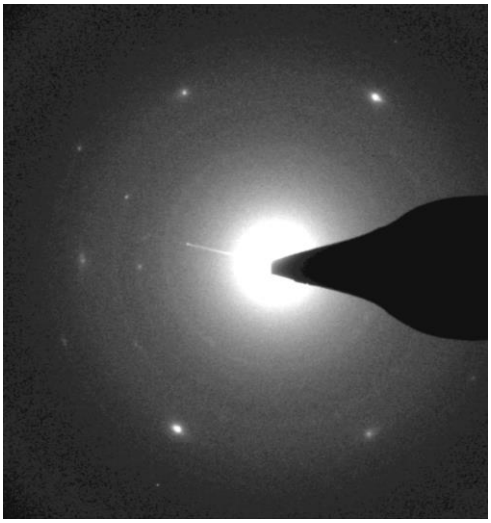

Figure 14. An electron diffraction pattern showing the biomineralized material to be of a mixture of high and low chalcocite phase.

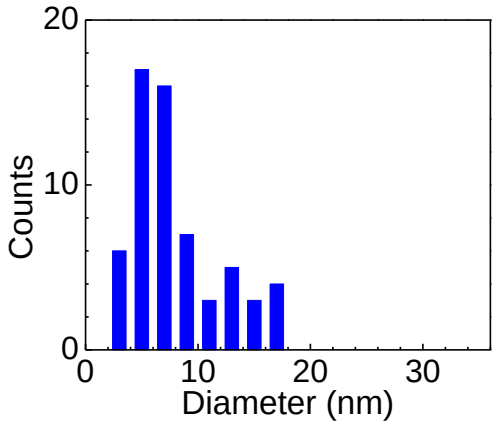

Figure 15. Size distribution of biomineralized copper sulfide nanoparticles.

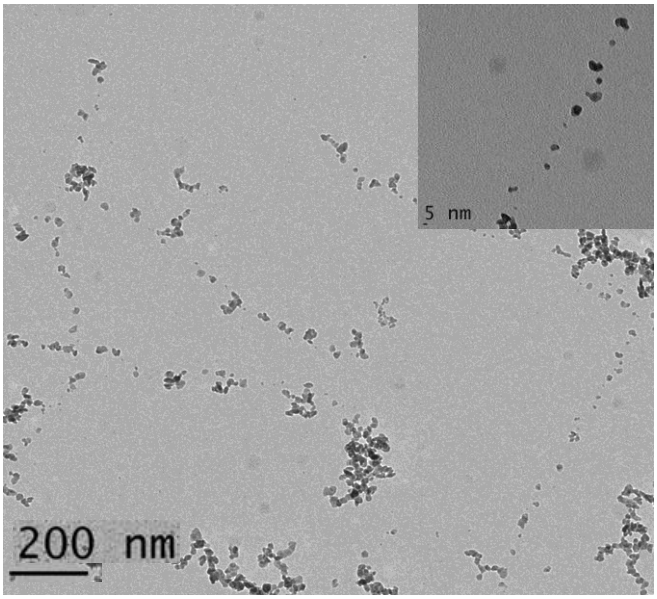

Figure 16. TEM image of phage templates with nanoparticles after 48 h of incubation period.

The effect of increasing the incubation time on the nanoparticles were also investigated. The incubation time was varied from 12 h to 48 h. A representative image

for a 48 h incubation time is shown in figure 16. As can be seen from the figure the nanoparticles grew in size. In spite of growing in size, large gaps were present between the nanoparticles. A histogram of nanoparticle size with incubation time is shown in figure 17. It can be seen that as the incubation time was increased the particle size also increased from 6 nm to 48 nm from 12 h to 48 h.

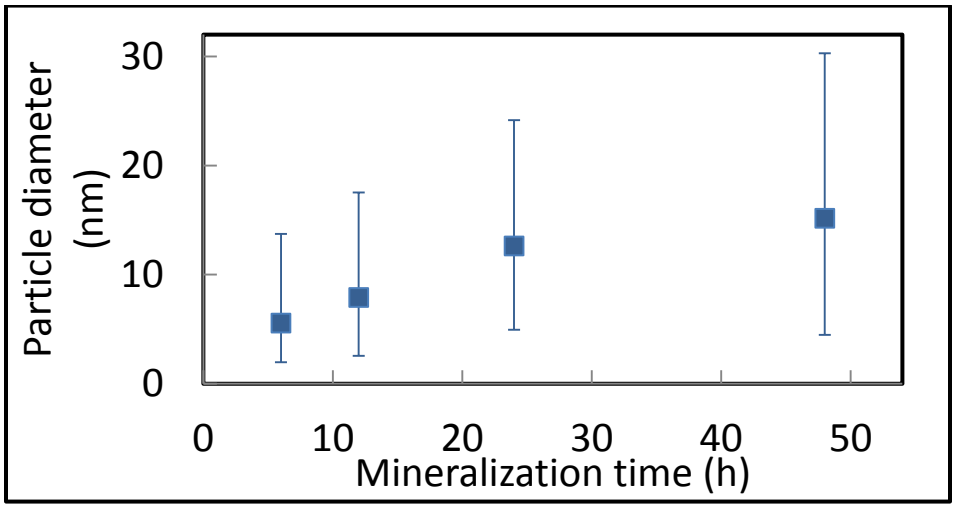

Figure 17. Histogram of nanoparticle size as a function of mineralization time.

In addition to the linear chains of nanoparticles, individual nanoparticles and clusters of nanoparticles were observed with TEM. These particles were attributed to spontaneous or untemplated particle formation. During biomineralization, we believe that the copper ions from the $CuCl_2$ form complexes with the peptides which produce copper sulfide nanocrystals upon addition of the Na_2S. Control samples made without a phage template did not produce linear chains of nanoparticles, but rather larger clusters of nanoparticles without a hierarchical structure.

2.4 Conclusion

We have utilized the phage display technique to identify pIII and pVIII sequences against Cu_2S powder. The sequences YRAPWPP and DTRAPEIV from the pIII and pVIII library respectively had the most number of occurrences. These sequences were chosen for subsequent binding test and mineralization experiments. The binding tests were not conclusive and their binding affinity towards Cu_2S could not be proved definitely. This was mostly due to fact that large variations were observed from titering the different phages with Cu_2S. The large variation made it difficult to draw any conclusion about the binding of the phages. Nonetheless, these phages along with the HG12 phage was used for mineralizing copper sulfide. The HG12 phage had a Cu_2S binding peptide sequence inserted at the pIII end of the phage. The nucleation with the HG12 phage did not result in conclusive nucleation on the pIII end. The nucleation experiment with the pIII inserted sequence resulted in mineralization of small nanoparticles all over the length of the phage template. This indicated some other nucleation mechanism was taking place which promoted the growth of the nanoparticles along the length of the virus. When the pVIII inserted sequence was used for mineralization discontinuous coverage of small nanoparticles was found along the length of the phage template. The mean particle size increased from 6 nm to 48 nm from 12 h to 48 h incubation. The material was found to be a mixture of different phases of copper sulfide. Though the phages were able to mineralize copper sulfide, the yield was low. This required another nucleation method more reliable and with high yield.

3 Copper Sulfide Mineralization using Non-specific Interactions

3.1 Introduction

Often, in Nature, molecules such as peptides and proteins closely control mineral composition and/or structure, optimizing them for specific functions. For example, magnetotactic bacteria form nearly stoichiometric magnetite (Fe_3O_4) for navigation; abalones control growth of calcium carbonate polymorphs, aragonite and calcite, to create robust shells. Because the phase diagram of copper sulfide is complex with many polymorphs, some of which are non-stoichiometric, it is a particularly intriguing material system in which to study bio-assisted synthesis. Biomolecules of a variety of sizes, shapes, and hierarchical structures have been used to induce growth of different copper sulfide compounds in a laboratory environment. Simple amino acids such as alanine and cysteine have served as capping ligands for CuS formation [80, 81]. Colloidal synthesis using alanine at pH 10 created polydisperse, mixed morphology (i.e. spheres, triangles, and rods) CuS particles tens of nanometers in size [80]. The hydroxyl group of alanine readily attached to CuS at high pH. A hydrothermal reaction using cysteine as both a stabilizing agent and a sulfur source resulted in hierarchical CuS microstructures including snowflakes, flowers, and porous shells [81]. Furthermore, small proteins such as bovine serum albumin (BSA) have also been used as capping molecules for copper sulfide synthesis [82]. Cu_2S and CuS nanoparticles were both successfully formed in colloidal solution using BSA. The sulfhydryl or imidazole groups within BSA likely

contribute to protein–metal cation interactions making particle formation possible. Larger biomolecules with hierarchical structures have also demonstrated an ability to mineralize copper sulfide, improving control over particle size distribution and long range particle geometry. For example, apoferritin, a cage protein which is composed of 24 subunits arranged in a spherical geometry, has been used to produce monodisperse CuS nanoparticles [83]. The pore diameter of this multi-component protein constrained material growth resulting in tight control of nanoparticle size. Additionally, nanocrystalline tubes of Cu_2S have been mineralized using bionanotube scaffolds approximately 100 nm in diameter and several microns in length [74]. HG12, a histidine-rich peptide, was displayed along the length of each bionanotube with a 6.4 nm spacing [20, 25, 74]. The imidazole in histidine served to template monodisperse Cu_2S nanoparticles along the length of each tube. Furthermore, the pH of the precursor solution was used to control the aggregation of the peptides along the bionanotubes and vary the average nanoparticle diameter from 12 nm (pH 5) to 22 nm (pH 8). The well-organized, hierarchical organization of the high affinity biomolecules enabled both the particle size and the larger scale geometry of the mineralized material to be engineered. The non-specific electrostatic interactions have been used to synthesize various metals and semiconductors. The non-specific interactions between fd and M13 phages and Ca^{2+} and Zn^{2+} ions have been utilized to mineralize hydroxyapatite and ZnS [84, 85]. Cu metal was mineralized on TMV virus using the electrostatic interactions [77]. The M13 virus was used as a biological scaffold to mineralize Ru, Rh and Pd metal on the viral coat protein [86].

In this chapter, the growth of copper sulfide driven by non-specific electrostatic interactions using a genetically-modified, carboxyl-rich M13 template is explored. The closely-spaced, hierarchically-ordered binding sites enabled the formation of high quality, optically-active $Cu_{1.8}S$ nanocrystalline material in which both band-to-band and free carrier absorption were observed.

3.2 Experimental Details

3.2.1 Genetic Engineering of M13 phage to insert E3 sequence

A genetically-modified virus was used as the template for the synthesis of copper sulfide. The N-terminus of the 2700 copies of the pVIII coat protein of the wild-type M13 virus was genetically modified to fuse three glutamic acid residues (E3) using a previously reported approach [62, 87]. The N-terminal of the wild-type phage consists of AEGD-, which was replaced with a more negatively charged amino acid sequence AEEE- using the M13SK vector [33, 88]. The PstI and BamHI restriction sites were introduced via a mutation (T to A) at position 1372 and a mutation (C to G) at position 1381, respectively, and a PstI restriction site was removed by a mutation (T to A) at position 6250 [62]. To construct the E3 phage, the oligonucleotide 50-CT ACT ACA AGG ATC CTC CTC CTC TGC AGC GAA AGA CAG CA-30, encoding the three glutamic acids, was hybridized and polymerase chain reaction (PCR) amplified. The circular M13SK vector and the oligo duplex were digested with PstI and BamHI, ligated together, and transformed into XL-1 Blue electrocompetent cells with an electroporator (BioRad, MicroPulser). The transformed cells were titered, and the bacteriophage DNA

was sequenced in the region encoding for the pVIII coat protein to confirm the peptide fusion.

A phage stock solution with a concentration of 10^{10} pfu/μL in tris-buffered saline was prepared using standard amplification and polyethylene glycol (PEG) purification techniques for the M13 phage [70, 71]. The tris-buffered saline contains 50 mM Tris-HCl, 150 mM NaCl and the pH of the buffer was adjusted to 7.5. To amplify the phages and infect the E. Coli cells with the phages, 500 ml of luria broth (LB) medium was combined with 5 ml of ER2738 (New England Biolabs) overnight culture and was inoculated with a single plaque. The solution was incubated at 37 C for 8 h with shaking. The E. coli cells were then pelleted twice at 4^0 C and 10,000 rpm for 20 min, and the supernatant was transferred to a clean tube after each centrifugation. Subsequently, 1/6 volume of 20% PEG/2.5 M NaCl (PEG/NaCl) was added to the supernatant and the phage was precipitated overnight at 4^0 C. The phages were then pelleted at 4^0 C and 10,000 rpm for 10 min and the supernatant discarded. To dissolve the phage pellet 1 ml of TBS was added and vortexed until the pellets were dissolved, then the solution was transferred to a micro-centrifuge tube, and precipitated again with 1/6 volume PEG/NaCl on ice for 60 min. Finally, the phages were pelleted at 10,000 rpm for 10 min, the supernatant was discarded, and the phage pellet was dissolved in 100 μL of TBS. The concentration of the phage stock was measured using a spectrophotometer (Evolution 60, UV/vis) and diluted as necessary with TBS to obtain a phage stock concentration of 10^{10} pfu/μL.

3.2.2 Mass spectroscopy analysis

The insertion of the E3 peptide was confirmed by matrix-assisted laser desorption/ionization time-of-flight mass spectrometry (MALDI-TOF MS, QSTAR XL oMALDI MS/MS) and was performed on the pVIII protein. Samples were prepared by incubating 100 μL of 3.85 x 10^{10} pfu/μL of M13 phage with 25 μL of 6 M guanidine hydrochloride at room temperature for 5 min for denaturation. The salts and other small molecules left after the denaturation were removed using a molecular weight cut-off filter (Vivaspin 500 MWCO 3000). The purified, denatured protein was mixed with acetonitrile, trifluoroacetic acid, and alpha-cyano-4-hydroxycinnamic acid matrix and spotted on the matrix plate.

3.2.3 Mineralization of copper sulfide

Nanocrystalline copper sulfide was mineralized by sequential incubation of the E3 phage template in copper chloride ($CuCl_2$) and sodium sulfide (Na_2S) chemical precursors as shown in figure 18. Stock solutions of 1 M $CuCl_2$ (Acros Organics) and 1 M Na_2S (MP Biomedicals) were prepared in deionized water and then diluted to concentrations of 200 mM and 1 mM, respectively, for use as precursors. The E3 stock solution was diluted 1:10 with deionized water. Crystallization was performed by first combining 100 μL of 200 mM $CuCl_2$ and 100 μL of the diluted E3 phage solution for a total volume of 200 μL. The solution was vortexed to ensure mixing and allowed to incubate undisturbed for 2 hours. The phage templates were pelleted by centrifugation. The excess $CuCl_2$ precursor solution was removed leaving the pellet intact, and 100 μL of 1 mM Na_2S was added. The phage templates were incubated in the Na_2S precursor

solution for 5 min with sonication. For comparison, samples with wild-type M13 phage and without a phage template were made in a similar manner. In addition, the E3 phage template was added to a solution of pre-formed nanoparticles synthesized without a template.

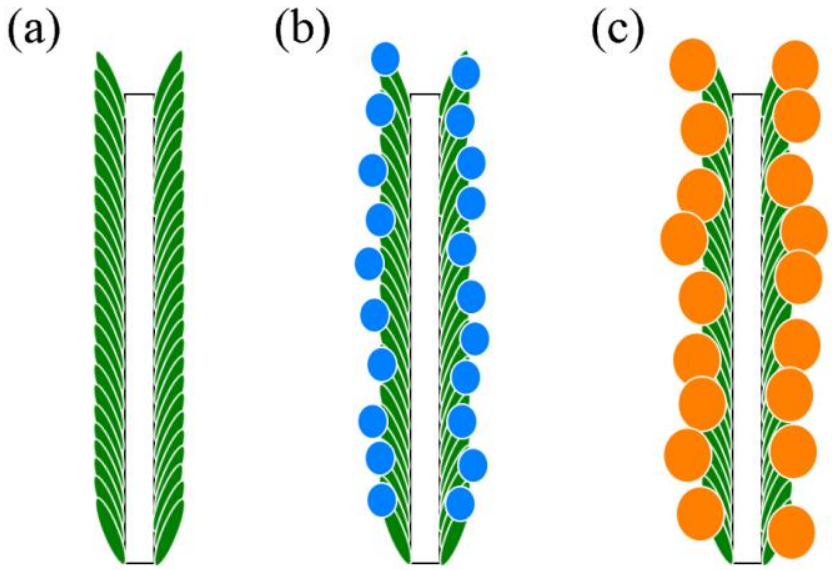

Figure 18. Schematic of the viral-templated crystallization process. (a) E3 phage template shown with the modified pVIII protein (green ovals) (b) copper ions (blue circles) bound to the pVIII protein during incubation with $CuCl_2$ (c) $Cu_{1.8}S$ nanocrystals (orange circles) formed along the length of the phage after addition of Na_2S.

3.2.4 Electrostatic interaction investigation

Electrostatic interactions between the viral template and copper cations were investigated using zeta potential measurements and transmission electron microscopy (TEM, FEI Tecnai12 and CM300) of phage agglomerates formed during incubation with $CuCl_2$. The zeta potential of the E3 template in TBS with and without the addition of $CuCl_2$ was measured at room temperature using a zeta potential analyzer (Malvern

Zetasizer Nano ZS). A phage concentration of 2.5 x 10^8 pfu/μL and total volume of 600 μL were used for all measurements. The E3 stock solution was diluted with TBS to half the original concentration. Samples were prepared by diluting 30 μL of this phage solution (5 x 10^9 pfu/μL) in deionized water or 0.5 mM $CuCl_2$. Low concentrations of $CuCl_2$ and E3 phage template were used for zeta potential measurements to avoid significant agglomeration. For each solvent, three samples were measured ten times and averaged. Wild-type M13 phage samples were similarly prepared and measured for comparison. In addition, TEM was used to study the phage agglomeration behavior associated with the presence of $CuCl_2$ in solution. For these samples, the E3 stock solution was diluted 1:10 with deionized water and an equal volume of 2 mM $CuCl_2$ was added for a total volume of 200 μL. The solution was vortexed to ensure mixing, then 5 μL volume of solution was immediately drop cast onto a carbon-coated nickel grid, incubated for 5 min, rinsed twice with deionized water, and stained with 2% uranyl acetate. The $CuCl_2$ concentration used here was lower than that used for copper sulfide synthesis. Lower $CuCl_2$ concentration avoided the formation of extremely large agglomerates which might be easily removed from the TEM grid during rinsing steps, preventing accurate analysis of agglomerate size. TEM samples were similarly prepared with wild-type M13 phage for comparison.

3.2.5 Structural characterization

The morphology of the synthesized material, as well as the nanocrystal geometry and size were characterized by TEM. Electron diffraction and energy dispersive x-ray (EDX) spectroscopy were used to determine the crystal structure and elemental

composition, respectively. To prepare samples for TEM, a 5 μL volume of suspended synthesis products was drop cast onto a carbon-coated nickel grid, incubated for 5 min, and then rinsed twice with deionized water. Bright-field TEM was used to determine the morphology of the synthesis products, as well as to quantify the widths of individual phage encrusted by copper sulfide nanoparticles and the width of phage bundles coated with nanoparticles. Phage bundles were defined as several phage aligned side-by-side forming a structure greater than one phage in width and length. Twenty-two bundles were each measured at several locations along their length to obtain an average width. The average width of individual phage overgrown with copper sulfide nanoparticles was measured in a similar fashion. Individual phage widths were only measured where nanocrystalline copper sulfide material was clearly visible.

3.2.6 Optical characterization

The room-temperature optical absorption of thin films of the phage and copper sulfide aggregates was measured from 360 to 3300 nm with a spectrophotometer (Cary 500 UV/Vis/NIR), neglecting reflection and scattering effects. To prepare samples for absorption measurements, the phage coated with copper sulfide were rinsed with deionized water to remove residual precursor solution and un-templated material, and then concentrated. To rinse the material, the mineralized phages were loosely pelleted through low speed centrifugation, the supernatant was removed, and the pellet was re-suspended in deionized water. Concentration was achieved through low speed centrifugation and partial removal of the deionized water supernatant. The remaining concentrated synthesis products were deposited on a glass slide and dried in a vacuum

desiccator for approximately 10 minutes. The optical absorption of the film was then measured from 360 nm to 3300 nm.

3.3 Results and Discussion

3.3.1 Insertion of E3 Peptide in the Virus Coat Protein

The DNA sequence of the E3 bacteriophage confirmed the fusion of the AEEE-peptide at the N-terminus of the pVIII protein. Furthermore, MALDI-TOF MS performed on the genetically-modified and wild-type M13 pVIII proteins was consistent with the replacement of the wild-type N-terminus amino acid sequence (AEGD-) with the E3 sequence (AEEE-). MALDI-TOF MS was used to confirm the display of three glutamic acids on the pVIII coat protein of the genetically-modified E3 phage. As shown in figure 19, sharp peaks at m/z 5236 and 5323 were observed for the wild-type M13 and E3 major coat proteins, respectively. These molecular weights are consistent with the theoretical values for wild-type M13 (5238 Da) and E3 (5324 Da) pVIII proteins. Furthermore, the 87 Da difference observed between the two proteins was consistent with the theoretical 86 Da molecular weight difference associated with replacing the wild-type M13 N-terminus peptide sequence, AEGD-, with AEEE-. These data corroborated the successful genetic modification and display of three glutamic acids on the pVIII coat protein of the E3 phage. As expected, the addition of an acidic amino acid to the major coat protein increased the net negative charge of the E3 phage compared to the wild-type M13 phage [33, 87, 88]. The average measured zeta potentials of the E3 and wild-type phage in dilute TBS were -33.9 ± 1.6 mV and -29.9 ± 2.2 mV, respectively.

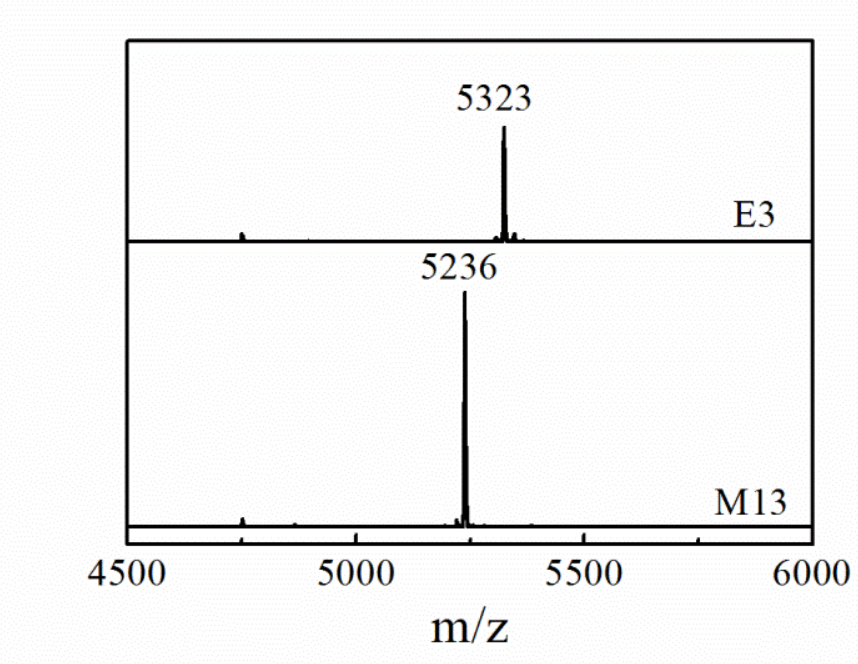

Figure 19. MALDI-TOF MS spectra of E3 and wild-type M13 phage pVIII coat proteins. The 87 Da difference between the molecular weights of the E3 and wild-type M13 major coat proteins confirmed the genetic modification of the E3 phage. (Data courtesy of Chung Hee Moon)

3.3.2 Macroscopic Fiber Formation

Copper sulfide crystal growth induced by the E3 viral template resulted from successive incubation with $CuCl_2$ and Na_2S precursor solutions. Immediately after mixing the E3 phage with $CuCl_2$, the solution became slightly opaque and white fiber-like agglomerates were observed in suspension, as shown in figure 20 (a). The agglomerates slowly grew in size throughout the 2 h $CuCl_2$ incubation and were easily pelleted with centrifugation. Upon addition of Na_2S to the phage pellet, the solution became light brown in color, the pellet re-dispersed, and dark brown filaments were visible following sonication. figure 20 (c) shows the large fiber-like bundles seen after

Na_2S incubation. The bundle formation observed throughout $CuCl_2$ incubation is consistent with previous reports of anionic filamentous or rod-like viruses in solutions containing divalent cations such as Ca^{2+}, Mg^{2+}, Zn^{2+}, or Cu^{2+} [77, 84, 85, 89]. In these reports, metal ions complexed with the viral surface via non-specific electrostatic interaction. The adsorbed cations screened the negative charge of the virus, reducing the electrostatic repulsion between viruses and causing lateral aggregation. These solutions were reported to appear 'cloudy' or 'opalescent' [77, 84]. Furthermore, similar to our observations following Na_2S incubation, other studies have reported aggregated phage bundles remaining intact throughout subsequent crystallization steps [84, 85].

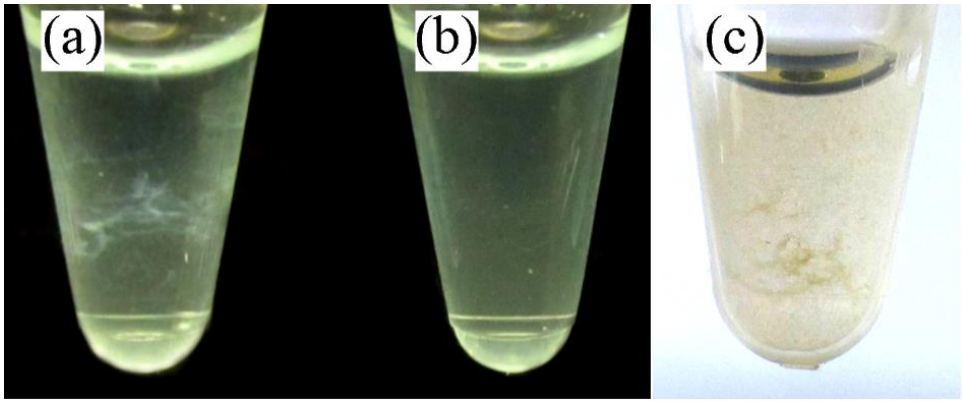

Figure 20. Optical images of (a) the E3 viral template and (b) the wild-type M13 phage following incubation in 100 mM $CuCl_2$. Large fiber-like agglomerates were visible within the solution containing the E3 template, but not the wild-type M13 phage. (c) E3 phage fibers coated with nanocrystalline copper sulfide were observed in suspension following incubation in Na_2S.

The electrostatic interactions associated with this specific colloidal system were further examined with zeta potential measurements, optical images, and TEM. The zeta potential of the E3 phage was increased from -33.9 ± 1.6 mV in dilute TBS to -11.6 ± 1:3 mV in dilute TBS with 0.5 mM $CuCl_2$. Moreover, the zeta potential increased as the

$CuCl_2$ concentration increased, indicating that the copper cations screened the negative charge of the E3 phage as indicated in figure 21.

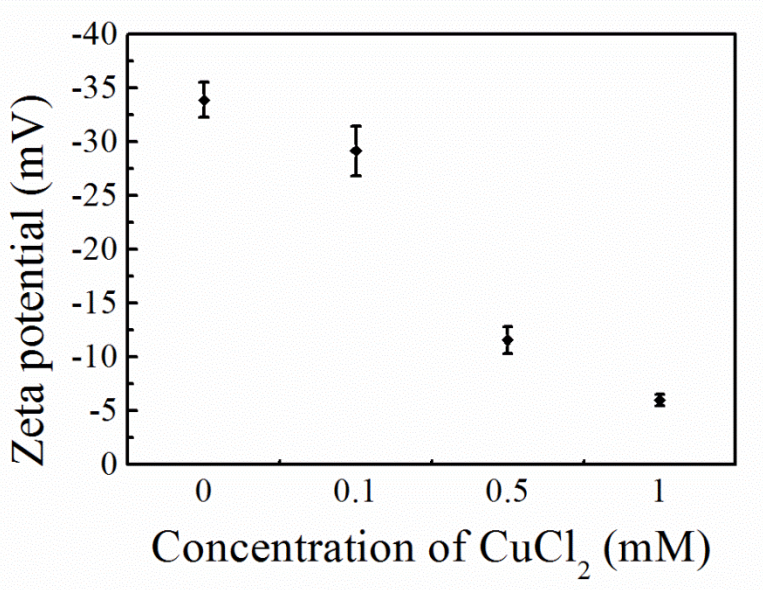

Figure 21. Zeta potential of E3 phage as a function of $CuCl_2$ concentration. A decrease in zeta potential was observed with increasing $CuCl_2$ concentration due to increased electrostatic screening. Some precipitation of phage agglomerates was observed in1 mM $CuCl_2$ such that fewer than 30 measurements were averaged.

At higher $CuCl_2$ concentrations, the repulsive forces between E3 phage templates were sufficiently reduced by the electrostatic screening of copper ions to allow the formation of large agglomerates such as those observed optically (100 mM $CuCl_2$) and with TEM (1 mM $CuCl_2$) in figures 20 (a) and 22 (a), respectively. In contrast, the wild-type M13 phage, with a lower charge density, produced fewer and smaller agglomerates than the E3 phage as shown optically (100 mM $CuCl_2$) and with TEM (1 mM $CuCl_2$) in figures 20 (b) and 22 (b), respectively. A similar dependence of aggregation on charge density was observed for the more negatively charged fd virus compared to the M13

when suspended in a divalent metal ion solution [84, 89]. No fiber-like structures were observed in samples made without phage templates indicating that the viral template was integral to macroscopic fiber formation.

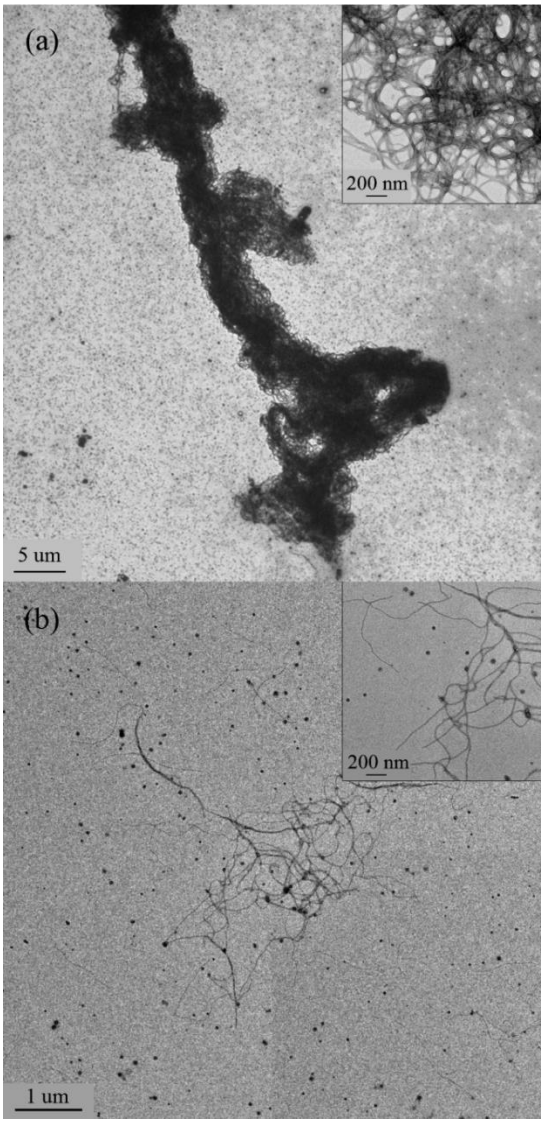

Figure 22. The effect of the viral template surface charge density on agglomerate structure and agglomerate size in 1 mM $CuCl_2$. (a) E3 phage templates produced large, dense agglomerates. Inset: higher magnification image showing that the agglomerates were composed of very closely-packed phage bundles. (b) Wild-type M13 phage resulted in small, loose agglomerates. Inset: higher magnification image showing that the agglomerates were composed of fewer, loosely-packed phage.

3.3.3 TEM, EDX and electron diffraction studies

Figures 23 (a)–(d) show TEM images of typical aggregates and individual phage found within the copper sulfide and phage suspension. Large agglomerates of phage bundles, smaller clusters of phage, and individual phage were all observed. The phage and the copper sulfide nanocrystal agglomerates ranged from a few microns to tens of microns in size and were each made up of phage bundles approximately 13–67 nm in width. Individual phage coated with copper sulfide nanoparticles appeared as high-aspect-ratio nanostructures with an average length of 946±31 nm and an average width of 11±2.6 nm. Regardless of the configuration of the phage templates (bundled or individual), nanocrystalline material was found along the length. The density of the nanocrystalline material on the template varied greatly. Some templates were found to have closely-packed, continuous coverage while others displayed sparse coverage with only a few nanoparticles. Furthermore, the nanocrystalline material typically appeared thicker on the exterior of phage bundles and on individual phage templates than on phage located within a bundle. This could be due to reduced diffusion rates of one or both of the precursors within the well-aligned bundles, despite the use of sonication during the synthesis. Alternatively, it could be caused by differences in electrostatic screening. Further studies are necessary to fully understand the observed difference in nanocrystalline material thickness. The sequential incubation in precursor solutions was critical to template crystallization. E3 phage templates did not display a strong affinity for pre-formed copper sulfide nanoparticles. Furthermore, synthesis in which the wild-type

M13 phage was used as a template produced very little to no copper sulfide along the phage surface, as shown in figure 24.

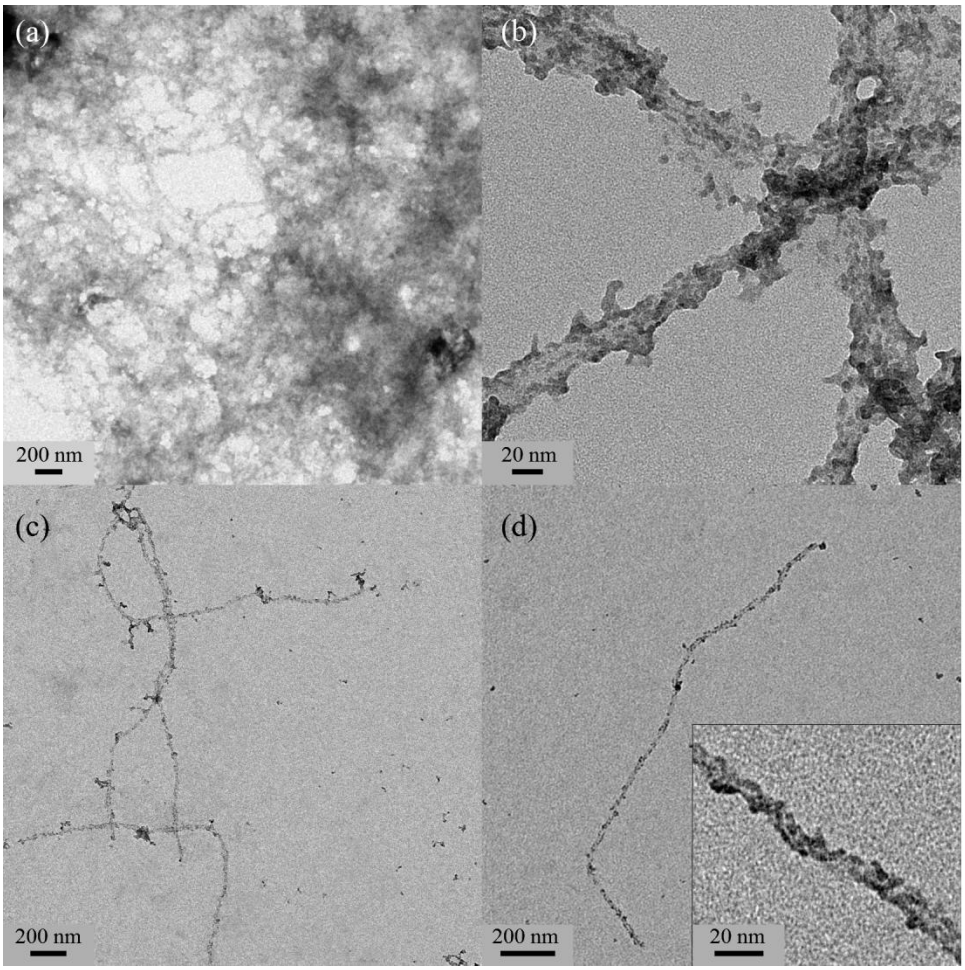

Figure 23. TEM images of (a) large phage bundles coated with copper sulfide, (b) higher magnification image showing phage bundles formed from several individual phage, (c) copper sulfide nanocrystals coating a small cluster of a few phage and (d) a single phage coated with copper sulfide nanocrystals. Inset: high magnification image of copper sulfide nanocrystals on a single phage.

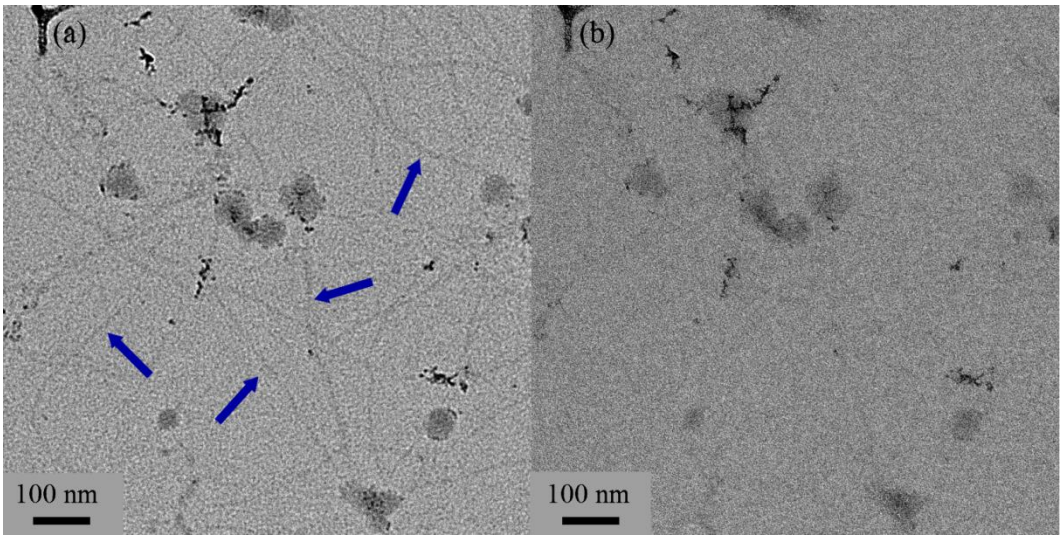

Figure 24. TEM image of synthesis products templated by wild-type M13 phage. (a) Slightly defocused image showing small bundles and individual wild-type M13 phage (indicated by blue arrows). (b) Focused image showing low coverage and yield of synthesized material on the template.

The crystalline structure and composition of the copper sulfide nanocrystalline material were studied further using EDX and electron diffraction. As shown in figure 25, the EDX spectrum of the crystalline nanoparticles confirmed that they contained predominantly Cu and S. The additional peaks observed in the spectrum are identified as C Kα , O Kα , and Ni Kα lines, which are generated by spurious scattering from the TEM Ni grid and the amorphous carbon support film, as well as the phage. The O Kα peak was an indication of possible partial oxidation of copper sulfide. A selected area electron diffraction pattern from the agglomerated copper sulfide and phage bundles is shown in the inset of figure 26. The observed ring pattern can be indexed with the digenite structure, a slightly copper-deficient cubic polymorph of copper sulfide with the anti-fluorite structure and $Cu_{1.8}S$ stoichiometry [90]. The measured d-spacings, 3.2, 1.95

and 1.67 Å, were indexed as the (111), (220) and (311) interplanar distances of digenite. High resolution TEM (HRTEM) images of the dense aggregates of copper sulfide and phage are also shown in figure 26. The material was composed of small, tightly-packed, polydisperse nanocrystals ranging in size from 2 to 7 nm. Smaller nanocrystals were nearly spherical, whereas larger nanocrystals appeared slightly elongated. Figure 26 shows the 3.2 Å lattice fringes of the individual nanocrystals which are consistent with the digenite (111) interplanar distances.

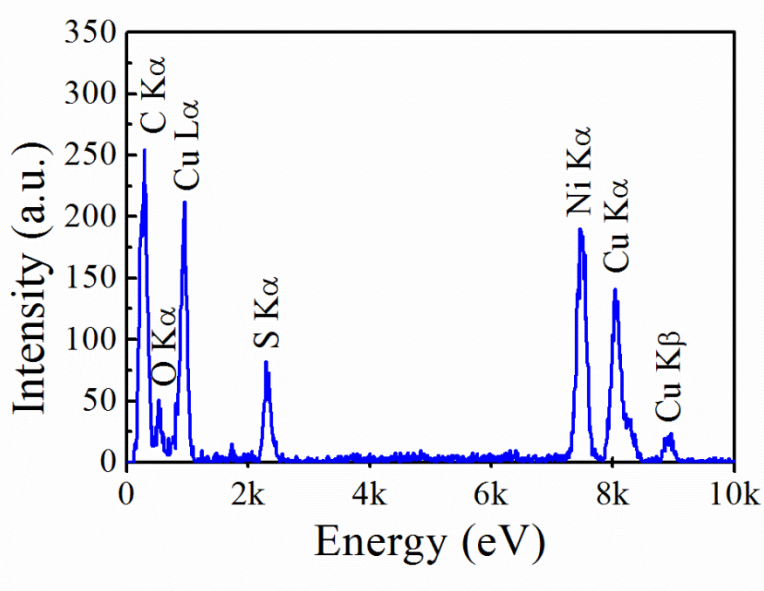

Figure 25. EDX spectrum for the copper sulfide nanocrystalline material showing elemental copper and sulfur peaks.

Nanoparticle size is difficult to predict and can typically be attributed to a combination of crystal growth conditions. Nonetheless, it is interesting to note that the nanocrystals formed by the carboxyl-rich E3 template were smaller and more polydisperse than those templated by bionanotubes functionalized with the imidazole-rich 12-mer peptide, HG12 [74]. The comparatively diminished binding site spacing of the E3

may not allow for the formation of larger diameter nanoparticles such as those observed by Banerjee et al [74]. Further studies are necessary to determine the effect of peptide spacing on crystal growth.

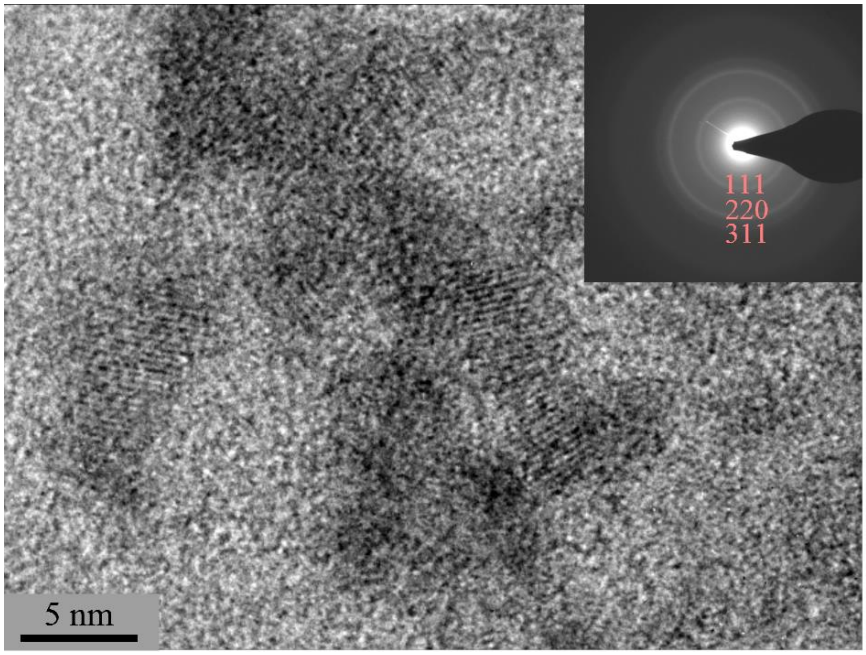

Figure 26. HRTEM image of nanocrystalline material showing the (111) lattice fringes of cubic $Cu_{1.8}S$ with digenite structure. Inset: indexed selected area electron diffraction pattern of the crystalline copper sulfide material. (Images courtesy of Krassimir Bozhilov)

3.3.4 Optical properties

The absorption spectrum of a film prepared from the synthesized material is shown in figure 27 from 360 to 3300 nm. In the ultraviolet to visible wavelength region, a strong increase in absorbance was observed as the wavelength decreased below 800 nm. This optical behavior was attributed to indirect and direct band-to-band transitions of the semiconductor material. Bandgaps near 1.55–1.6 eV have been reported for bulk and polycrystalline digenite [45, 47]. In the near infrared (NIR) wavelength region,

a broad peak near 1060 nm and a narrower set of peaks near 3000 nm were observed. These features were attributed to localized surface plasmon resonance (LSPR) due to the presence of free carriers within $Cu_{1.8}S$. NIR LSPR is common in non-stoichiometric copper sulfides in which copper vacancies produce near metallic concentrations of free carriers, specifically holes [47, 91-94]. The free carrier absorption peak is dependent on the copper sulfide composition, as well as nanocrystal size and shape. The LSPR increases in strength and blue shifts with increasing hole concentration or copper vacancies. Additionally, as observed by Luther et al [92] and Kriegel et al [94] for copper sulfide nanoparticles with dimensions smaller than the mean free path, the LSPR wavelength increases with decreasing particle size due to surface scattering of free carriers. Our NIR absorbance peak near 1060 nm was broad likely due to the polydispersity, 2–7 nm diameter particles, of the nanocrystalline material. The additional peaks near 3000 nm are most likely caused by asymmetric or elongated nanocrystal geometries within the synthesis products or by plasmonic coupling between tightly-packed nanocrystals along the length of the viral template. The presence of multiple resonance peaks due to shape anisotropy was also observed by Hsu et al in Cu_xS nanodisks [95]. The small dip near 2250 nm is due to a spectrophotometer discontinuity.

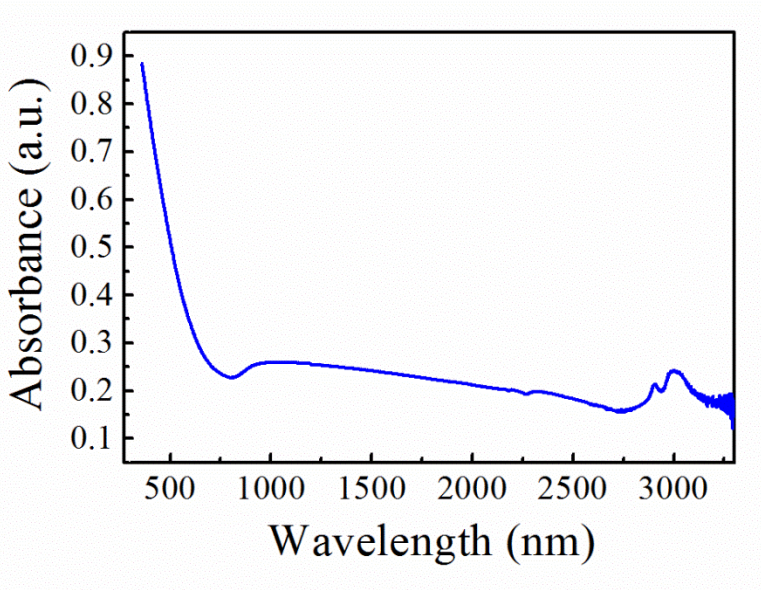

Figure 27. The absorbance spectrum of a film of bio-induced synthesis products on a glass slide.

3.4 Conclusion

We have examined the use of a high-aspect-ratio viral scaffold for bio-induced copper sulfide crystal growth. The dense, well-organized binding sites of the highly negatively charged, genetically-modified M13 template produced cubic $Cu_{1.8}S$. Both interband and free carrier absorption were exhibited by the polydisperse, nanocrystalline copper sulfide material. Due to the complexity of the Cu–S system phase diagram with a multitude of polymorphic phases and non-stoichiometric compounds, copper sulfide is a compelling system in which to study bio-assisted crystal growth. In many living organisms, biomolecules have demonstrated control of both stoichiometry and crystal structure of inorganic materials. These bio-induced synthesis studies are an initial excursion into the capacity of highly-organized, hierarchical viral templates to control

semiconductor materials with complex phase diagrams such as copper sulfide. The ability to engineer biomolecules to synthesize specific copper sulfide phases would represent significant progress in designing materials with potentially high impact on future photovoltaic and plasmonic devices.

4 Stability Study of Viral-templated Copper Sulfide Material

4.1 Introduction

The Cu-deficient phases of copper sulfide self-dope introducing large hole concentrations with increased Cu vacancies. These nearly metallic free carrier concentrations produce near infrared plasmon resonance absorption and significantly increase semiconductor conductivity. Materials, such as these, which exhibit optical and electrical behaviors which are a hybrid of those conventionally associated with semiconductors and metals are useful for studying phenomena such as exciton-plasmon coupling [96], plasmon-based electron transfer [97], and near field enhancement [97]. Moreover, they have direct use in biomedical imaging [98], photothermal therapy [99-101], sensing [102, 103], and photocatalysis [104, 105]. A significant limitation of nanoscale copper chalcogenides for many of these applications is that they have been found to interact readily with oxygen, often producing clear changes in composition and/or free carrier concentration [94, 106, 107]. Recent stability studies have primarily focused on the transformation of stoichiometric chalcocite to non-stoichiometric djurleite ($Cu_{1.97}S$) both in nanoparticles and thin films [91, 94, 107, 108]. The rate and extent of conversion when exposed to ambient conditions, as might be expected, was found to be highly dependent on ligand [82, 109] and surface passivation [107, 109, 110] selection.

In this chapter the optical and electrical stability of the bio-templated copper sulfide material has been described. Although Cu_xS synthesis has been achieved using a number of biomolecules from simple amino acids [80, 81] to hierarchical peptide-based

bionanotubes [74], the optical and electrical stability of these materials is rarely evaluated. Here, we examine the optical and electrical properties of the non-stoichiometric viral-templated $Cu_{1.8}S$ films to better assess their potential utility in future device applications. Despite the presence of the viral template, material instabilities associated with atmospheric conditions were revealed through optical absorption and electrical resistance measurements, and confirmed with surface analysis.

4.2 Experimental Details

4.2.1 $Cu_{1.8}S$ Synthesis and Film Formation

Nanocrystalline, viral-templated $Cu_{1.8}S$ was synthesized following procedure described previously in Section 3.2.3. Briefly, an M13 bacteriophage which displayed a peptide composed of three glutamic acid residues (E3) on each of the 2700 copies of the pVIII protein found along its length served as the viral template [33, 62, 87, 88]. The addition of acidic amino acids to the M13 major coat protein increased the net negative charge of the template enhancing non-specific electrostatic interactions with copper cations and resulting in synthesis of templated $Cu_{1.8}S$ [111]. To form the nanocrystalline semiconductor materials, the M13 templates were sequentially incubated in copper chloride ($CuCl_2$) and sodium sulfide (Na_2S) precursors. Stock solutions of 1 M $CuCl_2$ (Acros Organics) and 1 M Na_2S (MP Biomedicals) were prepared in deionized water and diluted to 200 mM and 1mM, respectively. Equal parts of 10^9 pfu/μL E3 phage and 200 mM $CuCl_2$ were combined to a final volume of 200 μL. The solution was vortexed to ensure mixing and incubated for 2 hours undisturbed. The phage templates were

subsequently pelleted by centrifugation. The excess $CuCl_2$ precursor was removed leaving the pellet intact, 100 μL of 1 mM Na_2S was added, and the solution was incubated for 5 min with sonication.

To prepare films for characterization, the viral-templated $Cu_{1.8}S$ synthesis products were loosely pelleted with low speed centrifugation and the Na_2S precursor was removed. The pellet was rinsed with deionized water to remove untemplated material and residual precursor, and resuspended in a minimal volume of deionized water. The products were drop cast onto a suitable substrate and dried under house vacuum for approximately 20 minutes. Glass slide substrates were used for optical absorption measurements; Si/SiO_2 substrates pre-patterned with e-beam deposited electrodes were used for electrical measurements; and gold-coated silicon substrates were used for x-ray photoelectron spectroscopy (XPS) analysis.

4.2.2 Optical stability study of films

The room-temperature optical absorption of viral-templated $Cu_{1.8}S$ films was measured from 360 nm to 3300 nm using a spectrophotometer (Cary 500 UV/Vis/NIR) neglecting reflection and scattering effects. The optical absorption of the films was measured at regular intervals after exposure to ambient conditions for several days.

4.2.3 Viral-templated $Cu_{1.8}S$ film characterization

The $Cu_{1.8}S$ film morphology and thickness were studied with scanning electron microscopy (SEM, XL30 FEG). Median film thickness and thickness range were determined by measuring cross-sectional thickness in 50 to 90 locations for each of three

samples. Samples were sputtered coated for 20 s with Pt/Pd prior to SEM analysis to minimize charging effects.

4.2.4 Electrical characterization and stability study

Electrical characterization was completed using synthesis products drop cast onto Si/SiO_2 substrates pre-patterned with Ti/Au (10 nm/100 nm) electrodes which were 3 mm by 2 mm and separated by a 50 μm gap. In addition, control samples were prepared with E3 phage alone and copper sulfide synthesized without a phage template under the same conditions. The resistance of the as-synthesized materials and control samples was measured under room temperature using two-terminal, current-voltage (I-V) measurements in which the current was recorded as the applied voltage was swept from -0.5 V to 0.5 V (Keithley 2636A sourcemeter). To evaluate the stability and resistance of viral-templated materials resulting from different storage conditions, measurements were performed on the same devices before and after storage under either ambient conditions or in a glove box for 3 days. The glove box atmosphere was inert gas (Ar) with < 0.1 ppm of O_2 and H_2O. All electrical measurements were completed under ambient conditions, therefore a 10-15 min exposure to air was unavoidable for all films during sample transfer and probe placement between initial and final I-V measurements.

4.2.5 X-ray photoelectron spectroscopy characterization

An x-ray photoelectron spectrometer (XPS, Kratos AXIS Ultra Delay-Line Detector Imaging XPS) equipped with an Al Kα monochromated X-ray source and a 165 mm mean radius electron energy hemispherical analyzer was used to determine the

composition and oxidation state of the as-synthesized material surface. During sample transfer and loading, as-synthesized materials were exposed to near ambient conditions for approximately 5 minutes. In addition, viral-template materials stored under ambient conditions for 3 days were also analyzed. Survey spectra were taken with an 80 eV pass energy and 1 eV energy step and a 20 eV pass energy and 0.1 eV energy step were used for high-resolution Cu 2p and S 2p spectra. Binding energy calibration was based on the C 1s peak at 285.0 eV.

4.3 Results and Discussion

4.3.1 Viral-templated $Cu_{1.8}S$ Film Characteristics

Film morphology and thickness was characterized on Si/SiO_2 substrates with pre-patterned gold electrodes. The extremely smooth Si/SiO_2 substrate surface allowed easy identification of the film and aided in accurately evaluating film thickness, while the large gold electrodes minimized charging effects from the electron beam. The drop-cast films of phage templated $Cu_{1.8}S$ were 1.5 to 3 mm in diameter and are shown spanning the 50 μm gap between the electrodes in figure 28 (a). SEM images of the $Cu_{1.8}S$ film morphology are shown in figures 28 (b, c).

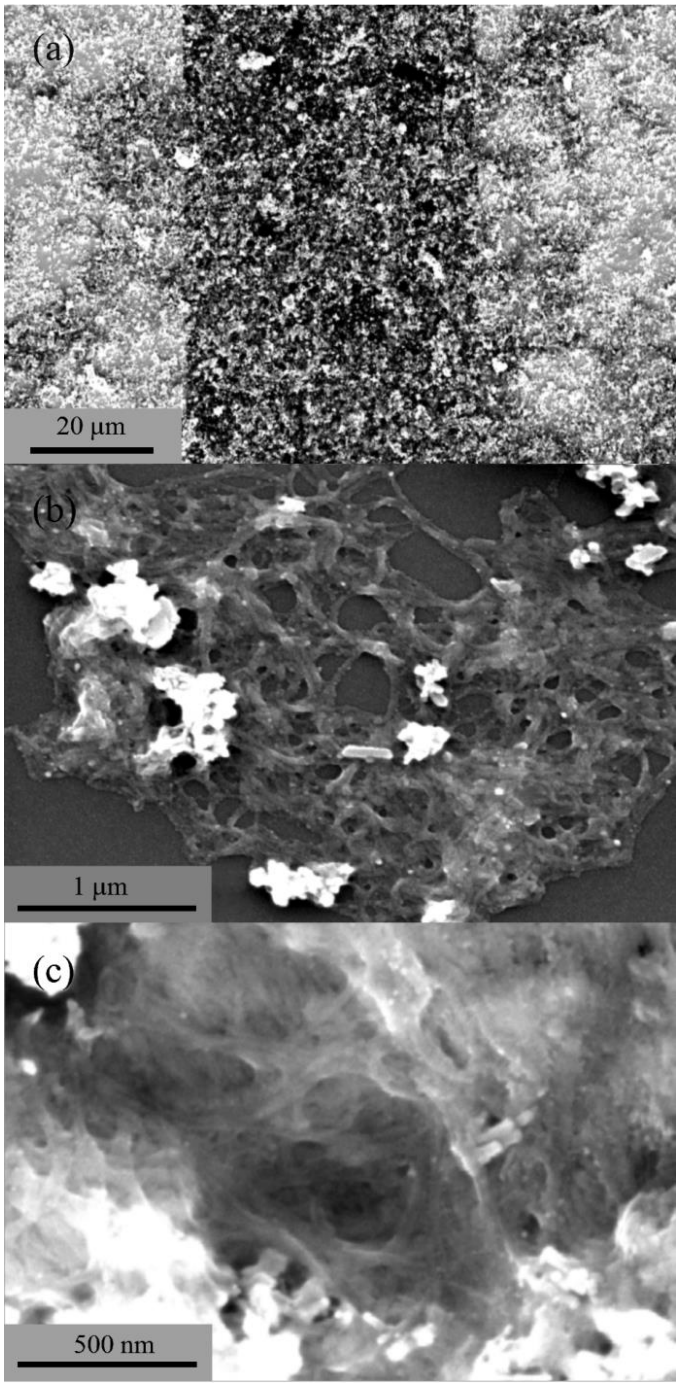

Figure 28. SEM images of $Cu_{1.8}S$ film. (a) Image of film with Au electrodes on both sides. (b) Image of $Cu_{1.8}S$ film where the density of phage agglomerates is less and the porous nature of the film is seen. (c) Higher magnification image of $Cu_{1.8}S$ film showing randomly aligned phage coated with synthesized material.

The film was composed of several large agglomerates of phage bundles coated with inorganic nanoscale material. The concentration of agglomerates varied across the film such that in some locations the film thickness was reduced to thin phage bundles 50 to 100 nm in diameter, as observed in figure 28 (b). Inspection at higher magnifications such as that in figure 28 (c), revealed that randomly aligned, individual $Cu_{1.8}S$-coated phage were visible throughout the films, including within the more densely packed agglomerates. This morphology was consistent with the macroscale electrostatically assembled agglomerates observed in solution during the synthesis process [111]. A representative SEM cross-section of a drop cast film is shown in figure 29, along with a histogram of film thickness. The thickness of this film ranged from 126 nm to 5.8 μm, with a median of 939 nm. Similar medians and thickness ranges were observed in other drop cast samples.

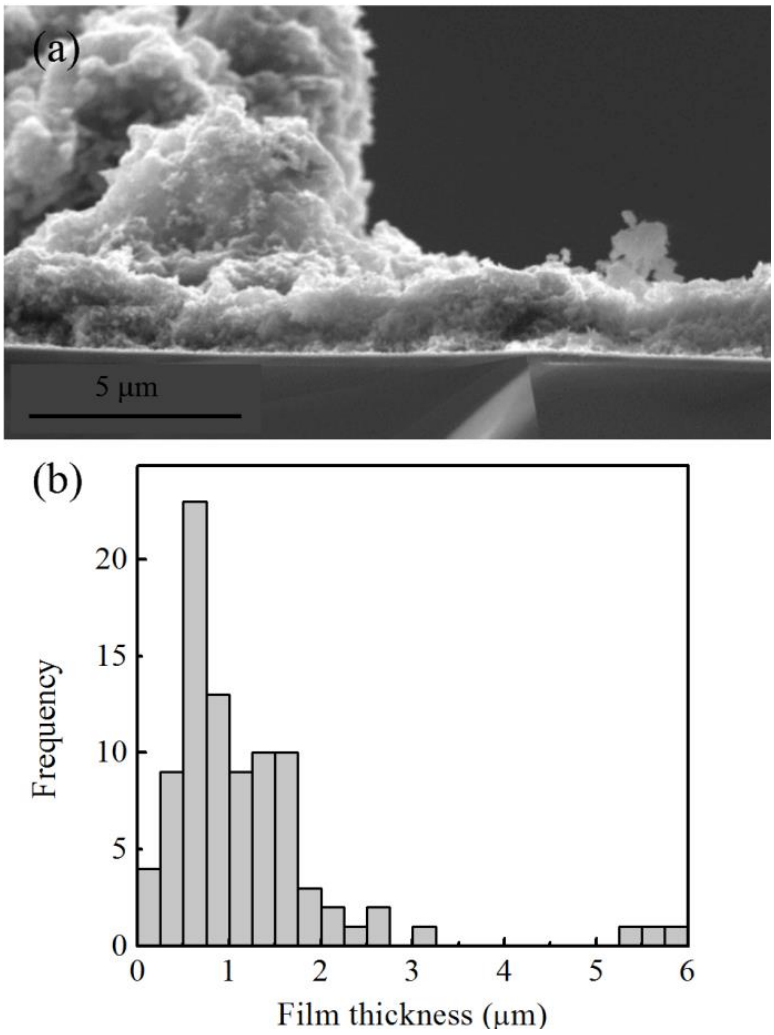

Figure 29. (a) SEM image of a $Cu_{1.8}S$ film cross-section showing thickness. (b) Histogram of film thickness across sample.

4.3.2 Optical stability study of the synthesized material

Optical absorption of the viral-templated $Cu_{1.8}S$ material was measured on glass substrates under ambient conditions. As shown in the inset of figure 30 and observed previously for these viral-templated materials [111], short wavelength absorption corresponding to $Cu_{1.8}S$ interband transitions, as well as a few additional long wavelength

absorbance peaks near 1060 nm, 2900 nm, and 3000 nm were observed. The near infrared (NIR) absorbance peaks were attributed to localized surface plasmon resonance (LSPR) due to the large concentration of free carriers, specifically holes, within the non-stoichiometric $Cu_{1.8}S$. The strength of the free carrier absorption peak is dependent on carrier concentration, increasing with hole concentration or copper vacancies [91, 92, 94]; therefore, it was not surprising that a strong LSPR peak was observed within these highly copper-deficient materials.

To assess material stability under ambient conditions, the absorbance spectrum of the synthesized materials was measured at regular intervals. The short wavelength absorption below 800 nm remained unchanged throughout the 3 day experiment, however the NIR absorption was seen to change rapidly. LSPR spectra taken from 800 to 3300 nm after 2 min, 3 h, 6 h, 12 h, 24 h, and 3 days of exposure are shown in figure 30. The NIR absorbance clearly increased continuously throughout the 3 day experiment indicating that the concentration of free carriers was also increasing. Similar optical behavior has been described in colloidal Cu_2S nanocrystals exposed to air [94], as well as other copper chalcogenide colloidal nanocrystals [94, 106]. In these reports, nanocrystal oxidation caused by exposure to air transformed stoichiometric to non-stoichiometric phases, increasing hole concentrations within hours.

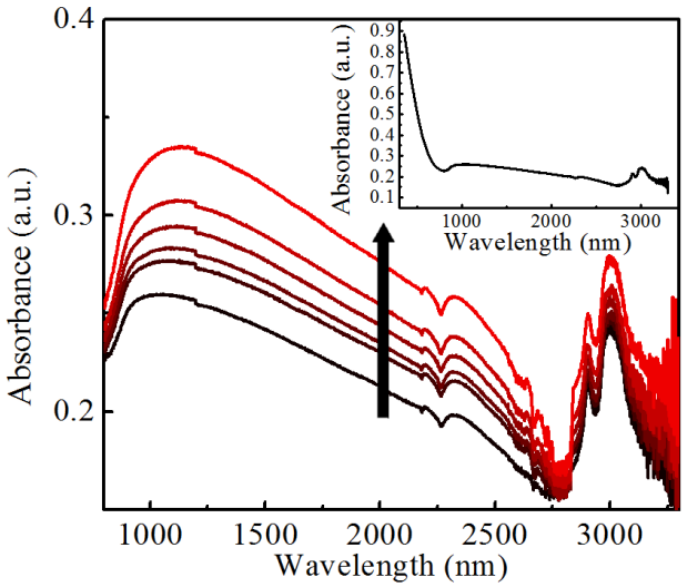

Figure 30. Optical response of $Cu_{1.8}S$ over time. NIR absorption spectra taken after 2 min, 3 hr, 6 hr, 12 hr, 24 hr and 3 days of exposure to ambient conditions. Exposure time increases from black to red curve as indicated by the black arrow. Inset: Absorption spectrum of $Cu_{1.8}S$ film from 300 to 3300 nm showing the interband transitions and NIR absorption.

For further analysis, the square of the magnitude of the broad 1060 nm LSPR absorbance peak, which is proportional to the hole carrier concentration as is discussed below. The absorbance A is given by the Beer-Lambert Law

$$A = \alpha l \tag{1}$$

where α is the absorption coefficient and l is the path length of the light. The absorption coefficient can also be represented in terms of the extinction coefficient $\kappa_{ext}(\lambda)$ such that

$$\alpha = \frac{4\pi f}{c}\kappa_{ext}(\lambda) \tag{2}$$

where f is the frequency of the electromagnetic wave, λ is the wavelength, and c is the velocity of light in vacuum. Using Mie scattering theory, and the discussion outlined by Zhao et al. [91]. The extinction coefficient can be related to the square root of the free carrier concentration. The extinction coefficient is given by the following expression [112, 113]

$$\kappa_{ext}(\lambda) = 18\pi NV\varepsilon_m^{3/2}\frac{\varepsilon_2(\omega)}{\lambda[(2\varepsilon_m+\varepsilon_1(\omega))^2+\varepsilon_2(\omega)^2]} \tag{3}$$

where N is the number of particles in volume V, $\varepsilon_1(\omega)$ and $\varepsilon_2(\omega)$ are the real and imaginary parts of the dielectric constant, respectively, and ε_m is the dielectric constant of the surrounding medium. Using Drude theory, $\varepsilon_1(\omega)$ and $\varepsilon_2(\omega)$ are defined as

$$\varepsilon_1(\omega_p) = \varepsilon_{core} - \frac{4\pi ne^2\tau^2}{m^*(1+\omega_p^2\tau^2)} \tag{4}$$

$$\varepsilon_2(\omega_p) = \frac{4\pi ne^2\tau}{\omega_p m^*(1+\omega_p^2\tau^2)} \tag{5}$$

where ω_p is the plasma frequency, e is the charge on a free carrier, n is the free carrier or hole concentration, ε_{core} is the material dielectric constant, m^* is the hole effective mass, and τ is the mean free time between collisions. If $\varepsilon_2(\omega)$ is small or weakly dependent on ω, then the plasmon resonance condition is [114]

$$\varepsilon_1(\omega) = -2\varepsilon_m \tag{6}$$

And the plasma frequency ω_p is given by

$$\omega_p^2 = \frac{4\pi ne^2}{m^*(2\varepsilon_m+\varepsilon_{core})} - \frac{1}{\tau^2} \approx \frac{4\pi ne^2}{m^*(2\varepsilon_m+\varepsilon_{core})} \tag{7}$$

At plasmon resonance, the extinction coefficient can be simplified using Eqs. 4, 5, and A7 and $\omega_p^2\tau^2 \gg 1$ for optical to NIR frequencies such that

$$\kappa_{ext}(\lambda) = \frac{18\pi NV\varepsilon_m^{3/2}m^*\omega_p^3\tau}{\lambda.4\pi ne^2} = \frac{18\pi NV\varepsilon_m^{3/2}\tau}{\lambda}\frac{(4\pi ne^2)^{1/2}}{m^{*1/2}(2\varepsilon_m+\varepsilon_{core})^{3/2}} \quad (8)$$

From Eq. 8, the extinction coefficient $\kappa_{ext}(\lambda)$ is proportional to the carrier concentration $n^{1/2}$ assuming all other parameters constant for the material. Using Eqs. 1, 2, and 8, the absorbance A is also proportional to the carrier concentration $n^{1/2}$; therefore a plot of A^2 as a function of time can be used to elucidate time dependent change in the hole concentration within the $Cu_{1.8}S$ viral-templated materials.

The square of the absorbance was plotted as a function of exposure time, and is shown in figure 31 (a). The square of this free carrier absorbance peak increased by 66% over the 3 day experiment, growing most quickly within the first 3 hours and slowing in subsequent hours A power law fit was found to accurately describe the relationship between the square of the magnitude of the absorbance peak, and thus the carrier concentration, and time. This is consistent with observations of the time evolution of hole concentrations within Cu_2S atomic layer deposition (ALD) films exposed to air [107], however the hole concentrations in viral-templated $Cu_{1.8}S$ more nearly followed $t^{1/2}$ whereas ALD films followed $t^{1/4}$ to $t^{1/3}$. A similar time dependence has been reported for oxide film growth on metals (i.e. Cu) [115], suggesting that the additional free carriers were the result of diffusion-limited oxide or film formation on the phage-templated material surface. The LSPR absorbance peaks near 2900 nm and 3000 nm displayed a similar power law dependence. Absorbance squared values as a function of exposure

time for each of these resonance peaks are shown in figures. 31 (b, c). This power law relationship also accurately described samples stored under ambient conditions for extended time periods such that no significant increase in the LSPR absorbance was observed after 10 days.

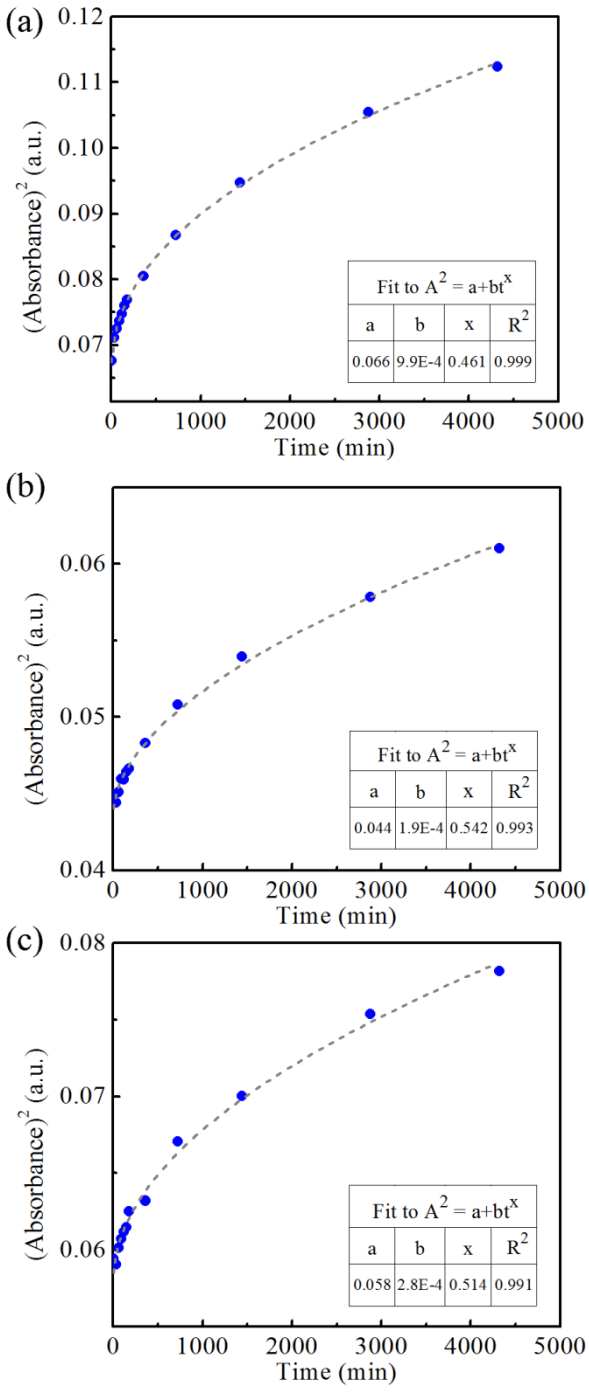

Figure 31. The square of the LSPR absorbance peak intensity for peaks near (a) 1060 nm, (b) 2900 nm, and (c) 3000 nm. The blue circles show the experimental absorbance squared (A^2) values and the grey dashed line is the best fit to a power law relationship between absorbance squared (A^2) and exposure time (t). The table lists the fit parameters and the R^2 values.

4.3.3 Electrical behavior and stability

I-V measurements of viral-templated materials were performed on Si/SiO_2 substrates. The drop cast films were 1.5 to 3 mm in diameter and readily bridged the 50 μm gap between the electrodes. When bias was applied to the films, they were found to be electrically conductive and Ohmic in nature. Recorded resistances ranged from 10^3 to 10^{10} Ω for as-synthesized materials, likely due to variations in film thickness and semiconductor coverage along the template. Films with 10^3 to 10^5 Ω resistance were selected for further investigation. In these films, applied voltages from -3 V to +3 V also resulted in Ohmic behavior and applied voltages as high as 20 V did not result in breakdown. Control samples prepared with phage alone and copper sulfide synthesized without a phage template under the same conditions did not have detectable current flow. The electrical conductivity of biological materials such as the M13 phage is generally low. Moreover, using the same synthesis conditions without a phage template resulted in a low density of copper sulfide nanoparticles, such that a continuous path for current flow was not formed within the drop cast material.

To further study the effect of ambient conditions on the viral-templated films and investigate the potential contribution from surface oxidation, film resistances were measured as-synthesized and then again following 3 days of exposure to either atmospheric or low oxygen, low humidity conditions (< 0.1 ppm of O_2 and H_2O) in a glove box. Due to measurement constraints, all films were exposed to air for approximately 10 - 15 min during sample transfer and measurement. Figure 32 (a) depicts the initial and final I-V behavior of two representative nanocrystalline $Cu_{1.8}S$

films in which the voltage was swept from -0.5 V to 0.5 V. Although material conductivity values could not be determined due to film thickness variations, changes in resistance associated with specific storage conditions were readily evaluated. In figure 32 (b), the ratio of as-synthesized, initial resistance ($R_{initial}$) to the 3 day, final resistance (R_{final}) has been calculated for a number of films held under ambient conditions and within an Ar-filled glove box. The resistance of the films stored in air significantly decreased resulting in an average $R_{initial}/R_{final}$ ratio of 39.

A decrease in resistance is consistent with increased material conductivity associated with the increased free carrier hole concentration observed with time dependent LSPR absorbance measurements. However, it is interesting to note that although LSPR absorbance indicated only a 66% increase in hole concentration after 3 days, the resistance dropped by nearly a factor of 40, thus suggesting that other factors may also contribute to the observed resistance decrease. For example, increased Cu-deficiency could speed diffusion of already highly mobile Cu ions which may bridge nanoparticle interfaces significantly reducing resistance. Alternatively, enhanced phage dehydration could cause subtle geometric changes, increasing physical contact between $Cu_{1.8}S$ nanoparticles and substantially decreasing resistance. Nonetheless, the observed resistance decrease correlates well with recent electrical behavior of other copper chalcogenide films in which the presence of air played a critical role [107, 116]. For example, films of Cu_2Se nanoparticles were found to initially display non-linear I-V behavior with a 1 V applied bias, however following 2 hours of exposure to air the same films exhibited Ohmic behavior and, after 2 days of exposure to air, the current had

increased to over 1000 times its initial value [116]. The change in electrical behavior was caused by the presence of CuO and Se on the nanoparticle surface which potentially reduced interparticle potential barriers, as well as the conversion of Cu_2Se to the more superionic conductor $Cu_{1.8}Se$ [116]. In another case, the electrical behavior of Cu_2S ALD films was significantly impacted by exposure to air [94]. In just under 2 days the conductivity increased from approximately 10 S/cm to 200 S/cm. This conductivity increase was attributed to surface copper deficiencies caused by oxidation which extracted Cu ions from underlying layers, increasing overall hole concentration within the films [107].

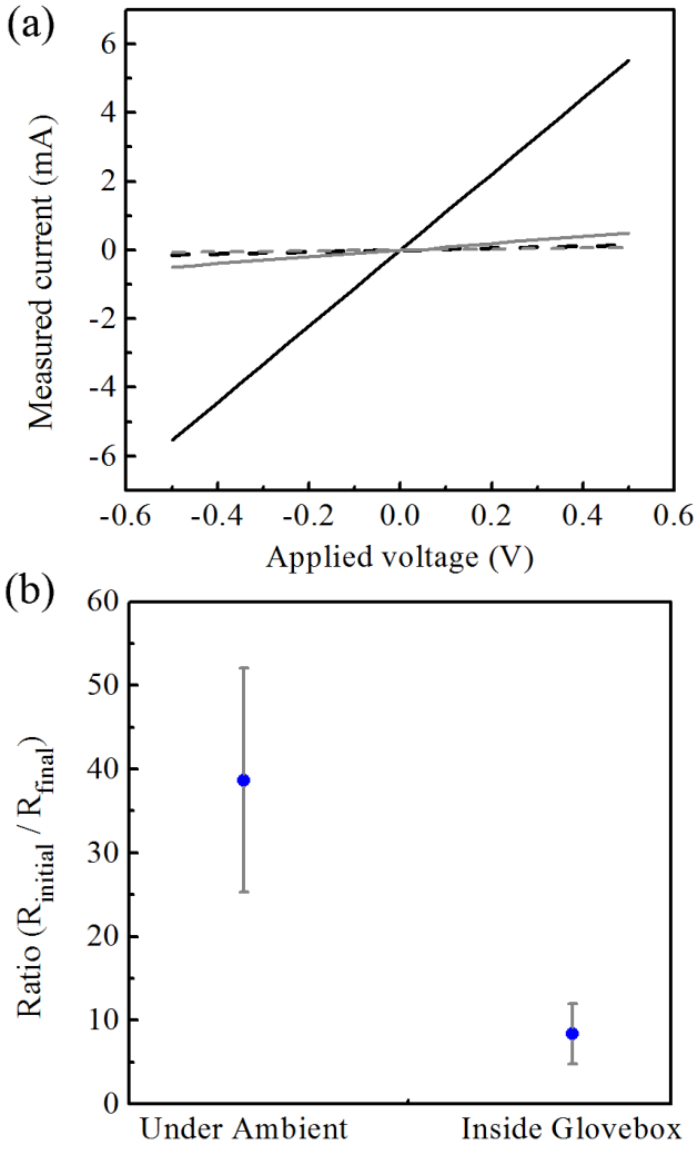

Figure 32. (a) I-V response of $Cu_{1.8}S$ films stored under ambient conditions (black) and inside a glove box (grey). Responses are shown for as-synthesized devices (dashed), as well after 3 days (solid). (b) Ratio of initial to final resistance for samples stored under ambient conditions and inside a glove box, under inert gas.

Although resistance decreased in films stored under both ambient and inert atmosphere conditions, as shown in figure 32 (b), the resistance decrease was notably lower for films stored under inert gas resulting in an average $R_{initial}/R_{final}$ ratio of 8. Minimizing film exposure to O_2 and H_2O limited the resistance change of $Cu_{1.8}S$ viral-templated materials, thus further suggesting a relationship between the presence of oxygen and the evolution of optical and electrical properties. The approximately eight-fold decrease in resistance observed in the film stored in the glove box is likely due to exposure to ambient conditions during sample transfer and measurement. As concluded through optical absorbance measurements, the rate of increase of hole concentration was most rapid upon initial exposure of the film to air therefore even a short 10 - 15 min exposure could have a large effect on resistance.

4.3.4 Surface composition analysis

To directly probe the surface composition of the viral-templated $Cu_{1.8}S$ films and reveal changes related to prolonged exposure to air, XPS was performed on as-synthesized films, in addition to films exposed to ambient conditions for 3 days. The survey spectrum of the as-synthesized film, shown in figure 33, indicated the presence of Cu, S, O, Cl, C, N, and Au. Phage templates within the film introduced C and N, and Au was associated with the substrate. High resolution XPS spectra of the Cu2p region of as-synthesized and air-exposed films are shown in figure 34 (a). The primary $Cu2p_{3/2}$ and $Cu2p_{1/2}$ peaks were located at 932.6 eV and 952.5 eV, respectively [117, 118]. These features were deconvoluted into three components: Cu_xS (932.6 eV), $CuSO_4$ (934.4 eV), and $CuCl_2$ (935.8 eV). The Cu_xS peak represents the combined Cu^{1+} and Cu^{2+} states

within the non-stoichiometric copper chalcogenide film [117, 119-121]. Given the small differences between binding energies of the various copper sulfides and the range of Cu species present, it was difficult to confirm the x value for Cu_xS [119, 122]. However, satellite peaks did firmly support the presence of paramagnetic Cu^{2+} [107, 118, 119, 123, 124]. The $CuSO_4$ peak was attributed to the conversion of various copper sulfide phases on the film surface when reacted with air and is consistent with observations of commercial copper sulfide powder [124] and sulfurized copper films exposed to ambient conditions [119], as well as natural chalcocite subjected to aqueous conditions [125]. The $CuCl_2$ peak [117] was likely due to residual precursor within the thick films composed of macroscopic phage agglomerates. $CuSO_4$ and $CuCl_2$ were only detected with XPS surface analysis. In our previous report [111], electron diffraction and energy dispersive x-ray (EDX) spectroscopy showed no evidence of these or other components within the synthesis products. In films exposed to ambient conditions for 3 days, the $CuSO_4$ contribution and the Cu^{2+} satellite peaks increased with respect to the Cu_xS peak indicating a change in surface composition due to oxygen exposure.

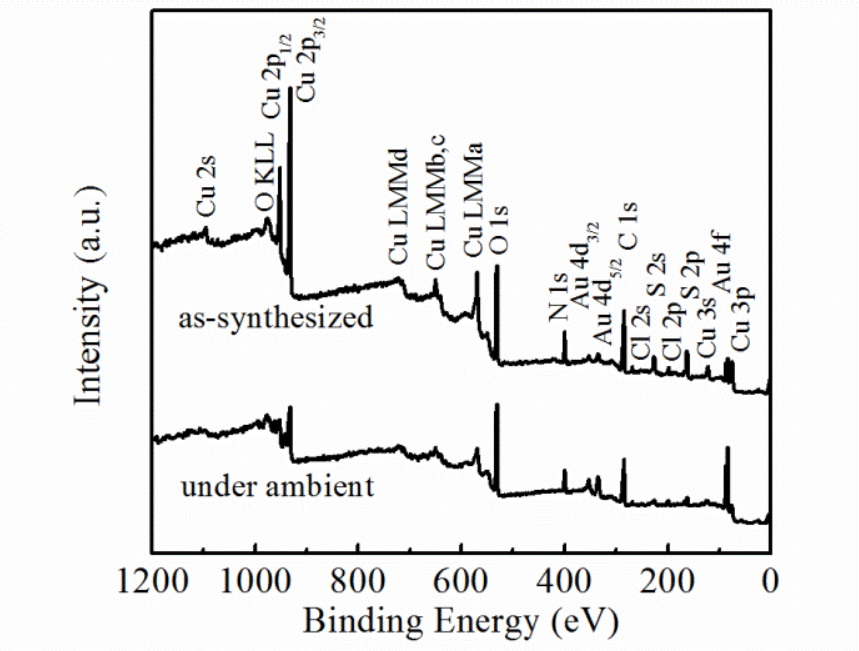

Figure 33. XPS survey scan spectra of an as-synthesized sample and a sample stored under ambient conditions for 3 days.

The S2p region of an as-synthesized film and a film stored under ambient conditions is shown in figure 34 (b). The broad peak was fit with $S2p_{3/2}$ and $S2p_{1/2}$ spin-orbit doublets representing three components. The $S2p_{3/2}$ at 162.4 eV was ascribed to Cu_xS [107, 117, 119] and the higher $S2p_{3/2}$ binding energy peaks at 169 eV and 163.7 eV were correlated to $CuSO_4$ [119, 124] and S_2Cl_2 [126], respectively. Similar to the Cu2p region, the S2p region showed an increased $CuSO_4$ contribution following prolonged exposure to air. The transformation of Cu_xS to $CuSO_4$ upon exposure to air revealed by XPS surface analysis, and the concurrent increase in Cu^{2+} oxidation state contribution as evidenced by the Cu2p satellite peaks, suggested that $CuSO_4$ was formed through removal of copper ions from the nanocrystalline Cu_xS lattice. The resulting copper vacancies increased the overall hole concentration within the semiconductor, and were

likely responsible for the increased carrier concentration observed through absorbance measurements as well as contributing to the decreased film resistance with exposure to air.

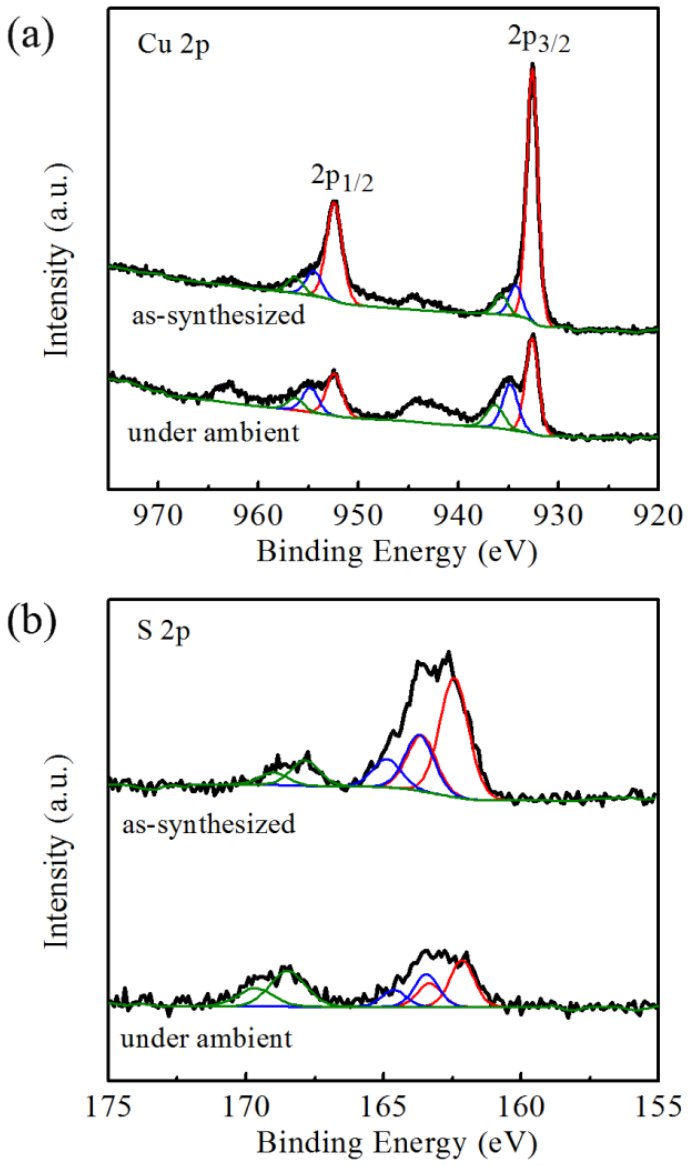

Figure 34. High resolution XPS spectra of the (a) Cu2p and (b) the S2p region for an as-synthesized sample and a sample stored under ambient conditions for 3 days showing the raw data as black solid lines and the deconvoluted spectra as red, blue, and green lines.

4.4 Conclusion

The optical and electrical stability of viral-templated $Cu_{1.8}S$ films were characterized. The properties of drop cast films, which ranged in thickness from 100s to 1000s of nm and were composed of agglomerates of M13 filamentous phage covered with inorganic material, were measured under ambient conditions over a period of 3 days. The magnitude of the LSPR peak grew with exposure time and the resistance of the films decreased, indicating an increase in free carrier concentration. Under inert gas (Ar) with < 0.1 ppm of O_2 and H_2O, the change in film resistance was lessened suggesting a correlation between ambient conditions and carrier concentration. XPS was used to relate changes in surface chemistry to the optical and electrical behavior. The surface analysis revealed the development of a $CuSO_4$ layer on the $Cu_{1.8}S$ surface under ambient conditions which was linked to the observed increase in carrier concentration. These are the first steps towards characterizing the optical and electrical stability of viral-templated non-stoichiometric copper sulfide nanomaterials. Studies which evaluate the physical properties and stability of bio-assembled, copper chalcogenides not only aid the development of in vitro biomolecule control of stoichiometry, phase, and stability, but are critical for assessing the usefulness of these materials for future device applications.

5 NH_3 Gas Sensors Based on Viral-templated $Cu_{1.8}S$

5.1 Introduction

Ammonia (NH_3) is a gas which is naturally present at low levels in the environment primarily due to decomposition of plant and animal matter [127]. These harmless quantities can rise to highly concentrated and dangerous levels at agricultural and industrial sites which use or produce fertilizer, refrigerants, plastics, and explosives, among other products. Exposure to concentrations exceeding 50 ppm, the permissible exposure limit (PEL) recommended by the U. S. Occupational Safety and Health Administration (OSHA), can cause temporary blindness, pulmonary edema, and significant irritation to eyes, skin, and lungs [128]. Furthermore, concentrations above 300 ppm are classified as immediately dangerous to life or death (IDHL) [128]. Sensitive, low power, and inexpensive NH_3 detectors are necessary to maintain safe operation of farming and manufacturing facilities, as well as to monitor gas levels in surrounding locations.

One category of sensor pursued for NH_3 detection is the chemiresistor. Most chemiresistive NH_3 gas sensors use metal oxides for detection. These devices typically operate at elevated temperatures, undesirably increasing power consumption. In recent years, alternative materials which are able to function effectively at ambient temperatures have been pursued [129-131]. NH_3 has been shown to interact reversibly with a range of Cu_xS-based materials including films [103, 132, 133], hollow nanospheres [134], nanoboxes [135], and nanoheterojunction particles [136]; a handful of room temperature

chemiresistive NH_3 gas sensors have been reported [103, 132, 133, 137, 138]. Copper content [103], ion irradiation [137], and surface area [133, 135, 138] have been used to modify sensing behavior. Chemically deposited non-stoichiometric $Cu_{1.4}S$ films exhibited a higher response to NH_3 than stoichiometric CuS or Cu_2S films [103]. Additionally, irradiation with high energy (100 MeV) gold ions further improved the response of these non-stoichiometric films through modification of surface and electrical properties [137]. Finally, enhanced performance was observed for device geometries with increased surface to volume ratios. For example, the NH_3 sensitivity of double-walled $Cu_{1.75}S$ nanoboxes was greater than that of single-walled nanoboxes [135]. We reported the synthesis of non-stoichiometric cubic phase copper sulfide, $Cu_{1.8}S$, using the M13 virus as a biological scaffold [111]. In this work, chemiresistive NH_3 gas sensors were prepared from viral-templated copper sulfide. These composite nanoscale materials enabled sensitive detection of NH_3 at room temperature.

5.2 Experimental Details

5.2.1 Device fabrication

$Cu_{1.8}S$ was prepared following the previously published method in which an M13 virus with three glutamate residues (-EEE-) fused to each major coat protein was used for assembly [111]. An overview of the device assembly procedure using this glutamate-rich, filament-shaped viral template is shown in figure 35, along with an illustration of the final sensor geometry. Briefly, equal parts of 10^9 pfu/μL E3 phage and 200 mM $CuCl_2$ (Acros Organics) were mixed to a final volume of 200 μL and permitted to interact

undisturbed for 2 h. The solution was centrifuged to pellet the phage, the supernatant containing $CuCl_2$ was removed, and 100 µL of 1 mM Na_2S (Sigma Aldrich) was added. The mixture was sonicated for 5 min to re-disperse the pellet and complete $Cu_{1.8}S$ synthesis. The viral-templated materials were drop cast onto Si/SiO_2 substrates pre-patterned with Ti/Au (10 nm/100 nm) electrodes, 50 µm wide and separated by a 3 µm gap. After 5 min incubation, the substrates were rinsed twice with deionized water and dried. The morphology of the $Cu_{1.8}S$/virus composite materials was imaged with scanning electron microscopy (SEM) and transmission electron microscopy (TEM).

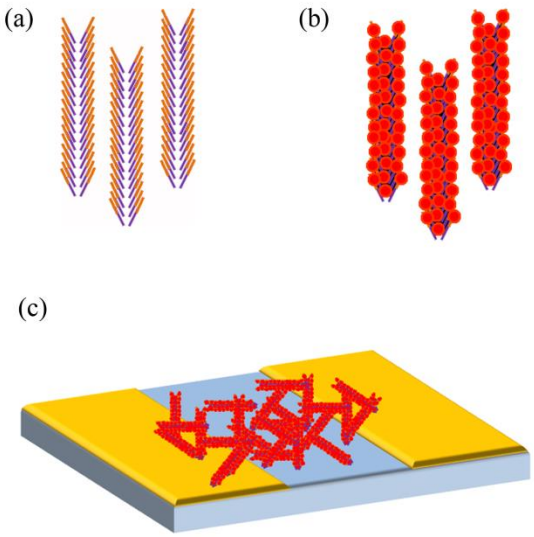

Figure 35. Schematic overview of the viral-templated $Cu_{1.8}S$ NH_3 sensor fabrication process. (a) An M13 phage with three glutamic acid residues (-EEE-, orange) fused to each copy of its major coat protein (purple) was used as a bio-template. (b) $Cu_{1.8}S$ nanomaterials were synthesized on phage template. (c) $Cu_{1.8}S$-coated phage were drop cast onto pre-patterned Au electrodes to form chemiresistors.

5.2.2 Measurement of initial resistances

Resistances of fresh samples were measured immediately. Two terminal current-voltage (I-V) measurements were performed on the devices by sweeping the voltage from -0.3 to 0.3 V (Keithley 2636A sourcemeter). The initial resistances of the devices were used to select devices for gas sensing experiments.

5.2.3 Gas sensing measurements

For sensing purposes, fresh samples were prepared and selected devices were wire-bonded (West-bond Inc. 7499D) onto a copper printed circuit board with 1% Si/Al wire. The sensors were placed in a closed cell chamber and dry air was introduced for 5 h to establish a stable baseline. Then, the devices were alternately exposed to increasing concentrations of NH_3 and dry air under a constant flow rate of 200 sccm, for 15 min and 30 min, respectively. The NH_3 concentration and exposure time were regulated by a mass flow controller with computer interface. The resistance change of the devices was recorded while applying a constant bias of 0.15 V. A similar procedure was used to evaluate sensor selectivity against carbon monoxide (CO). All gas sensing measurements were performed under ambient temperature and pressure.

5.3 Results and Discussion

5.3.1 Device morphology

Electron microscopy images of a viral-templated NH_3 sensor and the $Cu_{1.8}S$ nanomaterials of which it is comprised are shown in figure 36. Each device was composed of a single $Cu_{1.8}S$-coated phage agglomerate approximately 2-4 μm in width.

Each loose agglomerate formed a disorganized, but continuous fiber mesh which bridged the gap between electrodes. Variations in fiber diameter and length, as well as mesh density were observed within each agglomerate. A TEM image of an individual $Cu_{1.8}S$-coated fiber is shown in the inset of figure 36 (b). Full characterization of these nanocrystalline materials including transmission electron microscopy, electron diffraction, energy dispersive x-ray spectroscopy, and x-ray photoelectron spectroscopy has been published elsewhere and discussed in sections 3.3.3 and 4.3.4 [111, 139].

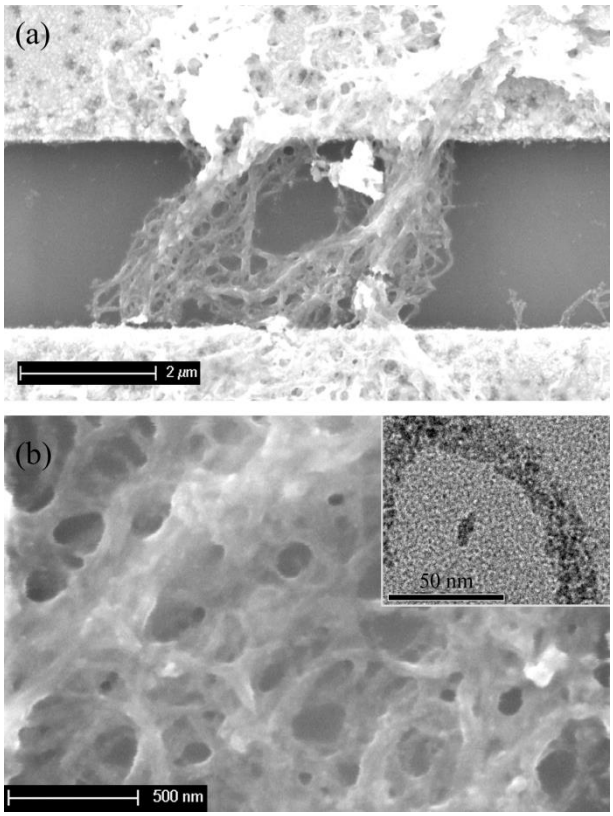

Figure 36. SEM images of (a) NH_3 gas sensor in which gold electrodes, seen at the top and bottom of the image, were connected by an agglomerate of phage-templated, nanocrystalline $Cu_{1.8}S$ and (b) composite $Cu_{1.8}S$-coated phage template materials. Inset shows TEM image of $Cu_{1.8}S$-coated phage fiber.

5.3.2 Electrical resistances of devices

The drop cast devices exhibited a range of electrical behaviors, therefore two terminal measurements were used to select devices in which to study sensing performance. A characteristic current-voltage (I-V) curve for the selected devices is shown in figure 37. The electrical behavior was symmetrical with a linear region between -0.1 V and 0.1 V. Resistances measured within this region were between 10 and 70 MΩ.

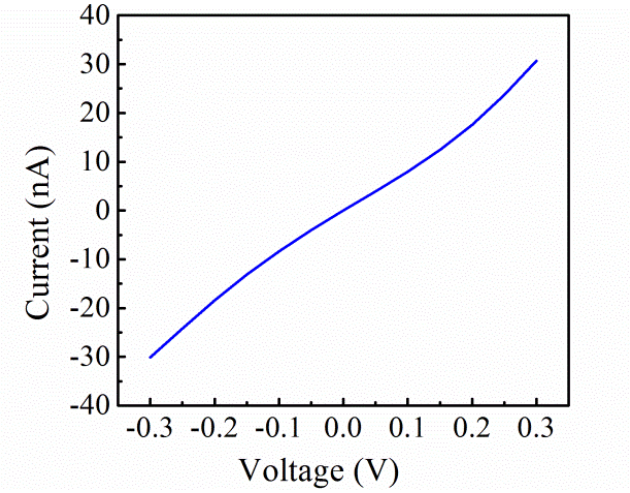

Figure 37. I-V characteristic of viral-templated $Cu_{1.8}S$ NH_3 gas sensor.

5.3.3 Gas sensing response

A representative room-temperature sensor response is shown in figure 38 (a) as a function of time for NH_3 concentrations between 10 and 80 ppm. The sensor response is defined as the percentage change in resistance compared to the baseline resistance ($\Delta R/R_0$ x 100%). Device resistance initially decreased with dry air flow, but a stable baseline was established within 5 h. At concentrations at or above 10 ppm, sensor resistance increased in the presence of NH_3 and decreased toward the baseline resistance when purged with dry air. Below 10 ppm, the signal-to-noise level of the device was too

low to clearly detect a resistance change, suggesting a lower detection limit (LDL) near 10 ppm. The measured increase in device resistance was consistent with previous reports of Cu_xS-based chemiresistors in which the adsorption of reducing gas NH_3, donates electrons to the p-type semiconductor lowering free carrier concentration in the sensing material [103]. The NH_3 calibration curve for the viral-templated $Cu_{1.8}S$ sensors is plotted in figure 38 (b). The average response increased with NH_3 concentration from 13% at 10 ppm to 73% at 80 ppm and response saturation was not observed. These average responses were greater than those of planar Cu_xS films [103, 132]. Thick chemically deposited $Cu_{1.38}S$ and $Cu_{1.8}S$ films exhibited approximately 13% and 5% response near 1000 ppm, respectively, and even lower responses at lower NH_3 concentrations [132]. Furthermore, thin CuS, $Cu_{1.4}S$, and Cu_2S films produced responses of no more than 25% at 80 ppm NH_3 [103]. The improved performance over planar thin films was attributed to the large surface-to-volume ratio of nanoscale viral-templated $Cu_{1.8}S$. Indeed, comparable or higher responses have been reported for other nanomaterial-based Cu_xS chemiresistors. Layers of 200 nm diameter CuS nanoshells which were synthesized using a surfactant micelle template exhibited responses of 60-75% at 20-100 ppm NH_3 and 210^oC [134], furthermore thin Cu_xS films chemically deposited on microporous silicon substrates produced responses of 20-290% in 45% relative humidity between 10-150 ppm NH_3 [138]. In addition to a large surface-to-volume ratio, the incorporation of the E3 phage within the $Cu_{1.8}S$ viral-templated materials may have contributed to sensor response. McAlpine et al. reported selective affinity for NH_3 using an oligopeptide composed of six glutamic acid residues (E6) covalently bound to a silicon nanowire

[140]. The resulting chemiresistive sensors attained a response of nearly 50% at 100 ppm NH_3 [140]. Furthermore, Hlavay et al. [141] and Shen et al. [142] demonstrated selective NH_3 detection using crystal quartz monitor and surface acoustic wave devices, respectively, coated with L-glutamic acid hydrochloride. Both types of sensors were able to sense NH_3 concentrations below 1 ppm. Response was attributed to a reaction between the carboxyl group of the glutamate and ammonia gas. Despite the difference in length and form compared to the E6 oligopeptide and L-glutamic acid, the high density of carboxyl-containing glutamate residues fused to each of the approximately 2700 copies of the pVIII protein found along the length of the E3 phage template may have conferred an additional degree of NH_3 sensitivity to the $Cu_{1.8}S$ to which it was bound.

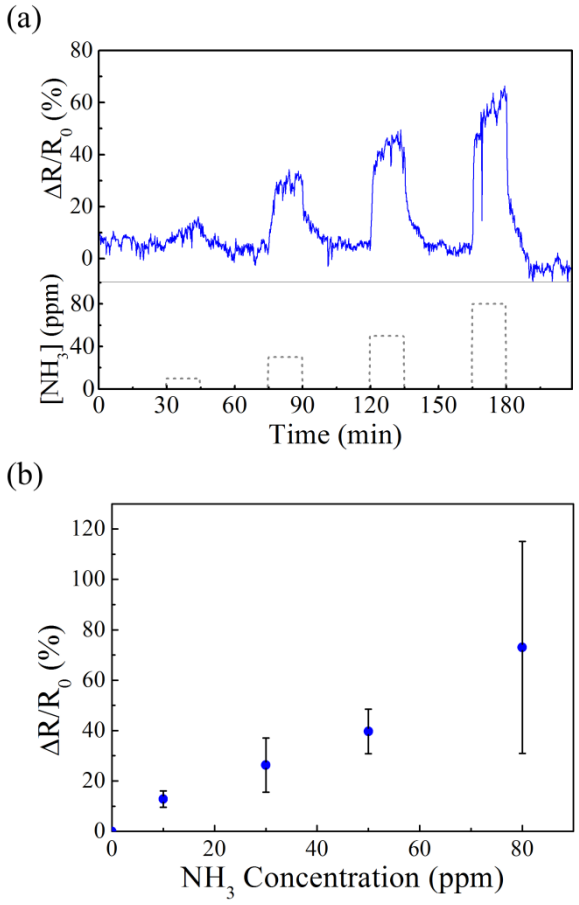

Figure 38. (a) Representative real-time response and corresponding gas concentrations and (b) calibration curve of viral-templated $Cu_{1.8}S$ NH_3 gas sensors. Error bars represent one standard deviation (n = 4). (Data taken courtesy of Chung Hee Moon)

To briefly evaluate the stability of the viral-templated devices, I-V and room-temperature sensor response were measured for devices which had been stored at ambient temperature and pressure for three days. On average, an increase in resistance was observed for these devices, however the response of these devices to NH_3 gas was comparable or slightly better than freshly made devices. More extensive studies are

required to understand device behavior under prolonged atmospheric exposure. A representative gas response curve along with the calibration curve is shown in figure 39.

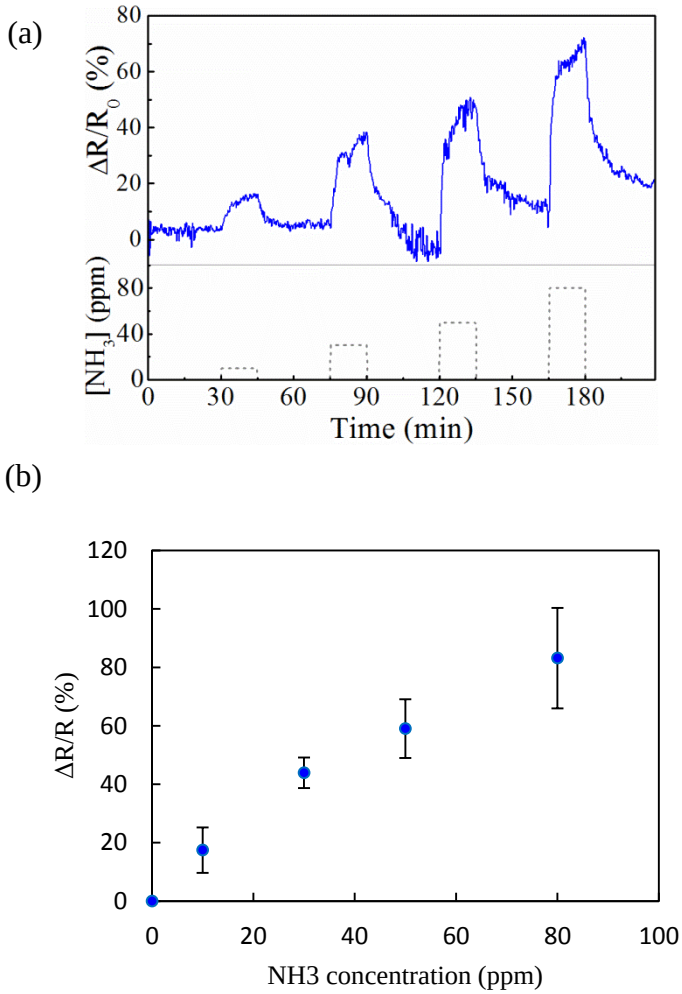

Figure 39. (a) Representative gas response of device exposed under ambient conditions for 3 days and corresponding NH_3 gas concentration (b) calibration curve of the devices.

The response time, defined as the time for the sensor resistance to reach 90% of its saturation value, was greater than the 15 min NH_3 exposure period. The recovery time, defined as the time for the sensor resistance to return to 10% above its baseline

resistance, varied. Yet, all sensors recovered a minimum of 67% within the 30 min dry air purge. Overall, the viral-templated device transients were relatively slow compared to other Cu_xS-based chemiresistors [103, 132, 133, 135, 137, 138]. Published response and recovery times have been 10s of seconds to a few minutes at most, although poisoning of the sensor surface was observed at higher NH_3 concentrations (>300-500 ppm) leading to much longer recovery times [132, 138]. Further experiments are necessary to better understand the sluggish behavior of the viral-templated NH_3 sensors.

As shown in figure 40, cross-sensitivity was not detected for CO gas concentrations between 10 and 500 ppm. In addition to agricultural and industrial sites, ammonia sensors are frequently used for automotive emission control and exhaust monitoring in which both NH_3 and CO are present. Strong selectivity for NH_3 over CO is important for these applications.

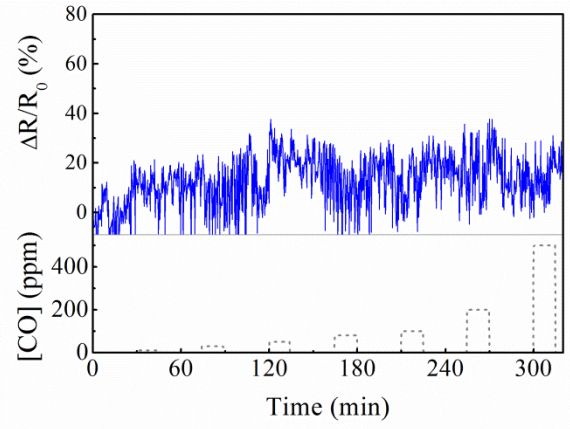

Figure 40. Real-time response and corresponding gas concentrations of viral-templated $Cu_{1.8}S$ sensors to CO gas. No measurable change in resistance was attributed to CO gas exposure. (Data taken courtesy of Chung Hee Moon)

5.4 Conclusion

In summary, we have fabricated a chemiresistor from viral-templated $Cu_{1.8}S$ for the detection of NH_3 gas at ambient temperature. Specifically, an M13 bacteriophage with a peptide comprised of three glutamic acid residues fused to each major coat protein was used as a nanoscaffold. Each device was made up of a single agglomerate of $Cu_{1.8}S$/virus composite material with a resistance on the order of tens of megaohms. These sensors exhibited a LDL of 10 ppm, which is below both the PEL and IDLH established by OSHA for NH_3. An average response of 13% and 73% was measured at 10 ppm and 80 ppm, respectively. In comparison to planar thick and thin films of CuS, $Cu_{1.4}S$, $Cu_{1.8}S$, and Cu_2S, these devices demonstrated superior NH_3 sensitivity. The response of these viral-templated devices also rivaled that of non-planar materials such as CuS nanoshells. The large surface to volume ratio of these nanomaterials and the high concentration of glutamic acid on the viral protein coat likely contributed to the high sensor response. Viral templates such as the M13 offer a one-step manufacturing approach for sensitive Cu_xS-based room temperature NH_3 gas sensors.

6 Viral-templated Copper Oxide

6.1 Introduction

Biomolecules can be used to assemble or synthesize both copper (Cu) and copper oxides (CuO, Cu_2O). Highly anisotropic nanoscale bio-scaffolds, which are useful for applications which necessitate a large surface to volume ratio and a one-dimensional pathway for transport, are of particular interest. Both uniaxial organization of smaller components and creation of continuous rod- or wire-like structures have been studied. Tobacco mosaic viruses (TMV) [77], cellulose fibers [143], and peptide nanotubes [25] have demonstrated assembly of Cu-based nano-building blocks into linear arrays 100s to 1000s of nanometers in length using weak electrostatic interactions, polyphenol compounds, and histidine binding, respectively. In addition, continuous nanorods of CuO have been synthesized with a combination of amino, carboxylic, and phenolic groups found in Aloe vera plant extracts [144]; and uninterrupted, electrically-conductive Cu and Cu_2O nanowires several microns long have been formed from Cu^{2+} ions reduced via the phosphate backbone of deoxyribonucleic acid (DNA) [145, 146]. Finally, histidine loops displayed on bioengineered flagella have been shown to produce either Cu nanoparticle chains or continuous tubes, depending on synthesis conditions [75].

In this chapter, we demonstrate copper oxide mineralization using an M13 bacteriophage template. Previous studies have used palladium (Pd)-activated electroless deposition on the M13 to create Cu nanowires 10s of nanometers in diameter [147]. Yet, Pd is not only expensive, but can alter semiconductor properties and resulting device

performance if incorporated as a dopant. Alternatively, a recently reported genetic modification in which the N-terminus peptide sequence AEGD- is replaced by AEEE- has further enhanced negative surface charge enabling a variety of nanoscale materials to be synthesized [33, 87, 88, 111]. Here, this M13 clone, which is referred to as E3, was used to assemble chains of discrete, mixed phase copper oxide nanoparticles at room temperature, without Pd-activation. These nanocrystals were highly uniform in size, shape, and regularity along the template and exhibited strong UV/visible optical absorption.

6.2 Experimental Details

6.2.1 Synthesis method

An M13 bacteriophage was used to template nanocrystalline copper oxide. This filamentous virus, which will hereafter be referred to as E3, displayed three glutamic acid residues at the N-terminus of each pVIII protein found along its length [33, 87, 88, 111]. To induce copper oxide formation in solution, the E3 template was first mixed with 200 mM copper chloride ($CuCl_2$, Acros Organics), and then 200 mM sodium borohydride ($NaBH_4$, Sigma Aldrich) was added under ambient conditions. Specifically, equal parts of 10^9 pfu/μL E3 phage and $CuCl_2$ were combined to a final volume of 200 μL and incubated undisturbed for 2 hours. Then, 100 μL of $NaBH_4$ was added dropwise in 5 μL increments over a period of 30 min. The solution was mixed gently by inverting the tube after each $NaBH_4$ addition. Synthesis products were separated using centrifugation and

rinsed with deionized water. Fresh $CuCl_2$ and $NaBH_4$ solutions were prepared for each synthesis.

6.2.2 Fourier transform infrared spectroscopy characterization

Fourier transform infrared spectroscopy (FTIR, Nicolet 6700) was used to study the interactions between the template and the copper precursor. Samples were prepared for analysis using an approach which was similar to that used for synthesis. Equal parts of 10^9 pfu/μL E3 phage and $CuCl_2$ were combined to a final volume of 200 μL and incubated undisturbed for 2 hours. The phage aggregates were then pelleted by centrifugation, rinsed with deionized water to remove unbound precursor, and resuspended. For comparison, samples were also prepared from E3 phage at a concentration of 10^{11} pfu/μL in deionized water. Spectra were measured between 525 cm^{-1} and 4000 cm^{-1} with a 2 cm^{-1} resolution and 128 scans.

6.2.3 Structural, Compositional and Elemental Characterization

Transmission electron microscopy (TEM, FEI Tecnai12 and CM300) and energy dispersive x-ray (EDX) spectroscopy were used to examine interactions between the template and copper precursor, as well as to study the morphology, size, and elemental composition of the synthesized materials. Furthermore, electron diffraction was used to determine the crystal structure of the nanomaterials. For TEM analysis, a 5 μL volume of either rinsed and resuspended phage aggregates or synthesis product was drop-cast onto carbon coated Ni grids, incubated for 5 min, and rinsed twice with deionized water.

6.2.4 Optical characterization

The optical absorption of films of viral-templated copper oxide was measured under ambient conditions from 360 nm to 2300 nm using a spectrophotometer (Cary 500 UV/Vis/NIR), neglecting reflection and scattering losses. To prepare films, the E3 phage template was first dried on glass slides and then copper oxide was synthesized on the templates using the previously described synthesis process. After synthesis, the films were rinsed with deionized water to remove excess precursors, dried, and measured. The morphology and thickness of the phage-templated film were evaluated with scanning electron microscopy (SEM, XL30 FEG). Film thickness was determined using cross-sectional measurements in 50 locations.

6.3 Results and Discussion

6.3.1 Binding mechanism study

As shown in figure 41 (a), large agglomerates were observed with TEM following incubation of the E3 phage in $CuCl_2$. Aggregation of rod or filamentous viral templates has been commonly observed in solutions of multivalent metal cations in which the concentration of positively charged metal ions is high enough to screen the negative surface charge of the virus, significantly reducing repulsive forces [77, 84, 85, 89]. Specifically, this electrostatically-based behavior has been reported for the E3 M13 virus in solutions containing Cu^{2+} [111], Co^{2+} [62], and Ba^{2+} [148] ions. EDX spectroscopy confirmed the presence of Cu within these agglomerates as shown in figure 41 (b),

supporting the hypothesis that Cu ions were bound to the template during the incubation step.

FTIR was used to further explore the nature of the interaction between the copper ions and viral template. A representative FTIR spectrum of E3 phage is shown in figure 42. Several characteristic features were present. The two most prominent bands were located at 1648 cm^{-1} and 1550 cm^{-1}. These bands were correlated with the amide I region which is related to C=O stretching vibrations and the amide II region which is related to in-phase N-H bending and C-N stretching vibrations [149-151]. Two broad bands associated with the amide III region, or out-of-phase N-H bending and C-N stretching vibrations, were also identified at 1309 and 1237 cm^{-1} [150-152]. The absorption band found at 1458 cm^{-1} was identified as a combination of scissoring and bending modes of CH_2 and asymmetric bending modes of CH_3, whereas the absorption band at 1401 cm^{-1} was attributed to symmetric CH_3 bending vibrations [150-152]. The bands near 1172 cm^{-1} and 1087 cm^{-1} were associated with C-C and C-OH stretching, and C-O stretching [148, 152] respectively. As shown in figure 42, following incubation with $CuCl_2$, the amide I and amide II bands were broadened, and peaks associated with –C=O stretching were down shifted in wavenumber indicating that Cu ions complexed with carboxyl groups. Similar changes in FTIR spectra have been reported for fd phage, a filamentous phage which is structurally similar to M13 phage, via Ca^{2+} ion coordination with the carboxyl groups in aspartic and glutamic acid residues [84] and M13 phage via Ba^{2+} coordination with the carboxyl groups in glutamic acid residues [148].

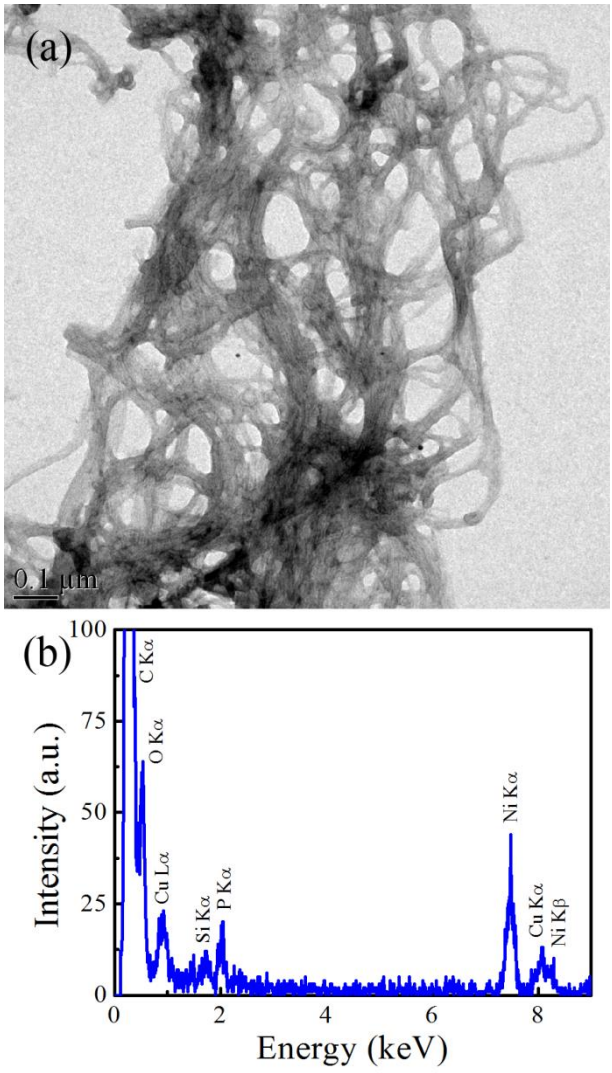

Figure 41. (a) A TEM image of phage agglomeration after incubation with $CuCl_2$ (stained with 1% uranyl acetate for visualization purposes). (b) An EDX spectrum indicating the presence of Cu ions bound to phage agglomerates. The observed C, O, and P peaks were associated with the nucleic acids and structural proteins of the phage template, and the Ni and Si peaks were attributed, respectively, to the TEM grid and detector.

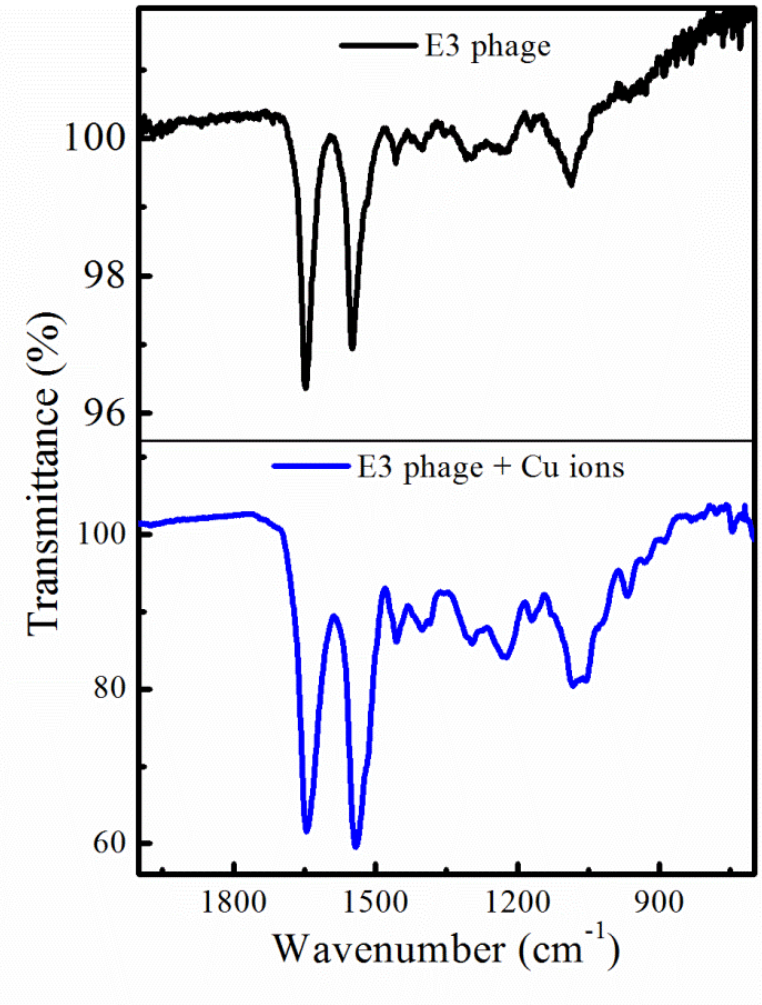

Figure 42. FTIR spectrum of E3 phage (top) and E3 phage following incubation with $CuCl_2$ (bottom).

6.3.2 Structural characterization

After incubation with $CuCl_2$, synthesis was completed by adding $NaBH_4$ to reduce copper ions bound to the viral template. As shown in figure 43, the previously observed phage agglomerates remained intact throughout the synthesis process. As shown in the high magnification TEM image in figure 44 (a), these large fiber-like structures were composed of closely packed, but discrete spherical nanoparticles which were arranged in

chains. A histogram of nanoparticle diameter is shown in the figure 44 (b). The nanoparticles had a narrow size distribution with an average nanoparticle diameter of 4.5 ± 0.7 nm. Compared to other copper oxide and copper nanoparticles synthesized on high aspect ratio bio-templates without Pd-activation, these particles were smaller and more uniform in size and spacing. The carboxylic acid-rich exterior surface of the rod-like wild-type tobacco mosaic virus demonstrated an ability to readily bind divalent copper cations, but displayed only a low affinity for solid Cu clusters resulting in sparse nanoparticle coverage [77]. Moreover, nanofibrillar cellulose manifested only minimal coverage of 3-13 nm diameter Cu-CuO nanoparticles [153], whereas tunicate cellulose formed a relatively narrow distribution of 5 nm diameter Cu nanoparticles but agglomeration occurred along the fiber surface [143]. It is also notable that, unlike λ-DNA [145] or flagella functionalized with histidine peptide loops [75], the nanoparticles on the E3 phage remained discrete rather than forming a continuous nanocrystalline layer even at high $CuCl_2$ concentrations. Materials prepared without the E3 phage template resulted in a dissimilar morphology. Rather than chains of nanoparticles, agglomerates of nanoparticles with an average diameter of 5.1 nm and cubic structures approximately 200 nm in size were produced. Thus, the E3 phage template facilitated the mineralization of spherical nanocrystals, creating ordered arrangement of distinct but closely packed particles.

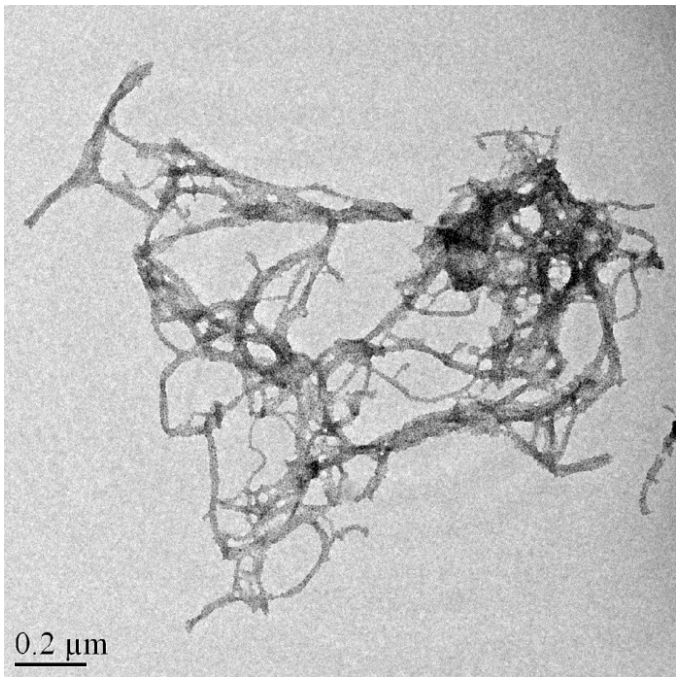

Figure 43. Agglomerate of phage coated with synthesized material.

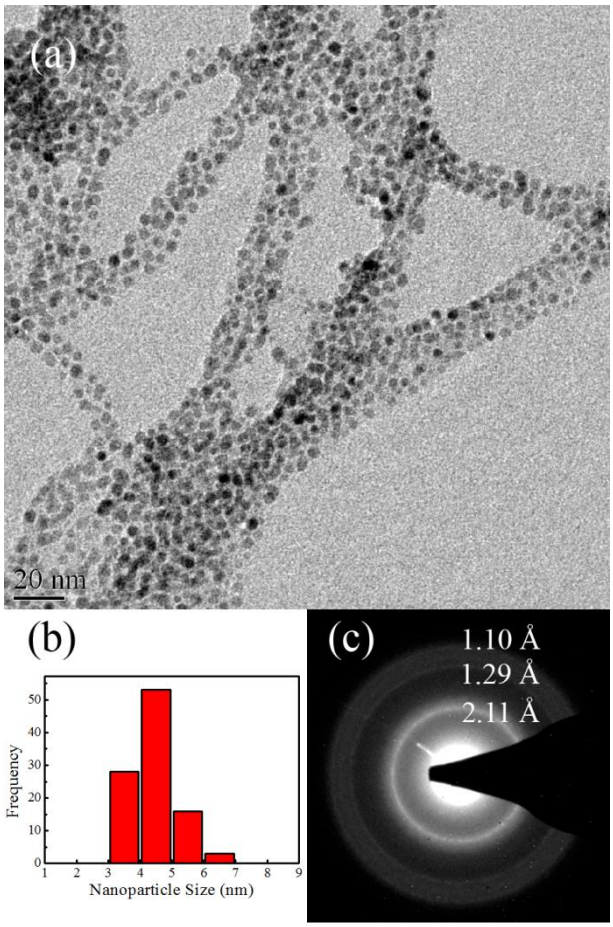

Figure 44. (a) High magnification TEM image of nanoparticles synthesized on E3 phage templates. (b) Size distribution of templated nanoparticles. (c) Electron diffraction pattern of the synthesized material.

6.3.3 Compositional and elemental characterization

The elemental composition and crystalline structure of the synthesis products were analyzed using EDX spectroscopy and electron diffraction. As shown in figure 45, both Cu and O were found within the nanoparticles. The additional peaks within the EDX spectrum were identified as the C Kα line, which was attributed to the carbon support film and phage template, and the Ni Kα and Si Kα lines, which were associated

with the Ni grid and Si detector, respectively. A selected area electron diffraction pattern of the templated material is shown in figure 44 (c). The observed ring pattern of the polycrystalline synthesis product had measured d-spacings of 2.11 Å, 1.29 Å, and 1.10 Å. These interplanar distances were indexed to the (200) and (311) planes of cubic Cu_2O, space group $Pn\bar{3}m$, (a = 4.2685 Å) [154] and the $(\bar{1}31)$ plane of monoclinic CuO, space group C2/c, (a = 4.6837 Å, b = 3.4226 Å, c = 5.1288 Å, β = 99.540) [155] indicating a mixture of the semiconducting copper oxides cuprite and tenorite was present. It is clear, that although some bio-templates, including the cage-like protein apoferritin [156] and histidine functionalized peptide nanotubes [25], are capable of inhibiting copper oxidation under similar conditions, the E3 phage template was not. This was likely due to the fractional coverage of the copper surface by the short, three residue binding peptides. Despite the use of strong reducing agents, without suitable passivation ligands, Cu nanoparticles are known to rapidly oxidize via ambient oxygen within the aqueous solution [157, 158].

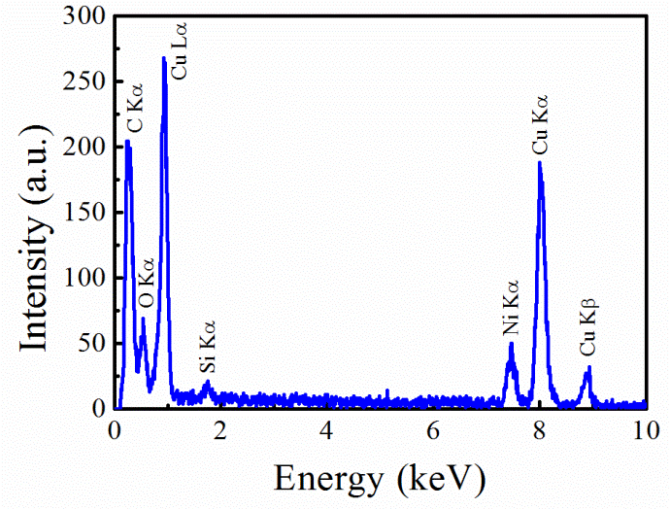

Figure 45. EDX spectrum of phage-templated material showing the presence of Cu and O.

6.3.4 Optical characterization and band gap calculation

Films of synthesized material were prepared on glass slides for UV/Vis/NIR optical absorption measurements. Representative SEM images of these films are shown in figure 46. These films had a thickness of 283 ± 63 nm and were composed of randomly oriented chains of phage-templated copper oxide nanoparticles. The optical behavior of the synthesized material is shown in figure 47 (a), from 360 nm to 2300 nm. The spectrum shows strong ultraviolet and visible absorption which can be attributed to band-to-band transitions of the synthesized semiconductor nanocrystals. The optical band gap of the synthesized materials was estimated with Tauc's method using the following relationship [159]

$$[\alpha h\nu]^n = A(h\nu - E_g)$$

where A is a constant, hν is the photon energy, Eg is the band gap, and α is the optical absorption coefficient. A coefficient, n, of 2 is used for direct band-to-band transitions. A linear fit of $(\alpha h\nu)^n$ versus hν was extrapolated to the hν axis to evaluate Eg. The resulting Tauc plot is shown in figure 47 (b). An optical band gap of 2.87 eV was found. This direct transition value is consistent with a blue-shift of the bulk band gaps of Cu_2O (2.1 eV [48]) and CuO (1.85 eV [48]). The shift to higher energy was likely caused by quantum confinement due to the small average 4.5 nm diameter of the templated nanoparticles. Quantum effects have been frequently observed in spherical Cu_2O and CuO nanoparticles with diameters less than 10 nm. For example, Borgohain et al. found optical band gaps of 3.37 eV and 2.77 eV, respectively, for 2 and 8 nm diameter Cu_2O particles synthesized using a unique electrochemical synthesis route [160]; and Balamurugan et al. measured optical band gaps of 4 and 9 nm diameter particles formed with activated reactive evaporation to be 2.9 eV and 2.5 eV, respectively [161]. Furthermore, Wang et al. [162] and Son et al. [163] have reported optical band gaps of 2.43 eV and 3.63 eV for 3-5 nm diameter CuO particles synthesized via microwave irradiation and a colloidal-thermal process, respectively.

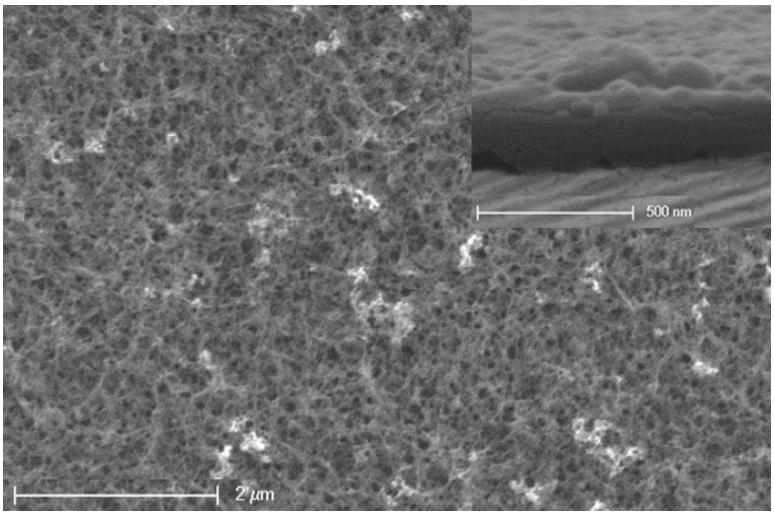

Figure 46. SEM image of phage-template Cu_2O/CuO film showing randomly oriented phage covered with synthesized material. Inset: SEM cross-section image of the film showing the thickness.

Aside from the strong band-to-band absorption observed at shorter wavelengths, the spectrum was featureless. Localized surface plasmon resonance (LSPR) absorption, which is predicted by Mie theory [112, 164, 165] and experimentally confirmed by other researchers [165, 166] for Cu nanoparticles greater than 2 nm in diameter, was not observed for these materials. This optical behavior further supports EDX and electron diffraction data suggesting that the viral-templated material was oxidized. The discontinuity near 800 nm is an artifact of the spectrophotometer detector and grating change at this wavelength.

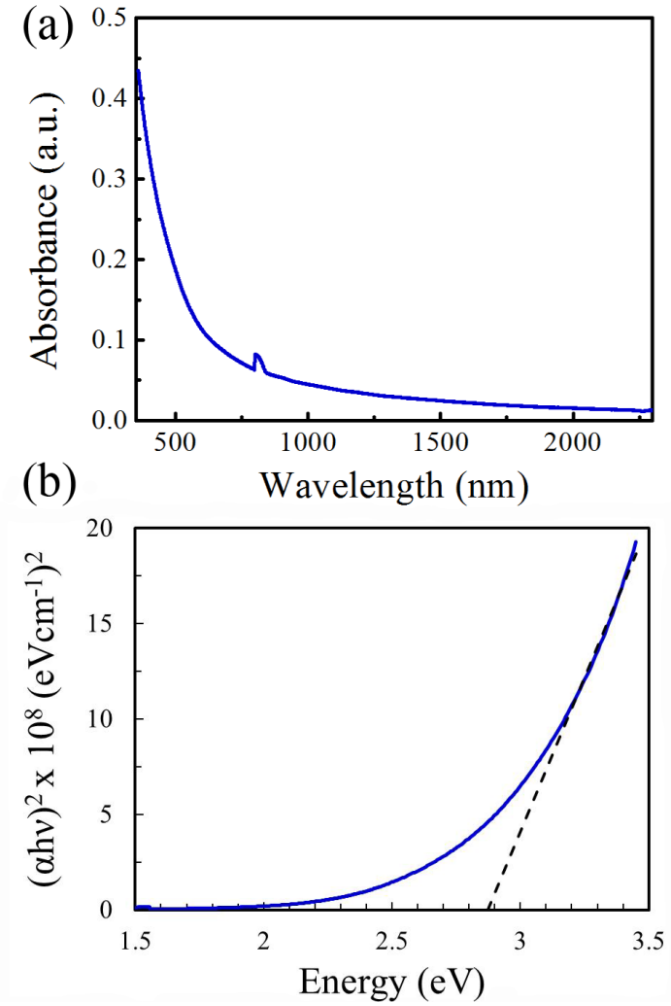

Figure 47. (a) Absorption spectrum of the synthesized material from 360 nm to 2300 nm. (b) Plot of $(\alpha h\nu)^2$ vs. energy for direct optical band gap calculation. The blue solid line is the measured spectrum and the black dashed line is the linear fit of the data.

6.4 Conclusion

Viral-templated copper oxide has been synthesized using an M13 filamentous bacteriophage without an initial Pd-activation step at room temperature. In particular, a clone known as E3, in which the wild-type N-terminus peptide sequence AEGD- was replaced by AEEE- to enhance negative surface charge, was utilized. As evidenced by TEM, EDX, and FTIR data, during incubation with the Cu precursor, Cu ions bound to carboxyl groups on the viral surface and large Cu-phage agglomerates were formed. $NaBH_4$ was used to reduce the bound ions which readily oxidized, generating fairly monodisperse nanoparticles with an average diameter of 4.5 nm regularly spaced along the templates. The synthesized material was a mixture of Cu_2O and CuO. Absorption measurements in conjunction with Tauc's technique were used to determine the direct optical band gap of the materials, revealing quantum confinement effects within the small diameter nanoparticles. The control demonstrated by the M13 bacteriophage over nanoparticle uniformity, size, spacing, and long range organization of semiconductor nano-building blocks is advantageous for applications which require both high surface to volume ratios and directional transport. Bio-assisted synthesis and assembly approaches such as this one are potentially valuable tools for the design and construction of next generation nanoscale materials and devices.

7 Conclusion and Future work

In this dissertation we have developed a method for synthesizing bio-templated copper sulfide and copper oxide nanoparticles along the entire length of the bacteriophage. We have utilized the bio-templated copper sulfide to study their optical and electrical properties and stabilities. As a device application we prepared an NH3 gas sensor with the copper sulfide material. We synthesized and studied the optical properties of the synthesized copper oxide nanoparticles.

In our review we found that the M13 bacteriophage was not previously utilized to mineralize copper sulfide semiconductor nanomaterials. Our first approach was to identify a peptide through phage display technique that would bind to copper sulfide and which eventually could be used to mineralize copper sulfide. The sequences that were identified from the pIII library could not be proved to conclusively bind to copper sulfide or mineralize. The genetically modified pIII sequence HG12 was also used to bind and nucleate copper sulfide, which was not successful either. Next the pVIII library was used to biopan against copper sulfide and a binding sequence was identified. Although the binding test with this peptide was not conclusive, nucleation with this peptide resulted in nanoparticles of copper sulfide being mineralized along the length of the virus. These nanocrystals were discontinuous in nature. The yield of this process was very low which necessitated the need for a more robust, reliable and repeatable synthesis process.

The approach that we adopted for a more reliable process was based on utilizing non-specific electrostatic interactions between the negatively charged phage surface and the positively charged cations. The positively charged Cu ions bound to the phage

surface. The binding mechanism was showed to be electrostatics and the C=O bonds were possibly interacting with the positive Cu ions. The incubation of the more negatively charged E3 phage with Cu precursor resulted in large agglomerates of phage which upon addition of Na_2S nucleated copper sulfide along the entire length of the phage template. The composition of the mineralized material was identified to be a slightly copper deficient phase $Cu_{1.8}S$.

After synthesizing $Cu_{1.8}S$ we focused on studying the optical and electrical properties of the material. The material was found to be optically absorbing. The nanoparticles showed absorption in the visible and UV region due to band-to-band transitions. Interestingly, the material also showed LSPR absorption similar to metal nanoparticles. This was attributed to the high density of free carriers in the copper deficient phase. The material was found to be optically changing behavior with time, increasing in LSPR strength upon exposure under ambient conditions. The material was also found to be conductive and Ohmic in nature. The electrical resistance of the material was found to decrease with time. The surface of the material was found to be forming $CuSO_4$ upon exposure with time which was extracting Cu ions from within the core of the material, depleting it and making the material more conductive with time.

We utilized the bio-templated $Cu_{1.8}S$ material to develop an NH_3 gas sensor. The ammonia gas consisting of a lone pair electron donates them to the material which decreased the effective number of holes in the material, thereby increasing the resistance of the material upon exposure to ammonia gas. The devices were able to detect ammonia gas from 10 ppm to 80 ppm. The device showed greater or comparable response to other

copper sulfide based ammonia gas sensors. The greater response of the devices was attributed to the larger surface-to-volume ratio of the material. This device shows that the phage-templated copper sulfide material could successfully be utilized to sense ammonia gas.

The next step for the bio-templated copper sulfide would be to try to control the composition of the material with the phage template. In our template we have utilized the non-specific electrostatic interactions for mineralizing copper sulfide. If a specific peptide could be bio-conjugated on the pVIII coat protein then it could be utilized to mineralize a specific composition of copper sulfide. For example the HG12 peptide which is capable of mineralizing Cu_2S [74] could be bio-conjugated on the pVIII coat protein and used for mineralization. This could ensure a composition specific nucleation on the phage template. Of course the inclusion of another peptide capable of nucleating a second material would open up the possibility to utilize these hybrid phage templates for various applications. Similar heterostructured phage was constructed by Mao et al. in which they were able to mineralize both ZnS and CdS on the same phage template, though the peptides were identified through phage screening [28]. The inclusion of CdS on the same phage template consisting of copper sulfide could facilitate the formation a type II junction between the two materials. These type of junctions could be used for photovoltaic applications [167-169]. Another application would be to try to nucleate ZnO on the same phage along with the copper sulfide. This would help to utilize these materials for photocatalysis applications [170].

Of course an important step to utilize these materials would be to stabilize the copper sulfide material before various devices could be produced which requires a particular composition of copper sulfide. So far our studies have showed that the material was changing behavior with time. To stabilize the material the phage templated material could be coated with a protective layer of material that would inhibit the diffusion of environmental oxygen into the copper sulfide. Martinson and Riha are exploring various materials as protective layers on the copper sulfide to stop or slow down the oxidation effect [107, 110].

The versatility of the synthesis process was utilized to mineralize copper oxide nanoparticles along the length of the phage template. These nanoparticles were monodisperse in size and uniformly spaced. Quantum confinement effect was observed in these materials. The synthesized material was identified to be a mixture of two types of compositions of copper oxide. At present it was not possible synthesize a particular composition of copper oxide. But in future work it may be possible to synthesize only one type of composition of copper oxide. Again, biopanning against a particular composition of copper oxide could help identify a composition specific peptide sequence which would be able to nucleate a particular composition of copper oxide. The copper oxide could be utilized to develop devices which could be used for solar cells, photocatalysis applications.

The phage-template was successfully utilized to mineralize p-type copper sulfide and copper oxide nanoparticles along the phage template. These phage templates offer the unique opportunity of incorporating bio-templated materials for future devices.

Bibliography

1. M. Hildebrand, Diatoms, Biomineralization Processes, and Genomics *Chemical Reviews* **108,** 4855 (2008)

2. M. Sumper and E. Brunner, Learning from diatoms: Nature's tools for the production of nanostructured silica *Advanced Functional Materials* **16,** 17 (2006)

3. K.F. Brandstadt, Inspired by nature: an exploration of biocatalyzed siloxane bond formation and cleavage *Current Opinion in Biotechnology* **16,** 393 (2005)

4. S.V. Patwardhan, S.J. Clarson and C.C. Perry, On the role(s) of additives in bioinspired silicification *Chem. Commun.* 1113 (2005)

5. W.E.G. Muller, S.I. Belikov, W. Tremel, C.C. Perry, W.W.C. Gieskes, A. Boreiko and H.C. Schroder, Siliceous spicules in marine demosponges (example Suberites domuncula) *Micron* **37,** 107 (2006)

6. W.E.G. Muller, A. Krasko, G. Le Pennec and H.C. Schroder, Biochemistry and cell biology of silica formation in sponges *Microscopy Research and Technique* **62,** 368 (2003)

7. W.E.G. Mueller, C. Eckert, K. Kropf, X. Wang, U. Schlossmacher, C. Seckert, S.E. Wolf, W. Tremel and H.C. Schroeder, Formation of giant spicules in the deep-sea hexactinellid Monorhaphis chuni (Schulze 1904): electron-microscopic and biochemical studies *Cell and Tissue Research* **329,** 363 (2007)

8. T. Matsunaga, T. Suzuki, M. Tanaka and A. Arakaki, Molecular analysis of magnetotactic bacteria and development of functional bacterial magnetic particles for nano-biotechnology *Trends in Biotechnology* **25,** 182 (2007)

9. D. Schuler and R.B. Frankel, Bacterial magnetosomes: microbiology, biomineralization and biotechnological applications *Applied Microbiology and Biotechnology* **52,** 464 (1999)

10. A. Arakaki, J. Webb and T. Matsunaga, A novel protein tightly bound to bacterial magnetic particles in Magnetospirillum magneticum strain AMB-1 *Journal of Biological Chemistry* **278,** 8745 (2003)

11. N. Hu and B. Zhao, Key genes involved in heavy-metal resistance in Pseudomonas putida CD2 *Fems Microbiology Letters* **267,** 17 (2007)

12. X.Z. Li, H. Nikaido and K.E. Williams, Silver-resistant mutants of Escherichia coli display active efflux of Ag+ and are deficient in porins *Journal of Bacteriology* **179,** 6127 (1997)

13. R.Y. Sweeney, C.B. Mao, X.X. Gao, J.L. Burt, A.M. Belcher, G. Georgiou and B.L. Iverson, Bacterial biosynthesis of cadmium sulfide nanocrystals *Chemistry & Biology* **11,** 1553 (2004)

14. B. Nair and T. Pradeep, Coalescence of nanoclusters and formation of submicron crystallites assisted by Lactobacillus strains *Crystal Growth & Design* **2,** 293 (2002)

15. S.H. Yu, Bio-inspired Crystal Growth by Synthetic Templates *Topics in Current Chemistry* **271,** 79 (2007)

16. C.L. Chen and N.L. Rosi, Peptide-Based Methods for the Preparation of Nanostructured Inorganic Materials *Angewandte Chemie International Edition* **49,** 1924 (2010)

17. R.R. Naik, P.W. Whitlock, F. Rodriguez, L.L. Brott, D.D. Glawe, S.J. Clarson and M.O. Stone, Controlled formation of biosilica structures in vitro *Chem. Commun.* 238 (2003)

18. M.B. Dickerson, K.H. Sandhage and R.R. Naik, Protein- and Peptide-Directed Syntheses of Inorganic Materials *Chemical Reviews* **108,** 4935 (2008)

19. S. Brown, Metal-recognition by repeating polypeptides *Nature Biotechnology* **15,** 269 (1997)

20. R. Djalali, Y.F. Chen and H. Matsui, Au nanocrystal growth on nanotubes controlled by conformations and charges of sequenced peptide templates *Journal of the American Chemical Society* **125,** 5873 (2003)

21. J.L. Burt, C. Gutierrez-Wing, M. Miki-Yoshida and M. Jose-Yacaman, Noble-metal nanoparticles directly conjugated to globular proteins *Langmuir* **20,** 11778 (2004)

22. J.L. Sumerel, W.J. Yang, D. Kisailus, J.C. Weaver, J.H. Choi and D.E. Morse, Biocatalytically templated synthesis of titanium dioxide *Chemistry of Materials* **15,** 4804 (2003)

23. K.K.W. Wong and S. Mann, Biomimetic synthesis of cadmium sulfide-ferritin nanocomposites *Advanced Materials* **8,** 928 (1996)

24. E. Dujardin, C. Peet, G. Stubbs, J.N. Culver and S. Mann, Organization of Metallic Nanoparticles Using Tobacco Mosaic Virus Templates *Nano Letters* **3,** 413 (2003)

25. I.A. Banerjee, L.T. Yu and H. Matsui, Cu nanocrystal growth on peptide nanotubes by biomineralization: Size control of Cu nanocrystals by tuning peptide

conformation *Proceedings of the National Academy of Sciences of the United States of America* **100,** 14678 (2003)

26. M. Knez, M. Sumser, A.M. Bittner, C. Wege, H. Jeske, T.P. Martin and K. Kern, Spatially Selective Nucleation of Metal Clusters on the Tobacco Mosaic Virus *Advanced Functional Materials* **14,** 116 (2004)

27. S.W. Lee, C.B. Mao, C.E. Flynn and A.M. Belcher, Ordering of quantum dots using genetically engineered viruses *Science* **296,** 892 (2002)

28. C. Mao, C.E. Flynn, A. Hayhurst, R. Sweeney, J. Qi, G. Georgiou, B. Iverson and A.M. Belcher, Viral Assembly of Oriented Quantum Dot Nanowires *Proceedings of the National Academy of Sciences of the United States of America (PNAS)* **100,** 6946 (2003)

29. S.W. Lee, B.M. Wood and A.M. Belcher, Chiral Smectic C Structures of Virus-Based Films *Langmuir* **19,** 1592 (2003)

30. S.W. Lee and A.M. Belcher, Virus-Based Fabrication of Micro- and Nanofibers Using Electrospinning *Nano Letters* **4,** 387 (2004)

31. C. Mao, D.J. Solis, B.D. Reiss, S. Kottmann, R.Y. Sweeney, A. Hayhurst, G. Georgiou, B. Iverson and A.M. Belcher, Virus-Based Toolkit for the Directed Synthesis of Magnetic and Semiconducting Nanowires *Science* **303,** 213 (2004)

32. K.T. Nam, B.R. Peelle, S.W. Lee and A.M. Belcher, Genetically Driven Assembly of Nanorings Based on the M13 Virus *Nano Letters* **4,** 23 (2004)

33. K.T. Nam, D.W. Kim, P.J. Yoo, C.Y. Chiang, N. Meethong, P.T. Hammond, Y.M. Chiang and A.M. Belcher, Virus Enabled Synthesis and Assembly of Nanowires for Lithium Ion Battery Electrodes *Science* **312,** 885 (2006)

34. S.W. Lee, S.K. Lee and A.M. Belcher, Virus Based Alignment of Inorganic, Organic and Biological Nanosized Materials *Advanced Materials* **15,** 689 (2003)

35. Z.W. Niu, M.A. Bruckman, B. Harp, C.M. Mello and Q. Wang, Bacteriophage M13 as a Scaffold for Preparing Conductive Polymeric Composite Fibers *Nano Res.* **1,** 235 (2008)

36. J.A. Arter, D.K. Taggart, T.M. McIntire, R.M. Penner and G.A. Weiss, Virus-PEDOT Nanowires for Biosensing *Nano Letters* **10,** 4858 (2010)

37. D.A. Marvin, FILAMENTOUS BACTERIAL-VIRUSES *Journal of Biosciences* **8,** 799 (1985)

38. L. Makowski, Phage display: structure, assembly and engineering of filamentous bacteriophage M13 *Current Opinion in Structural Biology* - **4,** (1994)

39. S. Cabilly, The Basic Structure of Filamentous Phage and its Use in the Display of Combinatorial Peptide Libraries *Molecular Biotechnology* **12,** 143 (1999)

40. W.O. Salivar, H. Tzagoloff and D. Pratt, SOME PHYSICAL-CHEMICAL + BIOLOGICAL PROPERTIES OF ROD-SHAPED COLIPHAGE M13 *Virology* **24,** 359 (1964)

41. S.S. Sidhu, Engineering M13 for Phage Display *Biomolecular Engineering* **18,** 57 (2001)

42. D.J. Chakrabarti and D.E. Laughlin, The Cu-S (Copper-Sulfur) System *Bulletin of Alloy Phase Diagrams* **4,** 254 (1983)

43. T.S. Moss, THE INTERPRETATION OF THE PROPERTIES OF INDIUM ANTIMONIDE *Proceedings of the Physical Society of London Section B* **67,** 775 (1954)

44. E. Burstein, ANOMALOUS OPTICAL ABSORPTION LIMIT IN INSB *Physical Review* **93,** 632 (1954)

45. B.J. Mulder, OPTICAL PROPERTIES OF CRYSTALS OF CUPROUS SULFIDES (CHALCOSITE, DJURLEITE, CU1.9S, AND DIGENITE) *Phys. Status Solidi A-Appl. Res.* **13,** 79 (1972)

46. I. Grozdanov and M. Najdoski, OPTICAL AND ELECTRICAL-PROPERTIES OF COPPER SULFIDE FILMS OF VARIABLE COMPOSITION *Journal of Solid State Chemistry* **114,** 469 (1995)

47. M.T.S. Nair, L. Guerrero and P.K. Nair, Conversion of chemically deposited CuS thin films to Cu1.8S and Cu1.96S by annealing *Semiconductor Science and Technology* **13,** 1164 (1998)

48. K. Santra, C.K. Sarkar, M.K. Mukherjee and B. Ghosh, COPPER-OXIDE THIN-FILMS GROWN BY PLASMA EVAPORATION METHOD *Thin Solid Films* **213,** 226 (1992)

49. L. Papadimitriou, N.A. Economou and D. Trivich, HETEROJUNCTION SOLAR-CELLS ON CUPROUS-OXIDE *Solar Cells* **3,** 73 (1981)

50. M.H. Habibi, B. Karimi, M. Zendehdel and M. Habibi, Fabrication, characterization of two nano-composite CuO-ZnO working electrodes for dye-sensitized solar cell

Spectrochimica Acta Part a-Molecular and Biomolecular Spectroscopy **116,** 374 (2013)

51. I.Y.Y. Bu, Novel all solution processed heterojunction using p-type cupric oxide and n-type zinc oxide nanowires for solar cell applications *Ceramics International* **39,** 8073 (2013)

52. G. Akgul, F.A. Akgul, E. Mulazimoglu, H.E. Unalan and R. Turan, Fabrication and characterization of copper oxide-silicon nanowire heterojunction photodiodes *Journal of Physics D-Applied Physics* **47,** 065106 (2014)

53. H.M. Yang, J. Ouyang, A.D. Tang, Y. Xiao, X.W. Li, X.D. Dong and Y.M. Yu, Electrochemical synthesis and photocatalytic property of cuprous oxide nanoparticles *Materials Research Bulletin* **41,** 1310 (2006)

54. Z.K. Xu, G.T. Duan, Y. Li, G.Q. Liu, H.W. Zhang, Z.F. Dai and W.P. Cai, CuO-ZnO Micro/Nanoporous Array-Film-Based Chemosensors: New Sensing Properties to H2S *Chem.-Eur. J.* **20,** 6040 (2014)

55. Q.J. Cheng, W. Yan, L. Randeniya, F.Y. Zhang and K. Ostrikov, Plasma-produced phase-pure cuprous oxide nanowires for methane gas sensing *Journal of Applied Physics* **115,** 124310 (2014)

56. L.C. Jiang and W.D. Zhang, A highly sensitive nonenzymatic glucose sensor based on CuO nanoparticles-modified carbon nanotube electrode *Biosensors & Bioelectronics* **25,** 1402 (2010)

57. H.B. Wang, Q.M. Pan, J.W. Zhao and W.T. Chen, Fabrication of CuO/C films with sisal-like hierarchical microstructures and its application in lithium ion batteries *Journal of Alloys and Compounds* **476,** 408 (2009)

58. V.D. Patake, S.S. Joshi, C.D. Lokhande and O.S. Joo, Electrodeposited porous and amorphous copper oxide film for application in supercapacitor *Materials Chemistry and Physics* **114,** 6 (2009)

59. S. Donatan, H. Yazici, H. Bermek, M. Sarikaya, C. Tamerler and M. Urgen, Physical elution in phage display selection of inorganic-binding peptides *Materials Science & Engineering C-Biomimetic and Supramolecular Systems* **29,** 14 (2009)

60. S.R. Whaley, D.S. English, E.L. Hu, P.F. Barbara and A.M. Belcher, Selection of Peptides with Semiconductor Binding Specificity for Directed Nanocrystal Assembly *Nature* **405,** 665 (2000)

61. C.E. Flynn, C. Mao, A. Hayhurst, J.L. Williams, G. Georgiou, B. Iverson and A.M. Belcher, Synthesis and Organization of Nanoscale II–VI Semiconductor Materials

Using Evolved Peptide Specificity and Viral Capsid Assembly *Journal of Materials Chemistry* **13,** 2414 (2003)

62. S.K. Lee, D.S. Yun and A.M. Belcher, Cobalt ion mediated self-assembly of genetically engineered bacteriophage for biomimetic Co-Pt hybrid material *Biomacromolecules* **7,** 14 (2006)

63. A.B. Sanghvi, K.P.H. Miller, A.M. Belcher and C.E. Schmidt, Biomaterials functionalization using a novel peptide that selectively binds to a conducting polymer *Nature Materials* **4,** 496 (2005)

64. X. Dang, H. Yi, M.-H. Ham, J. Qi, D.S. Yun, R. Ladewski, M.S. Strano, P.T. Hammond and A.M. Belcher, Virus-templated self-assembled single-walled carbon nanotubes for highly efficient electron collection in photovoltaic devices *Nature Nanotechnology* **6,** 377 (2011)

65. R.R. Naik, S.J. Stringer, G. Agarwal, S.E. Jones and M.O. Stone, Biomimetic synthesis and patterning of silver nanoparticles *Nature Materials* **1,** 169 (2002)

66. R.R. Naik, S.E. Jones, C.J. Murray, J.C. McAuliffe, R.A. Vaia and M.O. Stone, Peptide Templates for Nanoparticle Synthesis Derived from Polymerase Chain Reaction-Driven Phage Display *Advanced Functional Materials* **14,** 25 (2004)

67. K.I. Sano and K. Shiba, A Hexapeptide Motif that Electrostatically Binds to the Surface of Titanium *Journal of American Chemical Society* **125,** 14234 (2003)

68. M.B. Dickerson, R.R. Naik, M.O. Stone, Y. Cai and K.H. Sandhage, Identification of peptides that promote the rapid precipitation of germania nanoparticle networks via use of a peptide display library *Chem. Commun.* 1776 (2004)

69. M. Umetsu, M. Mizuta, K. Tsumoto, S. Ohara, S. Takami, H. Watanabe, I. Kumagai and T. Adschiri, Bioassisted Room-Temperature Immobilization and Mineralization of Zinc Oxide—The Structural Ordering of ZnO Nanoparticles into a Flower-Type Morphology *Advanced Materials* **17,** 2571 (2005)

70. I. New England Biolabs, Ph. D. Phage Display Libraries Instruction Manual (2009)

71. C. Barbas, D. Burton, J. Scott and G. Silverman, *Phage Display A Laboratory Manual* (Cold Spring Harbor Laboratory Press, Cold Spring Harbor, New York, United States of America, 2001) p.

72. Y. Huang, C.Y. Chiang, S.K. Lee, Y. Gao, E.L. Hu, J.D. Yoreo and A.M. Belcher, Programmable Assembly of Nanoarchitectures Using Genetically Engineered Viruses *Nano Letters* **5,** 1429 (2005)

73. CRC Handbook.

74. I.A. Banerjee, G. Muniz, S. Lee and H. Matsui, Mineralization of Semiconductor Nanocrystals on Peptide-Coated Bionanotubes and Their pH-Dependent Morphology Changes *Journal of Nanoscience and Nanotechnology* **7,** 2287 (2007)

75. M.T. Kumara, B.C. Tripp and S. Muralidharan, Self-assembly of metal nanoparticles and nanotubes on bioengineered flagella scaffolds *Chemistry of Materials* **19,** 2056 (2007)

76. G. Pappalardo, G. Impellizzeri, R.P. Bonomo, T. Campagna, G. Grasso and M.G. Saita, Copper(II) and nickel(II) binding modes in a histidine-containing model dodecapeptide *New Journal of Chemistry* **26,** 593 (2002)

77. S.Y. Lee, J.N. Culver and M.T. Harris, Effect of CuCl2 concentration on the aggregation and mineralization of Tobacco mosaic virus biotemplate *Journal of Colloid and Interface Science* **297,** 554 (2006)

78. A. Nedoluzhko and T. Douglas, Ordered association of tobacco mosaic virus in the presence of divalent metal ions *J. Inorg. Biochem.* **84,** 233 (2001)

79. Y.J. Lu, X. Meng, G.W. Yi and J.H. Jia, In situ growth of CuS thin films on functionalized self-assembled monolayers using chemical bath deposition *Journal of Colloid and Interface Science* **356,** 726 (2011)

80. S.M.M. Nelwamondo, M.J. Moloto, R.W.M. Krause and N. Moloto, Synthesis and characterization of alanine-capped water soluble copper sulphide quantum dots *Materials Letters* **75,** 161 (2012)

81. B.X. Li, Y. Xie and Y. Xue, Controllable synthesis of CuS nanostructures from self-assembled precursors with biomolecule assistance *Journal of Physical Chemistry C* **111,** 12181 (2007)

82. M.C. Brelle, C.L. Torres-Martinez, J.C. McNulty, R.K. Mehra and J.Z. Zhang, Synthesis and characterization of CuxS nanoparticles. Nature of the infrared band and charge-carrier dynamics *Pure and Applied Chemistry* **72,** 101 (2000)

83. K. Iwahori, R. Takagi, N. Kishimoto and I. Yamashita, A size controlled synthesis of CuS nano-particles in the protein cage, apoferritin *Materials Letters* **65,** 3245 (2011)

84. F.K. Wang, B.R. Cao and C.B. Mao, Bacteriophage Bundles with Prealigned Ca2+ Initiate the Oriented Nucleation and Growth of Hydroxylapatite *Chemistry of Materials* **22,** 3630 (2010)

85. T. He, G. Abbineni, B.R. Cao and C.B. Mao, Nanofibrous Bio-inorganic Hybrid Structures Formed Through Self-Assembly and Oriented Mineralization of Genetically Engineered Phage Nanofibers *Small* **6,** 2230 (2010)

86. K.N. Avery, J.E. Schaak and R.E. Schaak, M13 Bacteriophage as a Biological Scaffold for Magnetically-Recoverable Metal Nanowire Catalysts: Combining Specific and Nonspecific Interactions To Design Multifunctional Nanocomposites *Chemistry of Materials* **21,** 2176 (2009)

87. K.T. Nam, Y.J. Lee, E.M. Krauland, S.T. Kottmann and A.M. Belcher, Peptide-mediated reduction of silver ions on engineered biological scaffolds *Acs Nano* **2,** 1480 (2008)

88. N. Nuraje, X.N. Dang, J.F. Qi, M.A. Allen, Y. Lei and A.M. Belcher, Biotemplated Synthesis of Perovskite Nanomaterials for Solar Energy Conversion *Advanced Materials* **24,** 2885 (2012)

89. J.X. Tang, P.A. Janmey, A. Lyubartsev and L. Nordenskiold, Metal ion-induced lateral aggregation of filamentous viruses fd and M13 *Biophysical Journal* **83,** 566 (2002)

90. K. Yamamoto and S. Kashida, X-RAY STUDY OF THE AVERAGE STRUCTURES OF CU2SE AND CU1.8S IN THE ROOM-TEMPERATURE AND THE HIGH-TEMPERATURE PHASES *Journal of Solid State Chemistry* **93,** 202 (1991)

91. Y.X. Zhao, H.C. Pan, Y.B. Lou, X.F. Qiu, J.J. Zhu and C. Burda, Plasmonic Cu2-xS Nanocrystals: Optical and Structural Properties of Copper-Deficient Copper(I) Sulfides *Journal of the American Chemical Society* **131,** 4253 (2009)

92. J.M. Luther, P.K. Jain, T. Ewers and A.P. Alivisatos, Localized surface plasmon resonances arising from free carriers in doped quantum dots *Nature Materials* **10,** 361 (2011)

93. I. Grozdanov, A SIMPLE AND LOW-COST TECHNIQUE FOR ELECTROLESS DEPOSITION OF CHALCOGENIDE THIN-FILMS *Semiconductor Science and Technology* **9,** 1234 (1994)

94. I. Kriegel, C.Y. Jiang, J. Rodriguez-Fernandez, R.D. Schaller, D.V. Talapin, E. da Como and J. Feldmann, Tuning the Excitonic and Plasmonic Properties of Copper Chalcogenide Nanocrystals *Journal of the American Chemical Society* **134,** 1583 (2012)

95. S.W. Hsu, K. On and A.R. Tao, Localized Surface Plasmon Resonances of Anisotropic Semiconductor Nanocrystals *Journal of the American Chemical Society* **133,** 19072 (2011)

96. W. Zhang, A.O. Govorov and G.W. Bryant, Semiconductor-Metal Nanoparticle Molecules: Hybrid Excitons and the Nonlinear Fano Effect *Physical Review Letters* **97,** 146804 (2006)

97. A.O. Govorov, G.W. Bryant, W. Zhang, T. Skeini, J. Lee, N.A. Kotov, J.M. Slocik and R.R. Naik, Exciton−Plasmon Interaction and Hybrid Excitons in Semiconductor−Metal Nanoparticle Assemblies *Nano Letters* **6,** 984 (2006)

98. G. Ku, M. Zhou, S. Song, Q. Huang, J. Hazle and C. Li, Copper Sulfide Nanoparticles As a New Class of Photoacoustic Contrast Agent for Deep Tissue Imaging at 1064 nm *ACS Nano* **6,** 7489 (2012)

99. M. Zhou, R. Zhang, M. Huang, W. Lu, S. Song, M.P. Melancon, M. Tian, D. Liang and C. Li, A Chelator-Free Multifunctional [64Cu]CuS Nanoparticle Platform for Simultaneous Micro-PET/CT Imaging and Photothermal Ablation Therapy *Journal of the American Chemical Society* **132,** 15351 (2010)

100. Y.B. Li, W. Lu, Q.A. Huang, M.A. Huang, C. Li and W. Chen, Copper sulfide nanoparticles for photothermal ablation of tumor cells *Nanomedicine* **5,** 1161 (2010)

101. C.M. Hessel, V.P. Pattani, M. Rasch, M.G. Panthani, B. Koo, J.W. Tunnell and B.A. Korgel, Copper Selenide Nanocrystals for Photothermal Therapy *Nano Letters* **11,** 2560 (2011)

102. H. Lee, S.W. Yoon, E.J. Kim and J. Park, In-situ growth of copper sulfide nanocrystals on multiwalled carbon nanotubes and their application as novel solar cell and amperometric glucose sensor materials *Nano Letters* **7,** 778 (2007)

103. A.A. Sagade and R. Sharma, Copper sulphide (CuxS) as an ammonia gas sensor working at room temperature *Sensors and Actuators B-Chemical* **133,** 135 (2008)

104. Z. Li, L. Mi, W. Chen, H. Hou, C. Liu, H. Wang, Z. Zheng and C. Shen, Three-dimensional CuS hierarchical architectures as recyclable catalysts for dye decolorization *CrystEngComm* **14,** 3965 (2012)

105. Y. Liu, Y. Deng, Z. Sun, J. Wei, G. Zheng, A.M. Asiri, S.B. Khan, M.M. Rahman and D. Zhao, Hierarchical Cu2S Microsponges Constructed from Nanosheets for Efficient Photocatalysis *Small* **9,** 2702 (2013)

106. D. Dorfs, T. Hartling, K. Miszta, N.C. Bigall, M.R. Kim, A. Genovese, A. Falqui, M. Povia and L. Manna, Reversible Tunability of the Near-Infrared Valence Band Plasmon Resonance in Cu2-xSe Nanocrystals *Journal of the American Chemical Society* **133,** 11175 (2011)

107. A.B.F. Martinson, S.C. Riha, E. Thimsen, J.W. Elam and M.J. Pellin, Structural, optical, and electronic stability of copper sulfide thin films grown by atomic layer deposition *Energy & Environmental Science* **6,** 1868 (2013)

108. M. Lotfipour, T. Machani, D.P. Rossi and K.E. Plass, alpha-Chalcocite Nanoparticle Synthesis and Stability *Chemistry of Materials* **23,** 3032 (2011)

109. X. Liu, X. Wang, B. Zhou, W.-C. Law, A.N. Cartwright and M.T. Swihart, Size-Controlled Synthesis of Cu2-xE (E = S, Se) Nanocrystals with Strong Tunable Near-Infrared Localized Surface Plasmon Resonance and High Conductivity in Thin Films *Advanced Functional Materials* **23,** 1256 (2013)

110. S.C. Riha, S. Jin, S.V. Baryshev, E. Thimsen, G.P. Wiederrecht and A.B.F. Martinson, Stabilizing Cu2S for Photovoltaics One Atomic Layer at a Time *ACS Applied Materials & Interfaces* **5,** 10302 (2013)

111. M.S. Zaman, C.H. Moon, K.N. Bozhilov and E.D. Haberer, Phage-directed synthesis of copper sulfide: structural and optical characterization *Nanotechnology* **24,** 325602 (2013)

112. G. Mie, Beiträge zur Optik trüber Medien, speziell kolloidaler Metallösungen *Annalen der Physik* **330,** 377 (1908)

113. G.C. Papavassiliou, Optical properties of small inorganic and organic metal particles *Progress in Solid State Chemistry* **12,** 185 (1979)

114. U. Kreibig and M. Vollmer, *Optical Properties of Metal Clusters* (Springer, Berlin, 1995) p.

115. C. Wagner, The theory of the warm-up process *Zeitschrift Fur Physikalische Chemie-Abteilung B-Chemie Der Elementarprozesse Aufbau Der Materie* **21,** 25 (1933)

116. S.C. Riha, D.C. Johnson and A.L. Prieto, Cu2Se Nanoparticles with Tunable Electronic Properties Due to a Controlled Solid-State Phase Transition Driven by Copper Oxidation and Cationic Conduction *Journal of the American Chemical Society* **133,** 1383 (2011)

117. J. Leloup, A. Ruaudelteixier, A. Barraud, H. Roulet and G. Dufour, XPS STUDY OF COPPER SULFIDES INSERTED INTO A LANGMUIR-BLODGETT MATRIX *Applied Surface Science* **68,** 231 (1993)

118. A. Rossi, D. Atzei, S. Da Pelo, F. Frau, P. Lattanzi, K.E.R. England and D.J. Vaughan, Quantitative X-ray photoelectron spectroscopy study of enargite (Cu3AsS4) surface *Surface and Interface Analysis* **31,** 465 (2001)

119. M. Kundu, T. Hasegawa, K. Terabe, K. Yamamoto and M. Aono, Structural studies of copper sulfide films: effect of ambient atmosphere *Science and Technology of Advanced Materials* **9,** 035011 (2008)

120. G. Deroubaix and P. Marcus, X-RAY PHOTOELECTRON-SPECTROSCOPY ANALYSIS OF COPPER AND ZINC-OXIDES AND SULFIDES *Surface and Interface Analysis* **18,** 39 (1992)

121. K. Laajalehto, I. Kartio and P. Nowak, XPS STUDY OF CLEAN METAL SULFIDE SURFACES *Applied Surface Science* **81,** 11 (1994)

122. A. Ghahremaninezhad, E. Asselin and D.G. Dixon, Electrodeposition and Growth Mechanism of Copper Sulfide Nanowires *Journal of Physical Chemistry C* **115,** 9320 (2011)

123. M.C. Biesinger, L.W.M. Lau, A.R. Gerson and R.S.C. Smart, Resolving surface chemical states in XPS analysis of first row transition metals, oxides and hydroxides: Sc, Ti, V, Cu and Zn *Applied Surface Science* **257,** 887 (2010)

124. G. Lefevre, J. Bessiere, J.J. Ehrhardt and A. Walcarius, Immobilization of iodide on copper(I) sulfide minerals *Journal of Environmental Radioactivity* **70,** 73 (2003)

125. E.C. Todd and D.M. Sherman, Surface oxidation of chalcocite (Cu2S) under aqueous (pH=2-11) and ambient atmospheric conditions: Mineralogy from Cu L- and OK-edge X-ray absorption spectroscopy *American Mineralogist* **88,** 1652 (2003)

126. J.F. Moulder, C. Jill and R.C. King, *Handbook of X-ray Photoelectron Spectroscopy: a reference book of standard spectra for identification and interpretation of XPS data* (Physical Electronics, Eden Prairie, Minn., 1995) p.

127. Toxicological Profile for Ammonia. US Department of Health and Human Services Public Health Service (Agency for Toxic Substances and Disease Registry (ATSDR) http://www.atsdr.cdc.gov/toxprofiles/tp.asp?id=11&tid=2)

128. (https://www.osha.gov/dts/chemicalsampling/data/CH_218300.html

129. S.G. Wang, Q. Zhang, D.J. Yang, P.J. Sellin and G.F. Zhong, Multi-walled carbon nanotube-based gas sensors for NH3 detection *Diamond and Related Materials* **13,** 1327 (2004)

130. G.S.T. Rao and D.T. Rao, Gas sensitivity of ZnO based thick film sensor to NH3 at room temperature *Sensors and Actuators B-Chemical* **55,** 166 (1999)

131. J. Zhang, S.R. Wang, M.J. Xu, Y. Wang, H.J. Xia, S.M. Zhang, X.Z. Guo and S.H. Wu, Polypyrrole-Coated SnO2 Hollow Spheres and Their Application for Ammonia Sensor *Journal of Physical Chemistry C* **113,** 1662 (2009)

132. A. Galdikas, A. Mironas, V. Strazdiene, A. Setkus, I. Ancutiene and V. Janickis, Room-temperature-functioning ammonia sensor based on solid-state CuxS films *Sensors and Actuators B-Chemical* **67,** 76 (2000)

133. A. Setkus, A. Galdikas, A. Mironas, I. Simkiene, I. Ancutiene, V. Janickis, S. Kaciulis, G. Mattogno and G.M. Ingo, Properties of CuxS thin film based structures: influence on the sensitivity to ammonia at room temperatures *Thin Solid Films* **391,** 275 (2001)

134. X.L. Yu, Y. Wang, H.L.W. Chan and C.B. Cao, Novel gas sensoring materials based on CuS hollow spheres *Microporous and Mesoporous Materials* **118,** 423 (2009)

135. W. Zhang, Z. Chen and Z. Yang, An inward replacement/etching route to synthesize double-walled Cu7S4 nanoboxes and their enhanced performances in ammonia gas sensing *Physical Chemistry Chemical Physics* **11,** 6263 (2009)

136. T. Fu, CuS-doped CuO nanoparticles sensor for detection of H2S and NH3 at room temperature *Electrochimica Acta* **112,** 230 (2013)

137. A.A. Sagade, R. Sharma and I. Sulaniya, Enhancement in sensitivity of copper sulfide thin film ammonia gas sensor: Effect of swift heavy ion irradiation *Journal of Applied Physics* **105,** (2009)

138. A. Setkus, A. Galdikas, A. Mironas, V. Strazdiene, I. Simkiene, L. Ancutiene, V. Janickis, S. Kaciulis, G. Mattogno and G.M. Ingo, The room temperature ammonia sensor based on improved CuxS-micro-porous-Si structure *Sensors and Actuators B-Chemical* **78,** 208 (2001)

139. M.S. Zaman, G.B. Grajeda and E.D. Haberer, Optical and electrical stability of viral-templated copper sulfide (Cu1.8S) films *Journal of Applied Physics* **115,** (2014)

140. M.C. McAlpine, H.D. Agnew, R.D. Rohde, M. Blanco, H. Ahmad, A.D. Stuparu, W.A. Goddard, III and J.R. Heath, Peptide-nanowire hybrid materials for

selective sensing of small molecules *Journal of the American Chemical Society* **130,** 9583 (2008)

141. J. Hlavay and G.G. Guilbault, DETECTION OF AMMONIA IN AMBIENT AIR WITH COATED PIEZOELECTRIC CRYSTAL DETECTOR *Analytical Chemistry* **50,** 1044 (1978)

142. C.Y. Shen, C.P. Huang and H.C. Chuo, The improved ammonia gas sensors constructed by L-glutamic acid hydrochloride on surface acoustic wave devices *Sensors and Actuators B-Chemical* **84,** 231 (2002)

143. S. Padalkar, J.R. Capadona, S.J. Rowan, C. Weder, Y.H. Won, L.A. Stanciu and R.J. Moon, Natural Biopolymers: Novel Templates for the Synthesis of Nanostructures *Langmuir* **26,** 8497 (2010)

144. V.K. Patel and S. Bhattacharya, High-Performance Nanothermite Composites Based on Aloe-Vera-Directed CuO Nanorods *Acs Applied Materials & Interfaces* **5,** 13364 (2013)

145. R. Hassanien, A.F.A.-S. Said, L. Siller, R. Little, N.G. Wright, A. Houlton and B.R. Horrocks, Smooth and conductive DNA-templated Cu 2 O nanowires: growth morphology, spectroscopic and electrical characterization *Nanotechnology* **23,** 075601 (2012)

146. S.M.D. Watson, N.G. Wright, B.R. Horrocks and A. Houlton, Preparation, Characterization and Scanned Conductance Microscopy Studies of DNA-Templated One-Dimensional Copper Nanostructures *Langmuir* **26,** 2068 (2010)

147. J.C. Zhou, C.M. Soto, M.-S. Chen, M.A. Bruckman, M.H. Moore, E. Barry, B.R. Ratna, P.E. Pehrsson, B.R. Spies and T.S. Confer, Biotemplating rod-like viruses for the synthesis of copper nanorods and nanowires *Journal of Nanobiotechnology* **10,** 18 (2012)

148. C.K. Jeong, I. Kim, K.-I. Park, M.H. Oh, H. Paik, G.-T. Hwang, K. No, Y.S. Nam and K.J. Lee, Virus-Directed Design of a Flexible BaTiO3 Nanogenerator *Acs Nano* **7,** 11016 (2013)

149. W.F. Wolkers, P.I. Haris, A.M.A. Pistorius, D. Chapman and M.A. Hemminga, FT-IR SPECTROSCOPY OF THE MAJOR COAT PROTEIN OF M13 AND PF1 IN THE PHAGE AND RECONSTITUTED INTO PHOSPHOLIPID SYSTEMS *Biochemistry* **34,** 7825 (1995)

150. A. Barth and C. Zscherp, What vibrations tell us about proteins *Quarterly Reviews of Biophysics* **35,** 369 (2002)

151. Z. Movasaghi, S. Rehman and I.U. Rehman, Fourier transform infrared (FTIR) spectroscopy of biological tissues *Applied Spectroscopy Reviews* **43,** 134 (2008)

152. D.X. Dong, Y.G. Zhang, S. Sutaria, A. Konarov and P. Chen, Binding Mechanism and Electrochemical Properties of M13 Phage-Sulfur Composite *Plos One* **8,** 82332 (2013)

153. S. Barua, G. Das, L. Aidew, A.K. Buragohain and N. Karak, Copper-copper oxide coated nanofibrillar cellulose: a promising biomaterial *Rsc Advances* **3,** 14997 (2013)

154. A. Kirfel and K. Eichhorn, Accurate structure analysis with synchrotron radiation. The electron density in Al2O3 and Cu2O *Acta Crystallographica Section A* **46,** 271 (1990)

155. S. Asbrink and L.-J. Norrby, A refinement of the crystal structure of copper(II) oxide with a discussion of some exceptional e.s.d.'s *Acta Crystallographica Section B* **26,** 8 (1970)

156. M. Ceolin, N. Galvez, P. Sanchez, B. Fernandez and J.M. Dominguez-Vera, Structural aspects of the growth mechanism of copper nanoparticles inside apoferritin *European Journal of Inorganic Chemistry* 795 (2008)

157. R. Prucek, L. Kvitek, A. Panacek, L. Vancurova, J. Soukupova, D. Jancik and R. Zboril, Polyacrylate-assisted synthesis of stable copper nanoparticles and copper(I) oxide nanocubes with high catalytic efficiency *Journal of Materials Chemistry* **19,** 8463 (2009)

158. A. Kumar, A. Saxena, A. De, R. Shankar and S. Mozumdar, Facile synthesis of size-tunable copper and copper oxide nanoparticles using reverse microemulsions *Rsc Advances* **3,** 5015 (2013)

159. J. Tauc, Grigorov.R and A. Vancu, OPTICAL PROPERTIES AND ELECTRONIC STRUCTURE OF AMORPHOUS GERMANIUM *Physica Status Solidi* **15,** 627 (1966)

160. K. Borgohain, N. Murase and S. Mahamuni, Synthesis and properties of Cu2O quantum particles *Journal of Applied Physics* **92,** 1292 (2002)

161. B. Balamurugan, I. Aruna, B.R. Mehta and S.M. Shivaprasad, Size-dependent conductivity-type inversion in Cu2O nanoparticles *Physical Review B* **69,** 165419 (2004)

162. H. Wang, J.Z. Xu, J.J. Zhu and H.Y. Chen, Preparation of CuO nanoparticles by microwave irradiation *J. Cryst. Growth* **244,** 88 (2002)

163. D.I. Son, C.H. You and T.W. Kim, Structural, optical, and electronic properties of colloidal CuO nanoparticles formed by using a colloid-thermal synthesis process *Applied Surface Science* **255,** 8794 (2009)

164. G. Celep, E. Cottancin, J. Lerme, M. Pellarin, L. Arnaud, J.R. Huntzinger, J.L. Vialle, M. Broyer, B. Palpant, O. Boisron and P. Melinon, Optical properties of copper clusters embedded in alumina: An experimental and theoretical study of size dependence *Physical Review B* **70,** 165409 (2004)

165. C. Salzemann, I. Lisiecki, A. Brioude, J. Urban and M.P. Pileni, Collections of copper nanocrystals characterized by different sizes and shapes: Optical response of these nanoobjects *Journal of Physical Chemistry B* **108,** 13242 (2004)

166. T. Ghodselahi, M.A. Vesaghi and A. Shafiekhani, Study of surface plasmon resonance of Cu@Cu2O core-shell nanoparticles by Mie theory *Journal of Physics D-Applied Physics* **42,** 015308 (2009)

167. G.M. Liu, T. Schulmeyer, J. Brotz, A. Klein and W. Jaegermann, Interface properties and band alignment of Cu2S/CdS thin film solar cells *Thin Solid Films* **431,** 477 (2003)

168. B.R. Mehta, S. Gupta, V.N. Singh, P. Tripathi and D. Varandani, Photovoltaic response of a topotaxially formed CdS-CuxS single nanorod heterojunction *Nanotechnology* **22,** (2011)

169. A. Goldenblum, G. Popovici, E. Elena, A. Oprea and C. Nae, ALL-EVAPORATION-PROCESSED CU2S CDS SOLAR-CELLS WITH IMPROVED CHARACTERISTICS *Thin Solid Films* **141,** 215 (1986)

170. D. Wu, X. Fan, J. Dai, H. Liu, H. Liu and F. Zhang, Preparation and Photocatalytic Properties of Cu2S/Tetrapod-Like ZnO Whisker Nanocomposites *Chinese Journal of Catalysis* **33,** 802 (2012)